



U.S. Department  
of Transportation  
**Federal Highway  
Administration**

PB97135818



Publication No. FHWA-RD-96-059  
February 1997


---

# Preliminary Vehicle Impact Simulation Technology Advancement (Pre-VISTA)

---

Research and Development  
Turner-Fairbank Highway Research Center  
6300 Georgetown Pike  
McLean, Virginia 22101-2296



1. Report No. FHWA-RD-96-059		PB97-135818 		3. Recipient's Catalog No.	
4. Title and Subtitle PRELIMINARY VEHICLE IMPACT SIMULATION TECHNOLOGY ADVANCEMENT (Pre-VISTA)		5. Report Date February 1997		6. Performing Organization Code	
		8. Performing Organization Report No.		10. Work Unit No. (TRAVIS) 3A5A	
7. Author(s) Dale Schauer, F. Tokarz, G. Kay, A. Lee, R. Logan, E. Coffie, M. Ray		9. Performing Organization Name and Address Lawrence Livermore National Laboratory 7000 East Avenue Livermore, California 94550		11. Contract or Grant No. DTFH61-90-C-00000	
12. Sponsoring Agency Name and Address Office of Safety & Traffic Operations R&D Federal Highway Administration 6300 Georgetown Pike McLean, Virginia 22101-2296		13. Type of Report and Period Covered Final Report March 1993 - March 1995		14. Sponsoring Agency Code	
		15. Supplementary Notes Contracting Officer's Technical Representative (COTR): Martin Hargrave, HSR-20			
16. Abstract The Lawrence Livermore National Laboratory (LLNL) has completed a preliminary evaluation of current finite element technology capability applied to roadside hardware design and vehicle crashworthiness research using the non-linear structural code, DYNA3D. Independently developed vehicle models were evaluated, modified, and then used in several vehicle crash simulations. Criteria were specified for improving the development of vehicle models. Simulation capabilities were increased, and future direction identified for the roadside safety community.					
<div style="border: 1px solid black; padding: 5px; width: fit-content; margin: 0 auto;"> <p>PROTECTED UNDER INTERNATIONAL COPYRIGHT ALL RIGHTS RESERVED. NATIONAL TECHNICAL INFORMATION SERVICE U.S. DEPARTMENT OF COMMERCE</p> </div>					
17. Key Words Finite Element Modeling, DYNA3D, Vehicle Crash Simulation, Vehicle Models, Barrier Models, Vehicle and Occupant Modeling, Material Models			18. Distribution Statement No restrictions. This document is available to the public through the National Technical Information Service, Springfield, Virginia 22161.		
19. Security Classif. (of this report) Unclassified	20. Security Classif. (of this page) Unclassified	21. No. of Pages 144	22. Price		

# SI\* (MODERN METRIC) CONVERSION FACTORS

## APPROXIMATE CONVERSIONS TO SI UNITS

## APPROXIMATE CONVERSIONS FROM SI UNITS

Symbol	When You Know	Multiply By	To Find	Symbol	Symbol	When You Know	Multiply By	To Find	Symbol
<b>LENGTH</b>					<b>LENGTH</b>				
in	inches	25.4	millimeters	mm	mm	millimeters	0.039	inches	in
ft	feet	0.305	meters	m	m	meters	3.28	feet	ft
yd	yards	0.914	meters	m	m	meters	1.09	yards	yd
mi	miles	1.61	kilometers	km	km	kilometers	0.621	miles	mi
<b>AREA</b>					<b>AREA</b>				
in <sup>2</sup>	square inches	645.2	square millimeters	mm <sup>2</sup>	mm <sup>2</sup>	square millimeters	0.0016	square inches	in <sup>2</sup>
ft <sup>2</sup>	square feet	0.093	square meters	m <sup>2</sup>	m <sup>2</sup>	square meters	10.764	square feet	ft <sup>2</sup>
yd <sup>2</sup>	square yards	0.836	square meters	m <sup>2</sup>	m <sup>2</sup>	square meters	1.195	square yards	yd <sup>2</sup>
ac	acres	0.405	hectares	ha	ha	hectares	2.47	acres	ac
mi <sup>2</sup>	square miles	2.59	square kilometers	km <sup>2</sup>	km <sup>2</sup>	square kilometers	0.386	square miles	mi <sup>2</sup>
<b>VOLUME</b>					<b>VOLUME</b>				
fl oz	fluid ounces	29.57	milliliters	mL	mL	milliliters	0.034	fluid ounces	fl oz
gal	gallons	3.785	liters	L	L	liters	0.264	gallons	gal
ft <sup>3</sup>	cubic feet	0.028	cubic meters	m <sup>3</sup>	m <sup>3</sup>	cubic meters	35.71	cubic feet	ft <sup>3</sup>
yd <sup>3</sup>	cubic yards	0.765	cubic meters	m <sup>3</sup>	m <sup>3</sup>	cubic meters	1.307	cubic yards	yd <sup>3</sup>
NOTE: Volumes greater than 1000 l shall be shown in m <sup>3</sup> .									
<b>MASS</b>					<b>MASS</b>				
oz	ounces	28.35	grams	g	g	grams	0.035	ounces	oz
lb	pounds	0.454	kilograms	kg	kg	kilograms	2.202	pounds	lb
T	short tons (2000 lb)	0.907	megagrams (or "metric ton")	Mg (or "t")	Mg (or "t")	megagrams (or "metric ton")	1.103	short tons (2000 lb)	T
<b>TEMPERATURE (exact)</b>					<b>TEMPERATURE (exact)</b>				
°F	Fahrenheit temperature	5(F-32)/9 or (F-32)/1.8	Celcius temperature	°C	°C	Celcius temperature	1.8C + 32	Fahrenheit temperature	°F
<b>ILLUMINATION</b>					<b>ILLUMINATION</b>				
fc	foot-candles	10.76	lux	lx	lx	lux	0.0929	foot-candles	fc
fl	foot-Lamberts	3.426	candela/m <sup>2</sup>	cd/m <sup>2</sup>	cd/m <sup>2</sup>	candela/m <sup>2</sup>	0.2919	foot-Lamberts	fl
<b>FORCE and PRESSURE or STRESS</b>					<b>FORCE and PRESSURE or STRESS</b>				
lbf	poundforce	4.45	newtons	N	N	newtons	0.225	poundforce	lbf
lbf/in <sup>2</sup>	poundforce per square inch	6.89	kilopascals	kPa	kPa	kilopascals	0.145	poundforce per square inch	lbf/in <sup>2</sup>

\* SI is the symbol for the International System of Units. Appropriate rounding should be made to comply with Section 4 of ASTM E380.

## TABLE OF CONTENTS

	<u>Page</u>
CHAPTER 1: INTRODUCTION .....	1
CHAPTER 2: SOFTWARE DEVELOPMENT .....	5
Section 1. DYNA3D & MADYMO link .....	5
Section 2. NIKE3D to DYNA3D link and assessment of DYNA3D as a vehicle handling code .....	18
Section 3. RTH and DYNA link .....	21
Section 4. Tire model in DYNA consistent with NIKE and RTH .....	23
Section 5. Summary of material constitutive models used for vehicle/occupant interaction .....	25
Section 6. Evaluate IGES Implementation into INGRID .....	29
Section 7. DYNA3D Airbag Capability .....	30
CHAPTER 3: DYNA-MADYMO VEHICLE CRASH SIMULATIONS .....	35
Section 1. Frontal Taurus model .....	35
Section 2. Debug frontal impact Taurus model .....	35
Section 3. Frontal impact crash simulation .....	36
Section 4. Side impact Taurus model from NHTSA .....	41
Section 5. Debug side impact Taurus model received from NHTSA .....	41
Section 6. MDB model for side impact .....	41
Section 7. MDB side impact simulation .....	42
CHAPTER 4: PASSENGER COMPARTMENT MATERIAL MODELS .....	45
Section 1. Crushable foam .....	45
Section 2. Safety glass .....	49
CHAPTER 5: VEHICLE AND BARRIER CRASH SIMULATIONS .....	55
Section 1. Frontal Honda model impact with rigid poles .....	56
Section 2. Frontal Honda model impact with u-sign post .....	68
Section 3. Vehicle model refinement .....	79
Section 4. Ford Festiva FE model impacting a rigid pole .....	90
Section 5. Breakaway cable terminal model .....	103
CHAPTER 6: DISCUSSION .....	119
CHAPTER 7: CONCLUSIONS AND RECOMMENDATIONS .....	125
REFERENCES .....	129

## LIST OF FIGURES

<u>Figure</u>		<u>Page</u>
Figure 1.	One-way DYNA3D to MADYMO linkage results for the impact of a 1991 domestic sedan into a rigid wall at 48 km/h.....	7
Figure 2.	Correlation with accelerometer crash data for the impact of a 1991 domestic sedan into a rigid wall at 48 km/h.....	8
Figure 3.	Calculated engine block acceleration for the impact of a 1991 domestic sedan into a rigid wall.....	8
Figure 4.	Flow chart of DYNA3D/MADYMO coupling algorithm.....	10
Figure 5.	MADYMO/INGRID Hybrid III representations.....	12
Figure 6.	MADYMO/INGRID Eurosid representations.....	13
Figure 7.	Two-way linkage example of spherical shell impacting a wall.....	14
Figure 8.	Belted Hybrid III dummy under simple deceleration.....	15
Figure 9.	Coupled DYNA3D/MADYMO only results from a Hybrid III dummy impacting a short wall.....	16
Figure 10.	Further coupled DYNA3D/MADYMO only results from a Hybrid III dummy impacting a short wall.....	17
Figure 11.	Frontal impact of a sedan into a rigid wall with a Hybrid III occupant....	19
Figure 12.	Implementation of steering algorithm and lateral tire force in NIKE3D...	24
Figure 13.	Lateral acceleration for the prototype electric vehicle scenarios.....	24
Figure 14.	Initial airbag configuration.....	33
Figure 15.	Internal airbag pressure during representative inflation cycles.....	33
Figure 16.	Partially inflated airbag during contact with a rigid sphere.....	33
Figure 17.	Results of Taurus full frontal impact at 56 km/h.....	37
Figure 18.	Comparison of engine acceleration test data with DYNA3D results for a Taurus full frontal impact at 56 km/h.....	38
Figure 19.	Taurus mesh with a Hybrid III occupant.....	40
Figure 20.	Full frontal 59 km/h MDB impact results.....	43
Figure 21.	60 degree 59 km/h MDB impact results.....	44
Figure 22.	Three regions of stress seen in experimental data from a uniaxial compression test along with DYNA3D simulation.....	47
Figure 23.	Experimental data for compressive radial stress at failure in triaxial tests, along with the envelope of failure surfaces f1, f2, f3.....	47
Figure 24.	Experimental data and DYNA3D simulation of uniaxial compression tests done at four different strain rates.....	48
Figure 25.	Experimental data and DYNA3D simulation of uniaxial compression tests done on two orientations of the same orthotropic foam.....	48
Figure 26.	Experimental results and DYNA3D simulation of a drop test in which a 18.2 kg aluminum block traveling at 32.5 km/h impacts a 0.06-m thick section of foam.....	48
Figure 27.	Plan view of the underside of the quarter pane, showing the mesh and the cracked zones.....	52
Figure 28.	Velocity vs. time of the steel ball for three problems.....	53
Figure 29.	Velocity vs. time of the steel portion of the ball for two problems.....	53
Figure 30.	Original Honda Civic model.....	57
Figure 31.	Modified center bumper rigid pole impact model.....	60
Figure 32.	Center bumper impact model deformed shape at 0.1 s.....	60
Figure 33.	Center bumper impact model deformed shapes.....	61
Figure 34.	Comparison of test and DYNA3D results for center bumper impact.....	62
Figure 35.	457 mm left-of-center bumper impact model.....	64

**LIST OF FIGURES**  
(continued)

<u>Figure</u>		<u>Page</u>
Figure 36.	Deformed bumper support model at 0.08 s.....	64
Figure 37.	Comparison of test and DYNA3D results for bumper support impact. ...	65
Figure 38.	254-mm right-of-center bumper impact. ....	66
Figure 39.	Deformed 254-mm right-of-center impact model at 0.1 s.....	66
Figure 40.	Comparison of test and DYNA3D results for 254-mm right-of-center bumper impact. ....	67
Figure 41.	Modified u-channel sign post impact model. ....	67
Figure 42.	Deformed u-channel sign post impact model at 0.1 s.....	72
Figure 43.	Comparison of test and DYNA3D results for u-channel sign post impact model. ....	72
Figure 44.	Exploded view of soil/u-channel sign post showing slideline surfaces. ...	74
Figure 45.	Acceleration history of the original type 3 soil model. ....	74
Figure 46.	Acceleration histories of type 5 soil models based on Antelope Lake and Sandia desert soil. ....	75
Figure 47.	Acceleration histories of type 3 soil models based on Antelope Lake and Sandia desert soil. ....	75
Figure 48.	Acceleration histories of type 3 and type 5 soil models based on Antelope Lake soil. ....	76
Figure 49.	Acceleration histories of type 3 and type 5 soil models based on Sandia desert soil. ....	76
Figure 50.	Acceleration histories of type 3 soil models based on Antelope Lake soil with different friction coefficients.....	77
Figure 51.	Acceleration histories of type 3 soil models based on Sandia desert soil with different friction coefficients.....	77
Figure 52.	Deformed shape with friction coefficient = 0.0. ....	78
Figure 53.	Deformed shape with friction coefficient = 0.15.....	78
Figure 54.	Rigid pole impact model. ....	81
Figure 55.	Model modification flow chart. ....	81
Figure 56.	FE mesh of the original cradle with rigid beam engine mounts. ....	82
Figure 57.	FE mesh of the modified cradle with forward shell and aft rigid beam engine. ....	82
Figure 58.	Buckled cradle in the rigid pole center bumper impact simulation. ....	84
Figure 59.	Correlations between rigid beam/rigid beam and beam/beam engine mounts from the center impact simulation. ....	85
Figure 60.	Correlations between shell/rigid beam and spring/spring engine mounts from the center bumper impact simulation. ....	85
Figure 61.	Location of c.g. in the vehicle model.....	86
Figure 62.	Correlations between shell/rigid beam model and rear seat deceleration data from the center bumper crash test. ....	86
Figure 63.	Festiva FE model. ....	91
Figure 64.	Festiva deformation from center pole impact, 0-120 ms. ....	93
Figure 65.	Accelerations at c.g. of vehicle.....	96
Figure 66.	Rigid pole force. ....	98
Figure 67.	Acceleration at c.g. for all three simulations.....	99
Figure 68.	Rigid pole forces for all three simulations. ....	100
Figure 69.	View of the BCT FE model.....	105

**LIST OF FIGURES**  
(continued)

<u>Figure</u>		<u>Page</u>
Figure 70.	View of the end of the BCT model.....	105
Figure 71.	Buffered end section.....	106
Figure 72.	Terminal end connector.....	106
Figure 73.	W-beam guardrail.....	107
Figure 74.	Simulation of a BCT impact.....	109
Figure 75.	Simulation of the collapse of the BCT nose.....	110
Figure 76.	Fracture of the breakaway timber post.....	111
Figure 77.	Acceleration of the c.g. - test and simulation.....	113

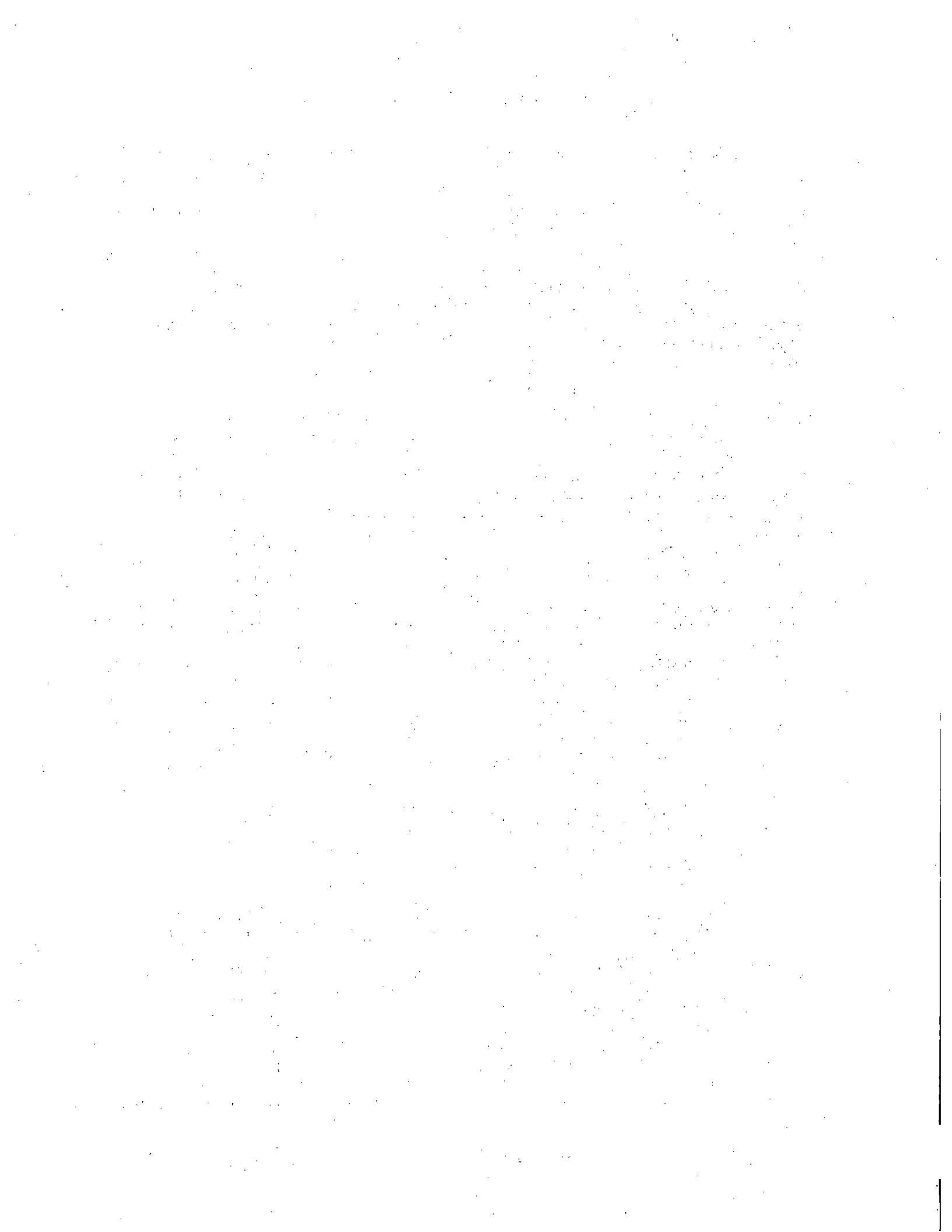
**LIST OF TABLES**

<u>Table</u>		<u>Page</u>
Table 1.	Test matrix.....	58
Table 2.	Material type 3: elastic-plastic.....	69
Table 3.	Material type 5 model for Antelope Lake soil.....	70
Table 4.	Pressure-volumetric strain curve for Antelope Lake soil.....	70
Table 5.	Material type 5 model for Sandia desert soil.....	71
Table 6.	Pressure-volumetric strain curve for Sandia desert soil.....	71
Table 7.	Soil models parametric analysis matrix.....	89
Table 8.	Friction coefficient parametric analysis matrix.....	89
Table 9.	Engine cradle parametric analysis matrix.....	89
Table 10.	Summary of centerline impact results.....	101
Table 11.	Summary of results.....	102
Table 12.	Simulation performance.....	102
Table 13.	Buffer section and terminal connector material properties.....	115
Table 14.	Cross-section properties of W-beam guardrail.....	116
Table 15.	Guardrail material properties.....	116
Table 16.	Timber material properties.....	117
Table 17.	Ultimate failure stress of timber in pendulum tests.....	117
Table 18.	Simulation characteristics.....	118
Table 19.	Roadside hardware models being developed by universities.....	126



## LIST OF ABBREVIATIONS AND SYMBOLS

BCT	Breakaway cable terminal
CAD	Computer aided drafting
c.g.	Center-of-gravity
CPU	Central processor unit
CVS	Crash victim simulation
DOF	Degrees of freedom
ELT	Eccentric loader BCT
Eurosid	Standard validated dummies used in impact studies in Europe.
FE	Finite element
FEA	Finite element analysis
FHWA	Federal Highway Administration
FOIL	Federal Outdoor Impact Laboratory
HIC	Head Injury Criterion
Hybrid III	Standard validated dummies used in impact studies in the United States
HVOSM	Highway Vehicle Object Simulation Model
IGES	International graphics engineering standard
IWRC	Internal-wire-rope-core cable
LLNL	Lawrence Livermore National Laboratory
MDB	Moving deformable barrier
MELT	Modified eccentric loader BCT
NCHRP	National Cooperative Highway Research Program
NHTSA	National Highway Traffic Safety Administration
NURBS	Nonuniform rational B-spline, a type of surface definition
PATRAN	Commercial three-dimensional mesh generator
Pre-VISTA	Preliminary Vehicle Impact Simulation Technology Advancement
PVM	Parallel virtual machine
RTH	Real Time Handling code
TAHRS	Tire, Accident, Handling, and Roadway Safety Program at LLNL



## CHAPTER 1: INTRODUCTION

The Lawrence Livermore National Laboratory (LLNL), Federal Highway Administration (FHWA) and National Highway Traffic Safety Administration (NHTSA) established a cooperative agreement in 1992 to evaluate current finite element (FE) technology capability for roadside hardware design and vehicle crashworthiness research. The purpose was to demonstrate that the FE method could be used to model common vehicle barrier crash scenarios. After several discussions, a list of agreed upon topics were identified for further investigation. The results of these discussions are represented by the document title, "Preliminary Vehicle Impact Simulation Technology Advancement" or Pre-VISTA. This report documents these efforts and comments on the results. The previous safety community modeling history combined with LLNL's code development capability and large base of experienced code users played a role in the initiation of this cooperative agreement.

To set the stage for this report, it is appropriate to present a brief history of roadside safety research. In the early 1960's, roadway safety was recognized as a problem that could be addressed and improved by proper use of engineering design. Initially, safety improvements could be made through the use of common sense to keep the vehicle on the road, the occupant in the vehicle, and the vehicle from turning over or being penetrated by the guardrail components. Later, in the 1970's and 1980's, crash testing developed as the major tool to evaluate the collision performance of barriers. This intuitive approach produced many designs that are still quite serviceable.

A combination of events has left the roadside safety community with problems that are very complex and, as a result, are very difficult to solve using only intuition. Today, there are more different types and sizes of vehicles than ever before. There is also more public awareness about safety than in previous years. This combined with the variety of accident scenarios, such as side impacts, non-tracking impacts, and vehicle-barrier interaction, as well as variations in guardrail terminal design and installation, have overwhelmed the roadside hardware designer. The designer needs updated tools to help address these difficult problems and to improve roadside safety. This report discusses the results of using a non-linear dynamic FE analytical method to simulate roadway-vehicle problems.

The first use of analytical methods applied to roadside safety was conducted by researchers at Cornell Aeronautical Laboratory.<sup>(1)</sup> Several dynamic models were developed using springs, dash-pots, beams, and links to study vehicle-barrier collisions. Not only was this study successful, but it identified several guardrail safety problems. This research led to the improvement of the W-beam median barrier and the box beam guardrail designs used in New York.<sup>(2,3)</sup> Responses were predicted for vehicle impacts with rigid concrete barriers<sup>(4)</sup> and ultimately produced the Highway Vehicle Object Simulation Model (HVOSM), which has been widely used in the roadside safety community.<sup>(5)</sup>

In the 1970's, the BarrierVII program was developed to simulate impacts with flexible barrier systems.<sup>(6)</sup> This relatively simple two-dimensional code was very useful for many types of impacts but suffered from severe two-dimensional limitations.

GUARD, CRUNCH and NARD are barrier analysis codes that were developed in the 1980's.<sup>(7,8,9)</sup> These codes experienced a variety of problems related to coding errors, poor analytical formulations, and restrictive assumptions. As a consequence, they never achieved a vote of confidence from the roadside safety community. A great deal of pessimism was generated about the utility of analytical methods in roadside safety hardware design and evaluation that persisted into the 1990's.

In 1991, FHWA sponsored three independent projects to recommend a plan for developing improved roadside hardware analytical capabilities for simulating roadside hardware collisions.<sup>(10,11,12)</sup> It was recommended to abandon special-purpose analysis codes like NARD, GUARD, BarrierVII, and HVOSM in favor of the general-purpose nonlinear FE program DYNA3D.<sup>(13)</sup> At the time of this recommendation, the roadside safety community had virtually no capabilities or experience with general-purpose codes like DYNA3D. Building this base of capability and experience will take time and the assistance of LLNL, universities, and other resources.

While some aspects of the simulation effort have been frustratingly slow, an exceptional amount of progress has been made in the past 4 years. Properly implemented analytical methods can make a dramatic contribution to the improvement of roadside safety.

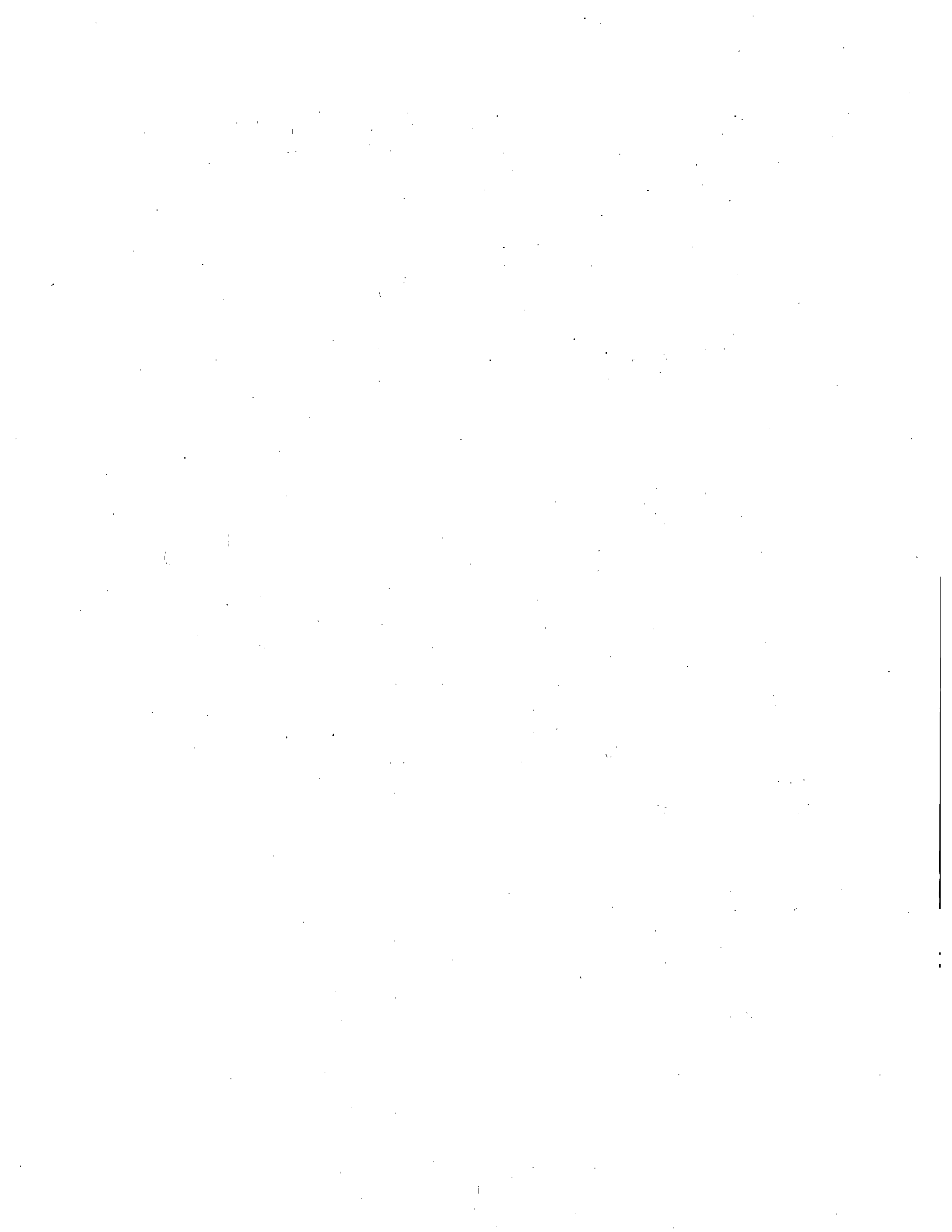
A variety of organizations, groups, and individuals has been involved in bringing nonlinear FE analysis (FEA) to roadside safety research. For many years, NHTSA has been funding research and promoting the use of these tools in crashworthiness and biomechanics research. FHWA has promoted both the use of these methods in roadside safety and closer collaborations with NHTSA during the past 4 years. This has resulted in a collaborative spirit that is beginning to link the FE work in both agencies. The end result may be a broader appreciation by both agencies of the FE methodology and its application to vehicle and barrier design.

The cooperative agreement established among FHWA, NHTSA, and LLNL is an important initial step to integrate FE technology into roadside hardware design and vehicle crashworthiness research. The working relationships established with the developers of the codes and experienced analysts have helped advance the community toward a higher level of expertise.

The following brief comments describe the work performed which is covered in more detail within the body of the report. In chapter 2, Software Development, the linking of DYNA with rigid body occupant codes used to model crash dummies was investigated. A link of NIKE to DYNA and the assessment of DYNA as a vehicle handling code required development of a simple tire model. It was established that DYNA could be linked to a real-time handling code and produced an estimate of the effort to complete such a link. A survey of material models needed to simulate the behavior of materials in crash dummies, human occupants, and necessary vehicle interior components was completed. The effort that would be required to implement the International Graphics Engineering Standard (IGES) capability into INGRID was evaluated. An unfolded airbag capability was implemented into DYNA to allow simulation of vehicle frontal crash with occupant interaction.

In chapter 3, all of the vehicle crash simulations are summarized for the linking of DYNA with MADYMO.<sup>(14)</sup> This includes the Ford Taurus model developed by an outside contractor and the effort required to debug a full frontal crash simulation. The moving deformable barrier model was enhanced for use in side impact simulations. In chapter 4, a model for crushable foam is described in detail. This has use in occupant/vehicle interior interactions. Also a cost estimate was produced to develop a usable safety glass model.

Chapter 5 covers simulations of vehicle impacts with roadside hardware. The Honda Civic model impact with rigid poles and a U-sign post was simulated and calculations compared with crash test data. The Honda model was refined, and the criteria for good vehicle model development was identified. A brief description is included of the efforts at FHWA to develop a small vehicle model, a breakaway cable terminal, and their interaction during impact. Chapter 6 describes the training and assistance provided to FHWA and NHTSA for the duration of this project and discusses the completed work. Finally, chapter 7 lists conclusions and provides recommendations for the future.



## CHAPTER 2: SOFTWARE DEVELOPMENT

### Section 1. DYNA3D & MADYMO link

A coupling of the nonlinear explicit FEA code DYNA3D with rigid body crash victim simulation (CVS) codes completed at LLNL is described. This coupling approach takes advantage of the structural response capabilities of DYNA3D and the validated occupant response abilities of the CVS codes. Two types of coupling were demonstrated, and a description of the equilibrium initialization method which was employed in the coupling development is also presented. An airbag capability, described later in section 7, was incorporated into this effort.

Rigid body dynamics codes like MADYMO and ATB can be used to predict the behavior of multiply connected rigid bodies during impact simulations.<sup>(14,15)</sup> These multiply connected rigid bodies frequently represent the anthropomorphic dummies that are employed to reproduce the response modes of human occupants during crash tests. A shortcoming of the CVS codes are the required force deflection curves for the ellipsoid-ellipsoid or the ellipsoid-plane contact models. These data sets are obtained experimentally and limit code validity to the tested range of materials and loading rates. Explicit FEA codes like DYNA3D are widely known for their ability to perform car crash response calculations.<sup>(13)</sup> Typically these simulations involve a description of the entire vehicle with minimal attention given to the vehicle occupants. FEA codes typically employ detailed constitutive relationships and sophisticated contact algorithms, which are based on known material parameters.

CVS and FEA codes form a spectrum of vehicle occupant simulations. At one end of this spectrum, a CVS code can be employed to simulate the occupant and occupant environment, with test data employed for loading responses and boundary conditions. At the other end of the spectrum, a detailed FEA representation of the vehicle and the occupant can be used to determine vehicle and occupant responses to crash situations. Vehicle FEA meshes have been available for some time but validated FEA occupant representations, e.g., a side impact dummy, are still in the development stage.<sup>(16)</sup> In between these two extremes lie one- and two-way coupled FEA/CVS code calculations. In a one-way linkage, the FEA code is used for the crash simulation. This calculation produces a description of the occupant environmental (passenger compartment) motion, which is used as an inertial reference frame motion by an appropriate CVS code.

A more detailed linkage involves constructing a FEA mesh, which includes a representation of the anthropomorphic dummy, the vehicle, and the impacting surface. As in the one-way linkage, the CVS vehicle occupant is assumed to be in a seat whose motion is prescribed by the FEA vehicle model. In the two-way linkage, the CVS code occupant movements are transmitted back to the FEA code during the simultaneous running of each code. The updated locations of the parallel CVS and FEA representations of the vehicle occupant are then employed by the FEA code for determinations of possible interactions of the occupant with the vehicle interior. The CVS occupant can be wearing a belt restraint system, and the vehicle can also contain an airbag. Coupling between the FEA mesh of the vehicle and the CVS occupant can occur in several ways; the most obvious is the impact of the occupant with the vehicle interior. Other possible couplings include the interaction between the anchorage points of the belt restraint system and the deformation of the vehicle during impact. This type of coupling could produce belt slack

which would in turn affect the occupant motion. In the two-way linkage, the coupled interactions are shared by both codes in the form of compatible sets of externally applied forces and displacements. Examples of one- and two-way linkages are given in the remainder of this report as well as a brief description of the linking algorithm employed.

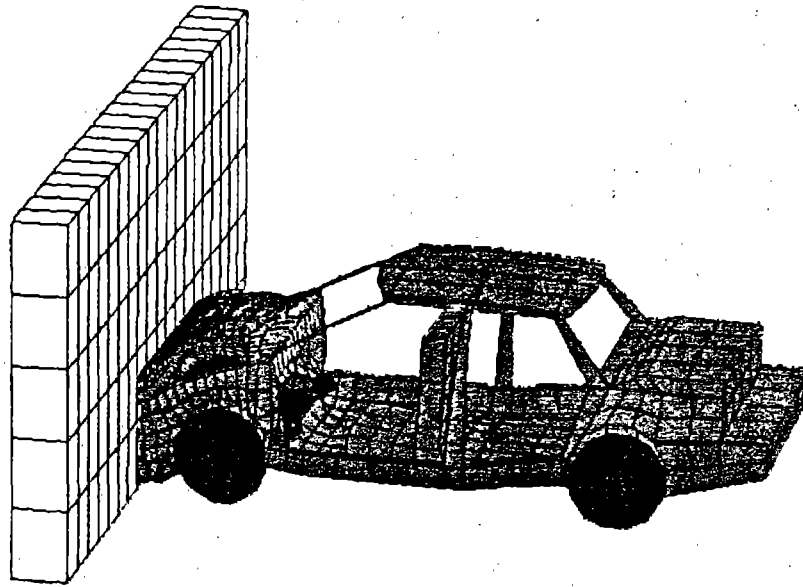
A one-way DYNA3D/MADYMO linkage is now described for a simulation of the impact of a 1991 domestic sedan into a rigid wall at 48 km/h (30 mi/h). This simulation employed a modified FEA mesh of a 1991 domestic sedan that was originally developed in a joint effort involving LLNL, FHWA, and University of Alaska faculty.<sup>(17)</sup> The original mesh development goal was to define a car in sufficient detail to capture pre-crash, impact, and post-crash behavior with a minimal number of degrees of freedom. Refinements to the vehicle mesh and contact descriptions were made for this study which raised the number of elements from 1,809 to 2,600. MADYMO was used to model the occupant interaction with the vehicle interior. The DYNA3D and MADYMO meshes can be seen in figure 1. For one-way linking, the DYNA3D occupant environment motions were used as boundary conditions for the MADYMO reference system consisting of the foot, ground, and seat planes shown in figure 1. Shown in figures 2 and 3 are acceleration time history comparisons between test data obtained from NHTSA<sup>(18)</sup> and DYNA3D calculations for the vehicle engine block and rear seat. The overall agreement of the calculations with the measured data lends credence to this type of coupling when the impact is straightforward and damage to the vehicle remains fairly localized. For this example, MADYMO calculated a Head Injury Criterion (HIC) number of 659 (a value of 1,000 is specified as a tolerance level in frontal impact), which can be compared to the measured HIC number of 633. The MADYMO HIC number was determined over the 38.7 to 50.7 ms interval of the calculated head acceleration time history. The measured dash panel peak acceleration of 34 g's can be compared to the MADYMO 3 ms (the highest linear acceleration level with a duration of at least 3 ms) value of 42.949 g's for the upper torso and 71.735 g's for the head. A peak head acceleration of 122 g's was also calculated by MADYMO.

It is generally accepted that there are three ways in which a dynamic linkage between an FEA and a CVS code can be achieved. These possible linkages include:

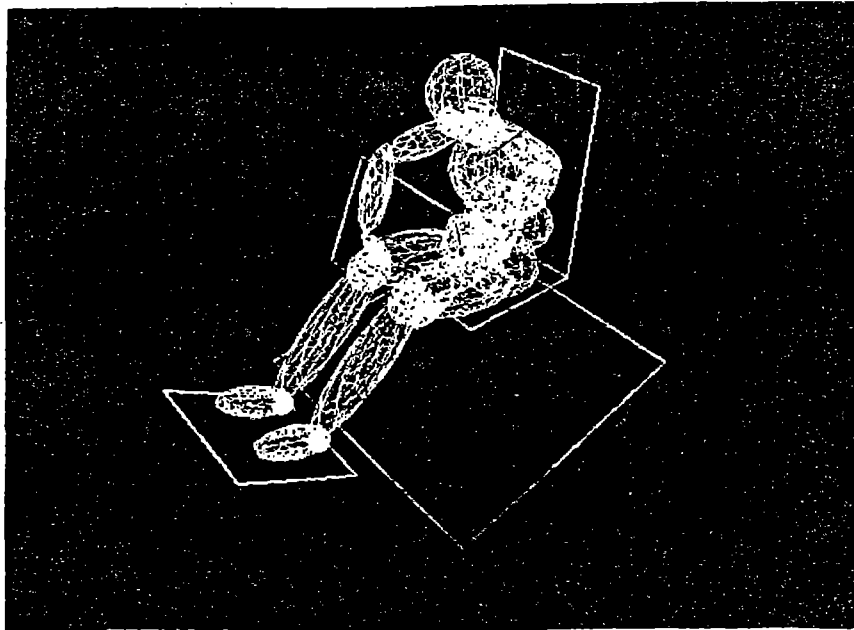
1. Installing both programs as overlays of new main program. This fully integrated coupling requires modifications to both programs as well as access to both source codes.
2. Developing a separate main program that acts as an interface between the two programs. This has the advantage that both programs can operate independently except for the data interchanges.
3. Coupling by means of an operating system; e.g., Parallel Virtual Machine (PVM).<sup>(19)</sup> A PVM interface would be unaffected by new code releases of either DYNA3D or MADYMO and each source code would remain under the control of its originators. Additionally, the coupling coding within each program would be fairly easy to implement and would have minimal impact on either of the codes future evolutions.

This last two-way linkage option was chosen as the most expedient method of coupling DYNA3D and MADYMO.





## DYNA3D Model



## MADYMO Model

Figure 1. One-way DYNA3D to MADYMO linkage results for the impact of a 1991 domestic sedan into a rigid wall at 48 km/h (30 mi/h).

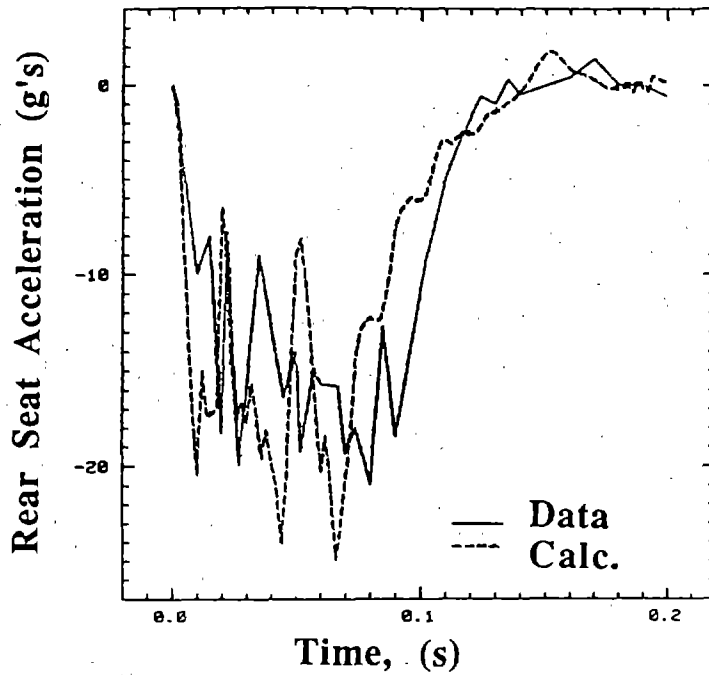


Figure 2. Correlation with accelerometer crash data for the impact of a 1991 domestic sedan into a rigid wall at 48 km/h (30 mi/h).

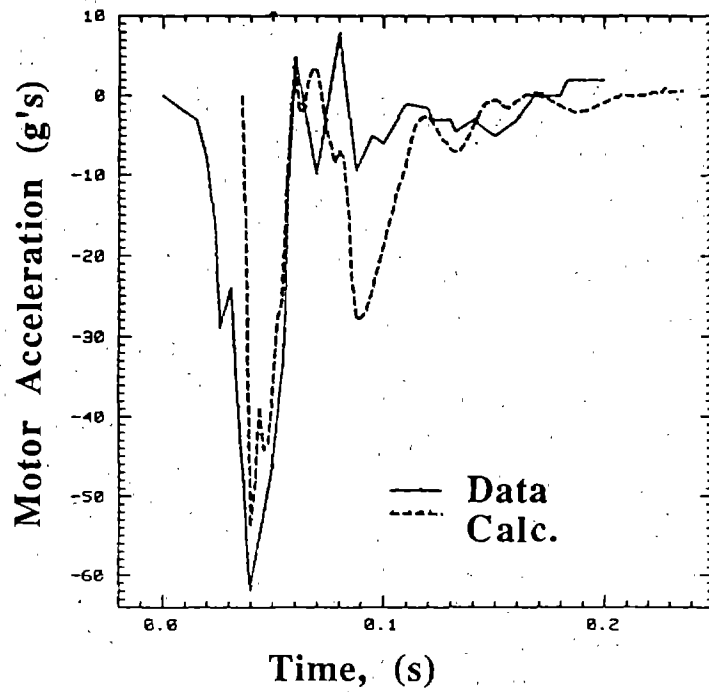


Figure 3. Calculated engine block acceleration for the impact of a 1991 domestic sedan into a rigid wall.

## Linkage Strategy

During dynamic coupling, CVS and FEA codes can exchange either kinematic or kinetic data sets for each linked rigid body. During kinetic coupling (from the DYNA3D viewpoint), MADYMO generated displacement and acceleration rigid body data at  $t_n$  is transmitted to DYNA3D which updates the position of its rigid bodies to  $t_{n+1}$ . This update is possible because of the explicit central difference time integration scheme which DYNA3D employs to advance between time steps. These updated positions are then checked for any contact forces which may arise as a result of the interaction of the rigid ellipsoids with the vehicle interior. The computed contact forces are then passed back to MADYMO as internal forces. In kinematic coupling, DYNA3D provides MADYMO with the position, velocity, and acceleration vectors of the rigid seats, belt, and airbag anchorage points. MADYMO in return provides DYNA3D with the resulting compatible force vectors at each of these points. Kinetic coupling between the two codes is the most straightforward to implement. The compactness of the scheme can be seen in the time integration coupling algorithm, described below and on the flow chart shown in figure 4. Kinematic coupling requires significant architectural modifications to both codes and for the time being, it remains a future task until sufficient demand arises for the kinematic interfaces described above.

- . DYNA3D advances its solution from  $t_n$  to  $t_{n+1}$ , updating the position of each ellipsoid center-of-gravity, c.g. (occupant position) using MADYMO kinematic data.
- . DYNA3D then computes updated nodal locations for each rigid ellipsoid.
- . DYNA3D computes contact forces and moments for each rigid ellipsoid nodal point and then computes equivalent forces and moments at the corresponding ellipsoid c.g.
- . DYNA3D passes these ellipsoid c.g. forces and moments and a new  $\Delta t$  back to MADYMO via PVM.
- . MADYMO receives the DYNA3D forces and moments as externally applied loads and updates its solution to  $t_{n+1}$  using the new  $\Delta t$ .
- . MADYMO passes the position and angular orientation of each ellipsoid c.g. back to DYNA3D at time  $t_{n+1}$  via PVM.

In the kinetic coupling strategy developed, the MADYMO environment can include the vehicle occupant, belt restraint system, rigid seat, and an airbag. The DYNA3D vehicle environment can include the ellipsoidal occupant and the passenger compartment details not included in the MADYMO environment, e.g., steering wheel or dash panel. A direct coupling scheme was employed in the coupling, i.e., a common time step ( $\Delta t$ ) is chosen by DYNA3D. This requires that the MADYMO time integration scheme be run in the fourth order Runge-Kutta constant time step mode. Future schemes could employ sub-cycling of the FEA code should this prove to be an inefficient strategy.

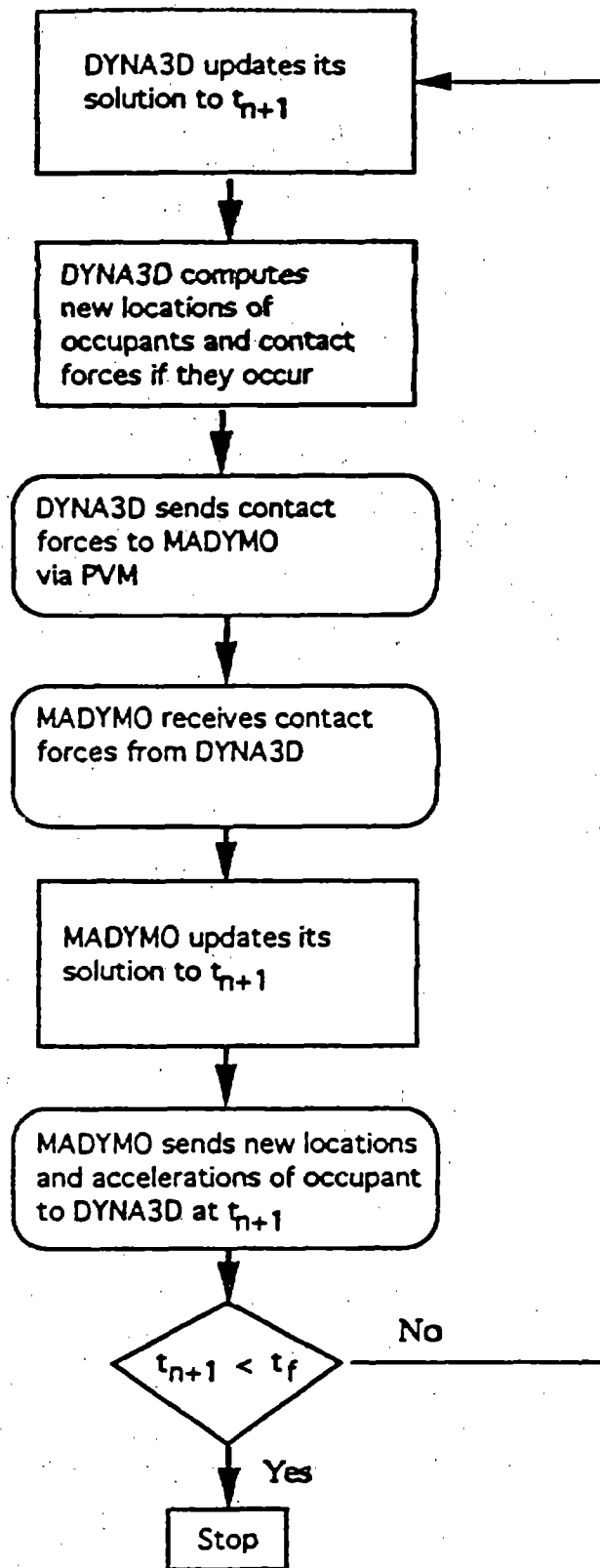


Figure 4. Flow chart of DYNA3D/MADYMO coupling algorithm.

## Static Initialization

The CVS and FEA occupant models must both be in the correct initial static equilibrium position prior to the transient analysis. For this initial coupling development, the static initialization was performed manually, i.e.:

- . An initial MADYMO calculation determined the occupant equilibrium position.
- . A translator code takes this initial MADYMO (or ATB) static equilibrium position and creates an INGRID input file that is added to the DYNA3D vehicle model INGRID file.
- . The resulting DYNA3D initialization assumes that other static loads on the model will not greatly influence the initial position of the common occupant ellipsoidal representations.

The accuracy of this scheme was verified by running the simulations presented in this report for a short time (before any impact occurred). The absence of observed induced dynamic oscillations verified the equilibrium stability of the static initialization scheme employed. More sophisticated schemes could be implemented if needed. Shown in figures 5 and 6 are MADYMO and DYNA3D representations of the Hybrid III and Eurosid dummies (standard validated dummies used in impact studies in the United States and Europe). The DYNA3D dummies were generated in the manner described above.

## Two-Way Linkage Examples

Two-way linkage examples were generated to demonstrate the linkage algorithm implementation. These examples are qualitative rather than quantitative in nature. Specific validation examples, such as those performed by the linked PAM-CRASH/MADYMO codes, are in progress.<sup>(20)</sup> The examples presented for this report include: a spherical shell impacting a wall, a belted Hybrid III dummy under simple deceleration, a Hybrid III dummy impacting a short wall, and the full frontal impact of a 1991 domestic sedan into a rigid wall with a Hybrid III vehicle occupant.

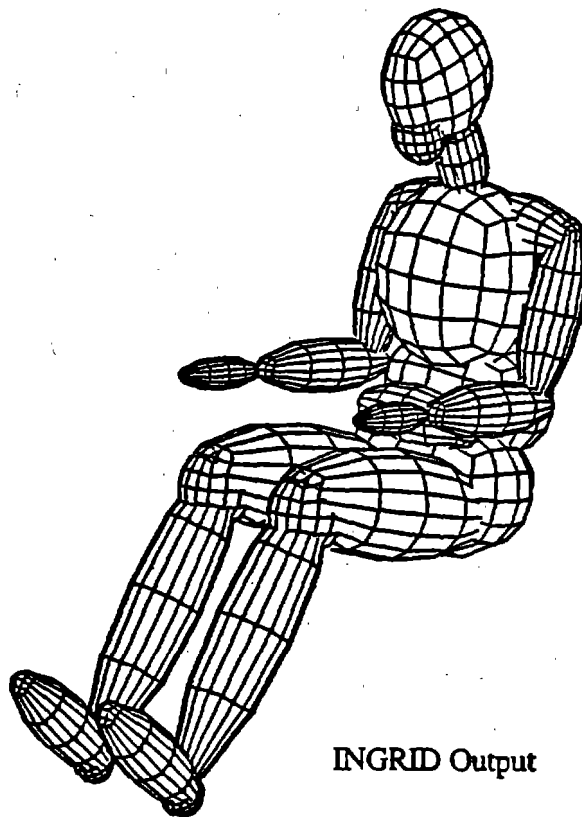
**Spherical Shell Impacting a Wall.** Shown in figure 7 is a single spherical shell impacting a rigid plane which is oriented at equal angles with each of the coordinate axes. Also shown in the figure are the symmetrical displacement time histories of the spherical shell center-of-the-mass. The symmetry of the displacements demonstrates the precision of the rotation/translation information interchange between MADYMO and DYNA3D.

**Belted Hybrid III Dummy Under Simple Deceleration.** To ensure that the coupling implementation was working correctly, an uncoupled MADYMO calculation was compared to a coupled DYNA3D/MADYMO calculation of the same event. The event chosen was the response of a belted Hybrid III dummy to a uniform deceleration. The results of this comparison are shown in figure 8 where identical positions of the dummy are produced from the uncoupled MADYMO and coupled DYNA3D/MADYMO calculations.

**Hybrid III Dummy Impacting a Short Wall.** A comparison of the results of an uncoupled MADYMO only calculation with the results of a MADYMO/DYNA3D calculation for the case of a Hybrid III dummy impacting a short wall at 6.7 m/s (15 mi/h) are shown in

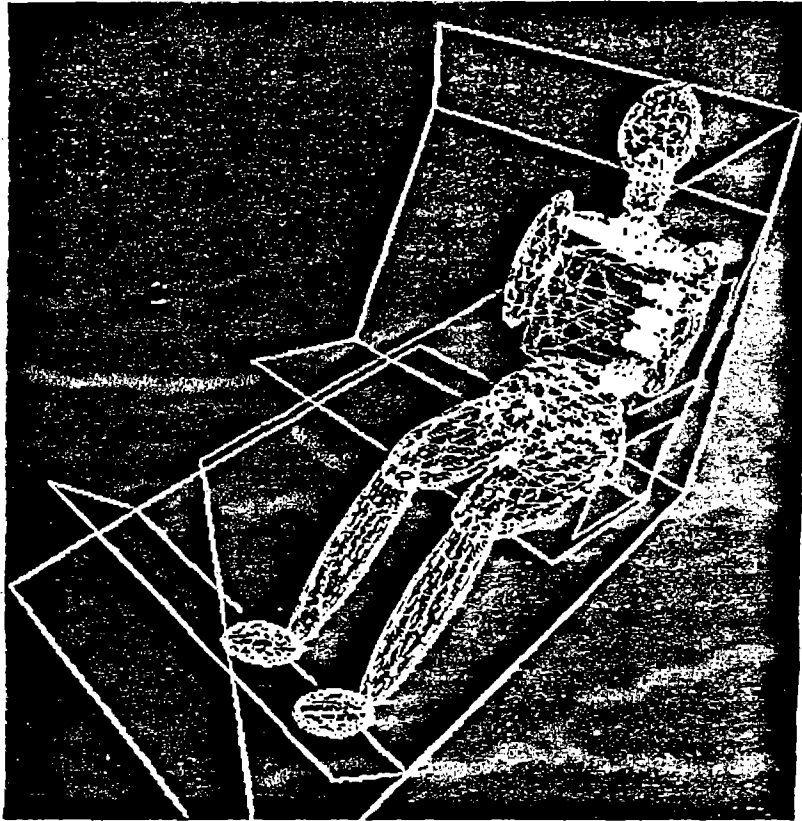


MADYMO Hybrid III Dummy

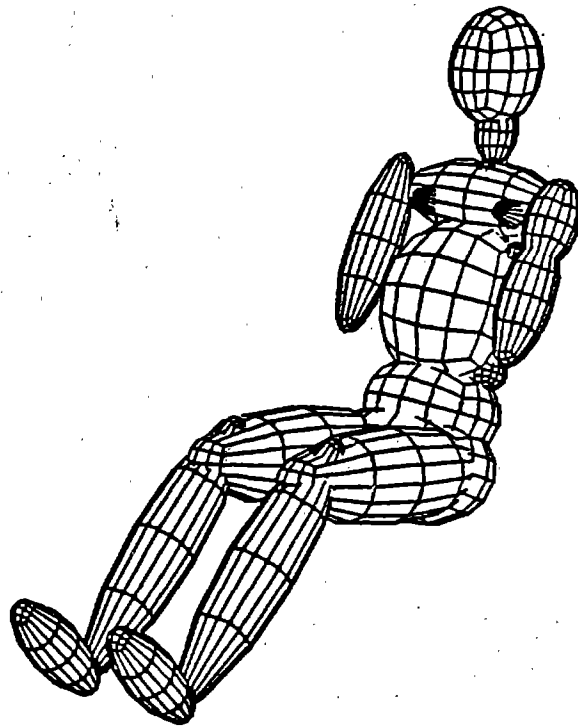


INGRID Output

Figure 5. MADYMO/INGRID Hybrid III representations.

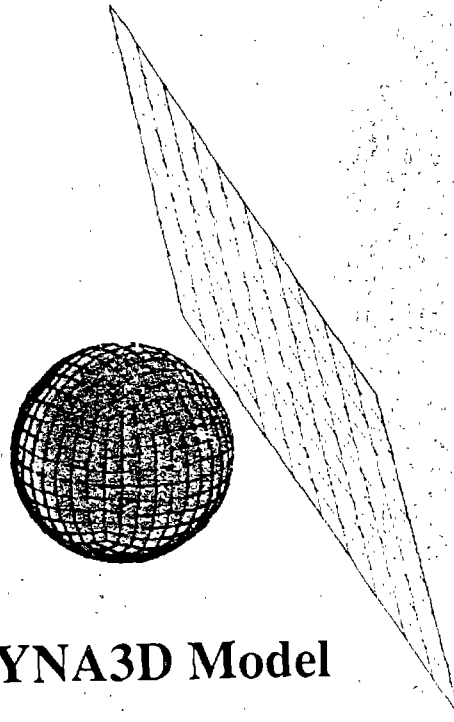


MADYMO Eurosid Dummy



INGRID Output

Figure 6. MADYMO/INGRID Eurosid representations.



## DYNA3D Model

Sphere returns to same spot upon rebound, verifying implementation of data transfer coding and DYNA3D contact force algorithm.

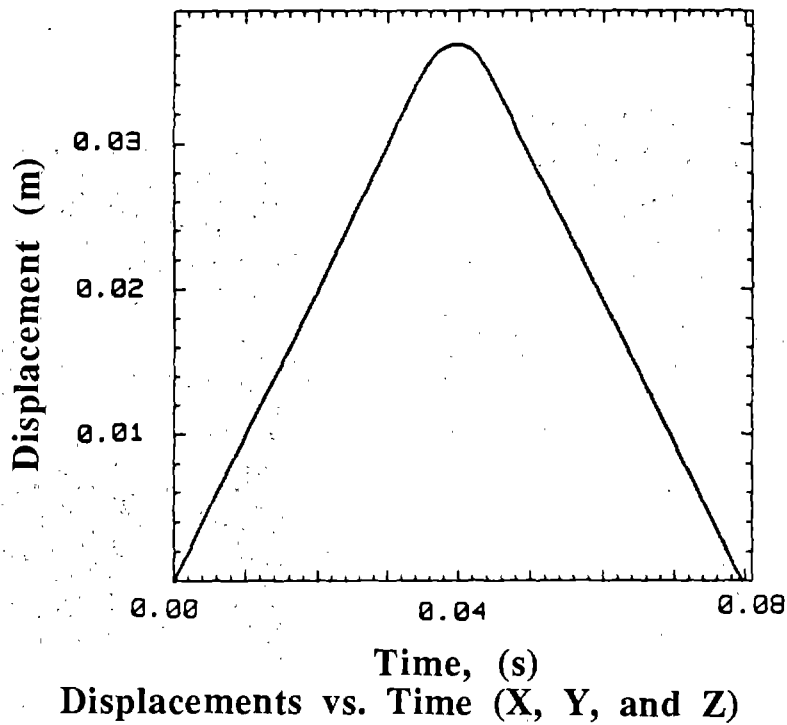
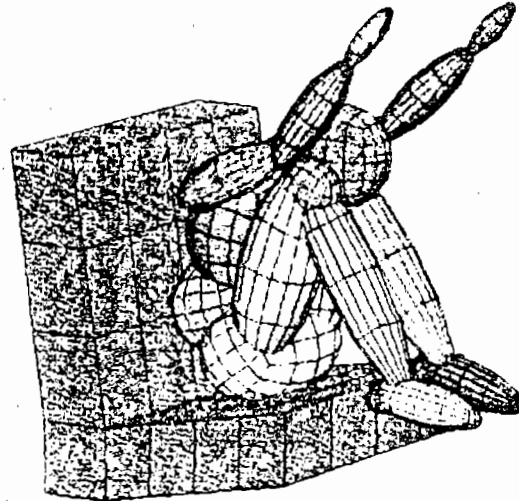


Figure 7. Two-way linkage example of spherical shell impacting a wall.



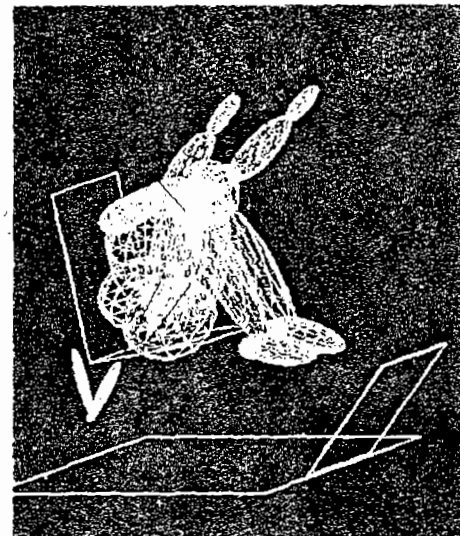


**MADYMO Only**



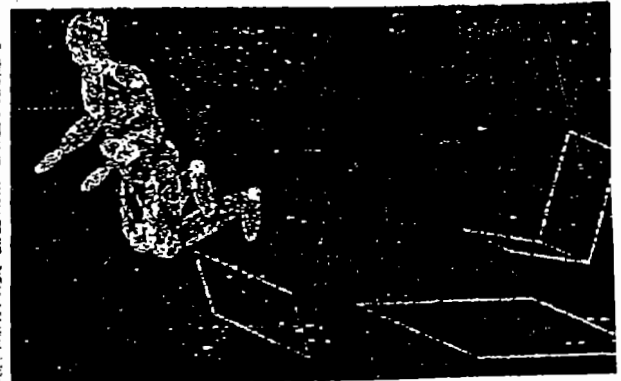
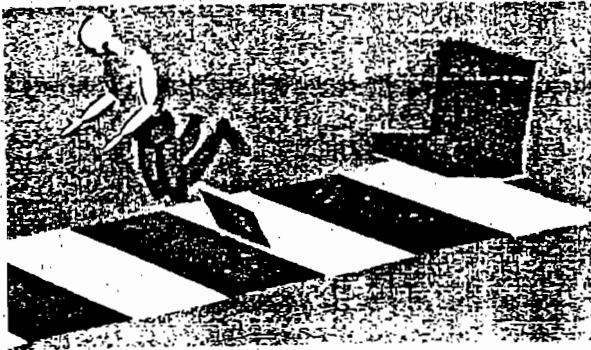
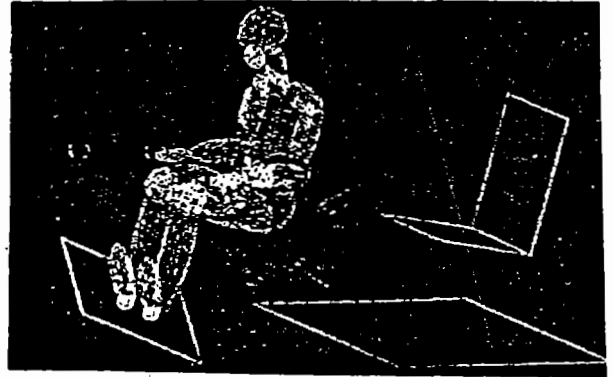
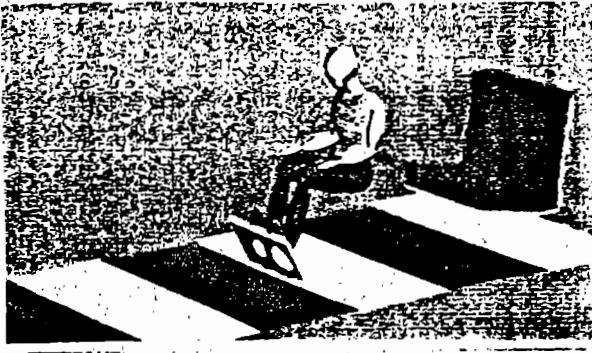
**Coupled DYNA3D**

**No external loading from  
DYNA3D. A check of the  
DYNA3D kinematic  
coupling implementation.**



**Coupled MADYMO**

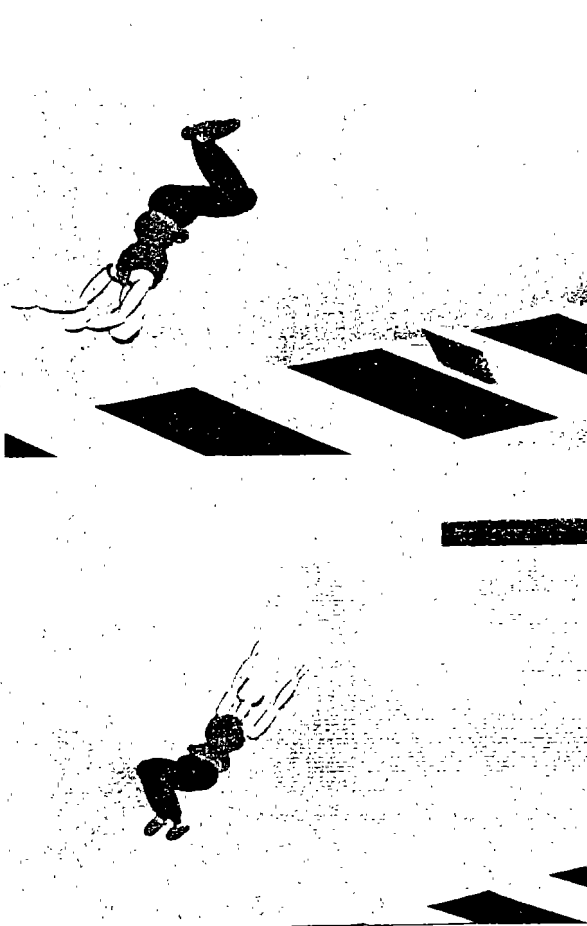
**Figure 8. Belted Hybrid III dummy under simple deceleration.**



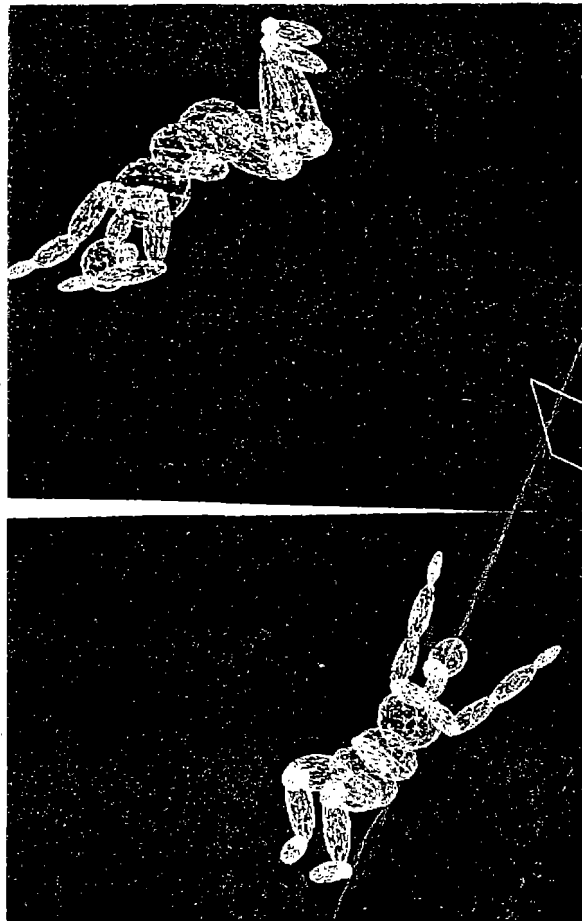
**Coupled Results**

**Uncoupled MADYMO Results**

Figure 9. Coupled DYNA3D/MADYMO only results from a Hybrid III dummy impacting a short wall.



**Coupled Results**



**MADYMO Only Results**

Figure 10. Further coupled DYNA3D/MADYMO only results from a Hybrid III dummy impacting a short wall.

figures 9 and 10. The impact in the coupled calculation was determined by DYNA3D and fed back into MADYMO to update the position of the tumbling dummy. A qualitative comparison of the results produced similar positions of the dummy after impact, verifying the DYNA3D linkage with MADYMO and providing a positive comparison of the DYNA3D and MADYMO contact algorithms for this situation.

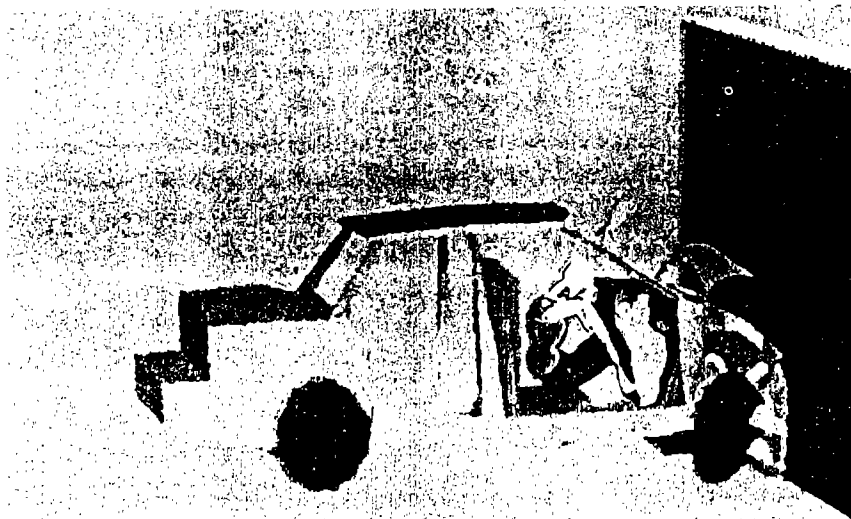
**Frontal Impact of a Sedan into a Rigid Wall with a Hybrid III Driver.** A MADYMO/DYNA3D calculation was performed for a crash simulation which included a model of a 1991 domestic sedan with a Hybrid III occupant which impacts a rigid wall in a full frontal impact at 13.4 m/s (30 mi/h). For this calculation, DYNA3D generated seat motion was employed as input for the MADYMO model of the seat belted Hybrid III dummy. During the calculation, the DYNA3D contact algorithms computed the force and moments on the dummy due to contact with dash panel part of the DYNA3D vehicle mesh. These contact forces and moments were then passed back to MADYMO which used them as externally applied loads to the appropriate parts of the MADYMO Hybrid III dummy. The deformed shape of the 1991 sedan with the Hybrid III passenger is shown in figure 11. This calculation was performed to demonstrate the feasibility of performing complicated linked calculations, including FEA vehicle representations that have been combined with rigid body ellipsoidal occupant representations.

DYNA3D/MADYMO coupling has been demonstrated by qualitative comparisons of uncoupled MADYMO and linked DYNA3D/MADYMO calculations of the same impact events. Future verifications will address comparisons and validations with measured experimental data.

## **Section 2. NIKE3D to DYNA3D link and assessment of DYNA3D as a vehicle handling code**

A plan was completed to develop a working linkage from NIKE to DYNA with an acceptable tire model tested for a simple vehicle collision into a rigid barrier.<sup>(21)</sup> An automatic transfer from the rigid body DYNA to the FE DYNA is not a trivial task and was not part of Pre-VISTA. The NIKE-DYNA link is a static link. This section describes the effort required to develop a DYNA-NIKE link which does not currently exist.

A preliminary version of NIKE now has a simple tire model installed. The vehicle crash simulation transfer from NIKE to DYNA still has some limitations. The link does not include initial velocity transfer. DYNA is restricted to the same material models as in NIKE. LLNL exercised DYNA using a simple rigid body model with large time steps. A problem was identified related to the approximation in DYNA for angular velocity which requires small time steps to ensure accuracy. A methodology is recommended for simulating rigid body handling with a tire model before and during the crash event. The following describes the effort to link NIKE and DYNA with handling capability.



**Two-way linked DYNA3D/MADYMO results.**

**Figure 11. Frontal impact of a sedan into a rigid wall with a Hybrid III occupant.**

## **DYNA Link to NIKE with Handling Capability**

A discussion at LLNL on the topic of linking a handling version of the NIKE code to DYNA before and after impact identified a work description that would meet several different time frames. The basic procedure is to hand-off vehicle handling information from NIKE to DYNA at the time of impact and then subsequent post-impact hand-off from DYNA to NIKE.

This effort will not require the use of a specific Real-Time Handling (RTH) code. FHWA has not yet selected a RTH code. LLNL can start and complete the linking of NIKE for pre and post impact to DYNA before the RTH code decision. After completing these links, FHWA can decide on the RTH code of choice and whether the selected code should be linked to DYNA using the above developed capability.

The recommended approach described below is a multi-step process. The current suspension systems need to be identified and defined. The failure mechanism needs to be specified. The final step is to implement results of the first two steps into both DYNA and NIKE and then demonstrate a manual link.

There are two distinct time frames for this activity. The first is to develop a NIKE to DYNA link to simulate pre-impact handling and enable more complicated pre-impact handling including damaged suspension and wheel impact with obstructions before the vehicle impacts more substantial roadside hardware. The second is to develop a DYNA to NIKE link with the capability to simulate post-impact handling with limited damage to the suspension. LLNL estimates 6 man-months for the NIKE/DYNA link and 18 man-months for the DYNA/NIKE link.

LLNL needs to identify the definition of suspension types and the degrees of freedom (DOF) required for handling. The vehicle model will use NIKE's rigid body capability for those portions of the vehicle related to handling requirements. The remaining portion of the vehicle will be modeled as deformable elements. Based on our current understanding of vehicle handling, the vehicle should have 6 DOF (3 translation, 3 rotation) for the sprung mass (vehicle), 4 vertical DOF (1 at each wheel), and 1 steering DOF for a minimum of 11 DOF. The four spin DOF (one angular at each wheel) are not necessary since braking and tire-pavement friction can be handled by input tables before impact. This allows faster execution on the computer since NIKE will not be limited to 10 degrees of wheel rotation for each time step. Also, NIKE has the capability to have four independent steering DOF. LLNL recommends using an individual with vehicle dynamic handling experience for guidance on vehicle handling issues. LLNL will decide how best to define tire-pavement friction, effects of braking, etc. for implementation into NIKE and DYNA.

LLNL will take the results and implement into NIKE3D and DYNA3D a suspension system model which is defined in terms of available one-dimensional, two-dimensional, three-dimensional, and discrete elements. FHWA will recommend which suspension type to model for this task. Once this information is obtained, LLNL will initiate implementation of a link for a case of handling followed by impact into a barrier. Presently, a static load NIKE/DYNA link exists. One must add inertial terms to make this a link for the vehicle impact simulation. LLNL will first develop a working manual link.

This will be followed by development and demonstration of the link for several different handling situations. This will allow more complicated pre-impact handling of tire plowing in soil, impact with a berm or tire rupture (air-out) by NIKE before handing off to DYNA for the impact phase. The previously mentioned pre-impact complications are all nonlinear and will require a large increase in cpu time.

### **DYNA/NIKE link**

This task focuses on linking the two LLNL developed codes to simulate impact and handling with or without damaged vehicle suspension. No DYNA/NIKE link capability exists. For NIKE to function as an RTH code, LLNL must add rotational inertia. At present, it only has rigid body translational inertia. This is also required for completion of the NIKE/DYNA link but only needs to be done once. FHWA will identify two generic suspension types and the most likely failure mechanisms and limits for these suspension models. A description of the phenomenology of the damaged suspension system is required. Assuming that DYNA can adequately model suspension failure, a judgment will be made on how to represent adequate tire-pavement models for handling with damaged suspension. This effort may require some suspension response behavior tests to obtain additional modeling information for DYNA and NIKE. LLNL will work with FHWA to determine how to implement this information into NIKE to simulate post-impact real-time handling with a damaged suspension. The NIKE post-impact handling will be defined entirely using rigid bodies and no further damage to the vehicle or suspension is possible. LLNL will provide a sample calculation to verify coding integrity.

The proposed project will not provide automatic linking of the codes. Automatic linking means that only the user defines the initial pre-impact NIKE input file and all decisions on when to switch to DYNA for impact and back to NIKE for the post-impact handling are taken care of automatically by internal coding. After gaining experience using the manual link capability, FHWA can decide on the automatic issue. The advantage in selecting the manual link approach is that the two codes, DYNA and NIKE, can continue to be the same public versions that are used for all other problem applications. If the automatic feature is desired, the result will be a code that is not the same as the public versions and consequently will be more difficult to maintain.

### **Section 3. RTH and DYNA link**

The original intent was to develop a linkage (via manual data or dump files) and run a demo problem with an RTH to DYNA (impact) to RTH hand-offs of a 96 km/h (60 mi/h) and 20 degree barrier impact. After discussing coupling strategy and coupling implementation issues with FHWA, LLNL obtained a C version of VDANL for porting to an SGI workstation platform. LLNL worked on a proof-of-concept calculation employing the Festiva FEA mesh obtained from FHWA. The mesh was modified to define a deformable sprung vehicle with four unsprung wheel/tire masses. The masses were then driven separately by exterior loading functions to simulate the type of input which is expected from VDANL. This manual hand-off was to investigate vehicle handling due to changes in vehicle c.g. In late 1994, FHWA decided not to pursue development of this link. Instead, FHWA instructed LLNL to complete an estimate to develop this capability.

The following covers the topic of linking an RTH code to DYNA before and after impact. The basic procedure is to hand-off information from an RTH code to DYNA at the time of impact, with the subsequent post-impact hand-off procedure to be developed as part of VISTA. This effort requires the use of a specific RTH code. Even though FHWA has not selected an RTH code, LLNL can complete an estimate for the task of linking an RTH code to DYNA. The recommendation was to choose an interim RTH code to allow an early start on this project. After FHWA decides on the RTH code of choice, the linking procedure can be adapted to the selected code without any extensive additional effort.

The recommended approach described is a multistep process. The current suspension systems need to be defined and the failure mechanism specified. The final step is to implement results of the first two steps into DYNA and demonstrate a manual link as described in chapter 2, section 1. There are three distinct time frames for this activity. The first is to develop an RTH to DYNA link. The second is to develop a DYNA to NIKE link with the capability to simulate limited damaged suspension and subsequent post-impact handling. The third and final activity is to develop an RTH-NIKE-DYNA link to simulate pre-impact handling, more complicated pre-impact handling including damaged suspension, and impact. LLNL estimates the effort to be 6 man-months for the RTH/DYNA link and 6 man-months for the RTH/NIKE/DYNA link. This discussion assumes that the work outlined in chapter 2, section 2 (DYNA/NIKE link), has been completed.

### **RTH/DYNA link**

This task will use an LLNL-selected RTH code. LLNL needs to identify the definition of suspension types and the DOF available in this RTH code. Our current understanding is that the RTH code should have 6 DOF (3 translation, 3 rotation) for the sprung mass (vehicle), 4 spin DOF (1 angular at each wheel), 4 vertical DOF (1 at each wheel), and 1 steering DOF for a total of 15 DOF. LLNL needs to obtain an RTH code in C or FORTRAN for use on a workstation or mainframe computer. LLNL needs documentation sufficient to define the governing equations of a generalized suspension model and examples of specific classes of suspensions. The equations and relationships will be written down and then LLNL will seek advice from FHWA for any recommended improvements or changes. LLNL will work with FHWA to develop an understanding of how best to define tire-pavement friction, effects of braking, etc. for implementation into DYNA.

### **RTH/NIKE/DYNA link**

This activity will focus on linking the FHWA chosen RTH code to DYNA and NIKE to DYNA. This will include the capability to simulate handling with damaged suspension. This will allow more complicated pre-impact handling of tire plowing in soil, impact with a berm, or tire rupture (air-out) by NIKE before handing off to DYNA for the impact phase. Since LLNL will have already linked a representative RTH code to DYNA, the linking of the chosen RTH code to NIKE should be straightforward. The other part of this task focuses on linking NIKE to DYNA as has been described in chapter 2, section 1. Presently, a static NIKE/DYNA link exists.



#### Section 4. Tire model in DYNA consistent with NIKE and RTH

LLNL developed and investigated the basic elements of a tire model and assessed implementation into DYNA. LLNL investigated technology development for an integrated package for the analysis of vehicle handling and vehicle impact into roadside features and other vehicles. This program at LLNL on Tire, Accident, Handling, and Roadway Safety (TAHRS) provided technical advances for use in Pre-VISTA.<sup>(22)</sup> This work has involved integration of handling and deformation codes, development of material and tire models, and comparisons of our results to test data. Only the work relating to the tire model and steering will be highlighted. The long-term goal is to model a rotating tire and simulate wall climbing behavior on a New Jersey type barrier.

In preparation for the linkage of RTH and FEM codes, a steering force boundary condition was added to NIKE3D. The lateral forces generated by each tire can be computed by the inclusion of a tire model subroutine in NIKE3D. The vector diagram in figure 12 illustrates how NIKE3D computes the lateral load on the tire. Simulating the road as a stone wall, NIKE3D first determines the vertical load on the tire. Then, using the user-input driver steering angle, the vehicle orientation direction, and velocity, NIKE3D determines the tire slip angle. NIKE3D then uses a complex tire model to determine the lateral load as a function of these variables. Figure 12 shows top views of a car model during two simulations. Identical driver input is used: the wheel is turned first to the left, then to the right. The 40 km/h (25 mi/h) simulation results in a circular path; in the 72 km/h (45 mi/h) case, the car skids into an unstable oversteer condition.

LLNL also developed a simple rigid-body vehicle handling code to demonstrate the linkage both to NIKE, DYNA, and a user interface. This resulted in a 10 DOF model with each suspension element represented by a spring and damper, as is each unsprung mass. The tire forces are modeled using the Dugoff tire model and are limited using the friction circle concept. Control of the vehicle during a run is currently accomplished by completing tables in a data file. Vehicle velocity can be controlled by specifying a desired speed or by inputting a table of driving forces vs. time. Steering likewise, can be controlled in two ways. One way is to specify a table of steering angles vs. time, and the other is to specify a table of x-y coordinate pairs representing the desired path of the vehicle. An imbedded steering controller will then attempt to follow the path as closely as possible. This vehicle handling code was used to simulate an idealized vehicle traversing a simple closed road circuit.

The code calculated the position and yaw of the vehicle, the suspension forces on the tires as the car follows the path, and the normal, longitudinal, and lateral forces experienced by the tires. This steady-state, vehicle-handling algorithm was improved by the addition of a bending correction to the anti-sway-bar equations and subsequent performance calculations for a prototype chassis design. Calculations demonstrated the unusual behavior of the near-constant-power for this electric powertrain in forward acceleration. In terms of lateral acceleration, LLNL demonstrated the potential for oversteer given the initial target of near 50/50 weight distribution if road camber at the front is held near zero (using negative roll camber). This scenario develops as one proceeds from condition (A) to (B) in figure 13, which shows the progression of lateral g's with oversteer angle. Condition (C) shows the effects of adding a large, front anti-sway bar, resulting in high cornering g's but with development of understeer in the limit to avoid unstable handling behavior as in (B).

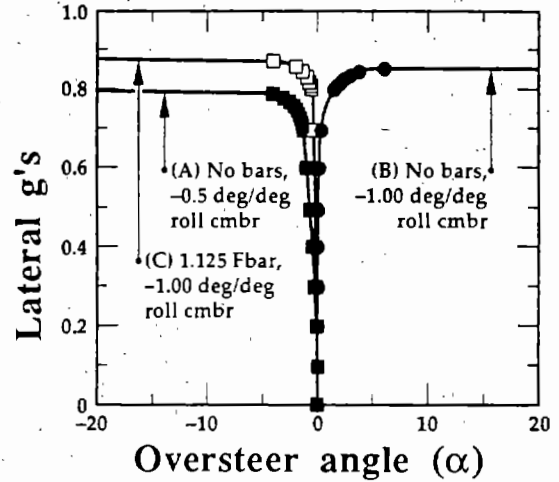
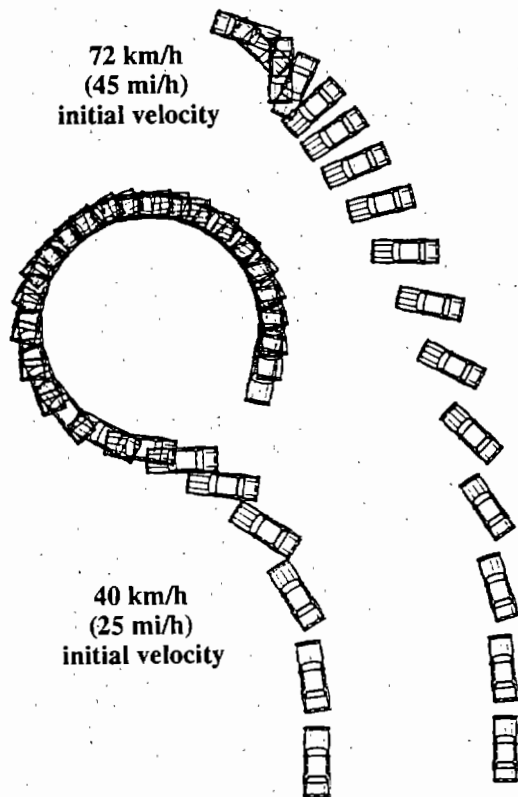


Figure 13. Lateral acceleration (steady-state skid-pad) for the prototype electric vehicle scenarios.

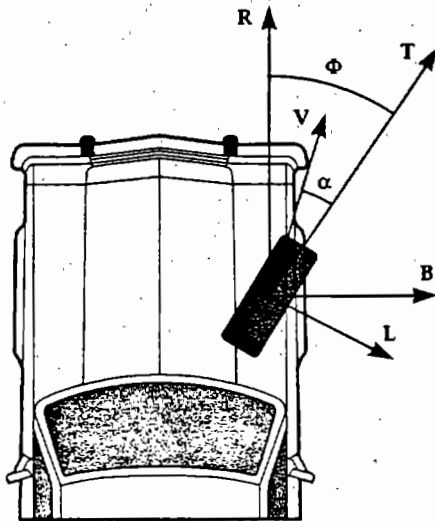


Figure 12. Implementation of steering algorithm and lateral tire force in NIKE3D. (Steering is 20 degrees left at  $t=0.2$  s, then 20 degrees right at  $t=2.0$  s. Vehicle responds differently as a function of velocity.)

This successfully demonstrated that a relatively simple tire model can simulate the tire forces as a vehicle traverses over a flat surface. Insight has been gained into the needs for additions and refinements to this basic tire model. This work has pointed the way to development of compatible tire models for DYNA and NIKE.

## **Section 5. Summary of material constitutive models used for vehicle/occupant interaction**

LLNL reviewed literature and contacted experts in the crashworthiness technical community to identify material modeling capabilities and needs for improving vehicle simulation with occupants. These would enable realistic simulation of human body models and crash dummies for occupant interaction with the vehicle interior during a vehicle crash. Where possible, constitutive equations were identified in tentative form with tangents amenable to implicit formulation. The following is a preliminary evaluation of current DYNA and NIKE material models and their application to occupant, and dummy components using FEA. Recommended implementations into DYNA/NIKE to represent human and dummy material behavior are included.

The Side Impact Dummy (SID) and the Hybrid III are very complex engineering systems used to assess the risk to human passengers of various scenarios in transportation accidents. This assessment relies on being able to determine the time history response of various components of the dummies. Using the NIKE/DYNA codes to perform time history predictions of a similar nature, requires sophisticated models both from a geometrical standpoint and a material standpoint. The current focus is on the suitability of the present material models in NIKE/DYNA for such applications.

The dummies are made of a variety of different materials. There are many metal components for which it is fairly certain that DYNA can provide adequate models given that this has been, historically, the main use of DYNA. There are however several rubber and plastic parts in the dummies for which it is not clear that adequate models exist in the codes. To name a few, there are parts made of butyl rubber, natural rubber, vinyl plastisol (a polyvinyl chloride coating compound), vinyl nitrile, urethane, and urethane foam. These materials behave, in general, in a nonlinear fashion in both the small deformation regime and the large deformation regime. In the small deformation regime, the nonlinearity is due to the viscoelastic nature of the materials; and in the large deformation regime, the nonlinearity is due to the viscoelastic nature of the material and to the nonlinear mechanism of polymer chain stretching and folding that goes on when one deforms such a material.

Material model issues are also important for modeling human anatomy where the combination of geometry, motion, and human tissue pose additional difficulties in simulating actual behavior. The motion characteristics of human joints are complex and three-dimensional in nature. The actual motion patterns depend partly on the anatomical arrangements of the bony and ligamentous constraints that dictate the freedom-of-motion characteristics. In addition, they depend partly on muscle activity during a particular function, which determines the actual motion patterns within the passive motion envelope. Hence, understanding the relationships between anatomical and structural properties on the one hand, and passive motion characteristics on the other, is important for the study of joint biomechanics in general.

As a mechanical system, joint motion is an effect of internal and external forces. The external forces are effects of muscles, gravity, and accelerations, and applied directly to the bones outside the articulating region. The internal forces are generated by articular contacts and ligament constraints and depend on the relative motions of the joint, the geometry, and ligament properties. This same characteristic governs the forces in all of the tendons, muscles, and ligaments associated with a particular joint and its motion.

Ligaments are composed of densely packed collagen fibers, while cartilage material is a highly hydrated soft tissue capable of undergoing very large strains (up to 50%). In the knee joint geometry, the meniscus is interposed between the femur and tibia, and its material properties are somewhere between cartilage and ligament, with radial and circumferential collagen fibers in a semi-permeable matrix. Its function is to distribute and transmit load between the articulating surfaces. This is just one example of the complexity found with any particular joint region.

### **DYNA/NIKE Material Model FEA Summary**

A review of the literature on the SID materials in the library indicates a general lack of well-accepted material models for these materials. In the area of human tissue, a reasonably good data base exists, and one can make judgments on material model selection based on the behavior of each particular tissue. However, based on the degree of modeling detail desired, there still exists a need for material model behavior that does not currently exist in NIKE/DYNA. Neglecting the vast complexities associated with the modeling issues involved, a review of the available material models in NIKE/DYNA can provide a hint of the current suitability of NIKE/DYNA for such analyses and can provide a direction for future developments. An overview of material models is presented below for possible use for this project and for human tissue with appropriate comments for each material model. These material models can be used for analysis of impact dummy containing plastic and rubber parts and human soft tissue. Each overview indicates the availability of each model in NIKE or DYNA.

#### **# 1 Elastic**

**NIKE/DYNA**

To use this model, you need to record or determine the Young's modulus and Poisson's ratio of the material. This provides the crudest and most basic level of material response. For the present situation, it can be used when no other information is available.

#### **# 2 Orthotropic Elastic**

**NIKE/DYNA**

Depending on the manufacturing technique of the SID materials, it is easy to imagine that some will be anisotropic especially for the skin. Often this kind of anisotropy is orthotropic in nature. This can be an adequate model for representing anisotropic bone characteristics. The testing for this model requires nine material constants.

#### **# 3 Isotropic Elastic-Plastic**

**NIKE/DYNA**

This model could possibly be used to model bone for situations where anisotropic behavior is not important. It can be used for any material that exhibits plastic behavior for loading in excess of yield. The required constants can be obtained from a standard uniaxial tension test. The key difference between metals and human tissue or bone is during unloading. Metals return following a much different path than during the load application resulting in a

large open hysteresis loop. However, tissue or bone unloads very close to the load application path.

# 5 Soil and Crushable Foam

NIKE

This model allows for the specification of a nonlinear pressure vs. volumetric strain relationship. Volumetric unloading can include volumetric crushing. The three required constants can be determined from a triaxial compression test. Deviatoric response is elastic-perfectly plastic with pressure dependent yield stress.

#6 Viscoelastic

NIKE/DYNA

In this model, the bulk behavior is assumed to be elastic and the deviatoric behavior is given by short and long-time shear moduli with a single relaxation time for defining the transition between the two. This model is a large deformation version of the Standard Linear Solid for all intents and purposes.

# 7 Blatz-Ko Hyperelastic Rubber

DYNA

This model requires the least number of material properties, namely, the shear modulus. Internally, it sets Poisson's ratio to .463 in the constitutive relationship between volume, strain, and pressure to approximate incompressibility of a certain degree. Since this model requires so few properties, it can be used when very little is known about the material to be modeled.

# 13 General Anisotropic Thermo-Elastic

NIKE

This allows three different options for specifying the relationship between the three material axes. This could be useful for certain bone behavior simulations. The required constants can be obtained from simple uniaxial material tension tests in the orthogonal directions. The shear terms require uniaxial tests at a 45-degree rotation in their respective two-dimensional planes.

# 16 Concrete and Geologic Material

DYNA

Despite its origins, this model can possibly be used to model foam like materials in a zeroth order sense. This can be done by forcing an elastic overall response coupled to a stiffening bulk response using an equation of state to model the pore collapse in the material.

# 27 Compressible "Mooney-Rivlen" Hyperelastic Rubber

NIKE/DYNA

This material provides the basic nonlinear elastomer behavior and should be considered the first order model for the polymeric dummy materials. It requires tests for the two Mooney parameters and an estimate of the compressibility of the material. This would be a good choice for a good isotropic simulation of human tissue behavior. In NIKE, this is model #15, and it can be specified to be incompressible, as is the case with many human tissues.

# 31 Frazer-Nash Hyperelastic Rubber

DYNA

This model is a generalized strain energy Taylor series expansion of the free energy function with up to 10 coefficients that can (according to the developers) be determined from three standard tests.

This allows different properties in three different axes and uses the 1948 Hill orthotropic plasticity model. While the model may include linear or nonlinear strain hardening, this is not an issue for human tissue. Most of the required constants can be obtained from simple uniaxial material tension tests in the orthogonal directions. The shear terms require uniaxial tests at a 45-degree rotation in their respective two-dimensional planes.

### Recommendations

It is somewhat difficult to identify which models will work well for the different materials. It is clear that models for the basic behaviors exist, but that good models are perhaps lacking because they have not been formulated. To improve the suitability of NIKE/DYNA for such analyses, the following improvements should be considered.

1. For viscoelastic behavior of SID materials, the DYNA viscoelastic model should be extended to multiple relaxation times. This is important since impact-like loads tend to have a very broad frequency content and the materials concerned have complex frequency responses that are difficult to model with single relaxation time models.
2. The rubber materials should be extended to handle multiple relaxation time viscoelastic effects. This will provide a major increase in the suitability of DYNA for the proposed use. While the viscoelastic model provides for these viscous effects, it is still deficient in its ability to accurately handle the large deformation response of the polymeric materials.
3. A model for the urethane foam needs to be added to DYNA. The use of model #16 for this purpose is far too crude. A preliminary literature search did not turn up any candidate models. Thus, a more thorough computer literature search will be required to expose any candidate models, otherwise a new model will have to be developed.
4. An orthotropic hyperelastic model for human tissue needs to be added to NIKE. To accomplish this will require a significant effort (perhaps 1 to 2 man-years) by an experienced material model developer.
5. The strain energy density function ( $W$  for NIKE #15 hyperelastic model) needs to be recast for more general terms (not strain invariants) of experimental relationships. Some of these exist in the literature. It would take several months to achieve this. The advantage would be to make it easier for literature models to be implemented into NIKE.
6. The logical extension would be to combine the fourth and fifth recommendations to produce an anisotropic hyperelastic NIKE model with the strain energy function expressed in simple experimental relationships. Again, achieving this will require a very significant effort (2 man-years) by an experienced material model developer.
7. Most of these models will require plane stress formulations so that they can be used with shell elements.
8. Better, more modern elastomer models may have to be added to NIKE/DYNA. While this development can be done on an as-needed basis, the effort required is open ended (several months to years).

## Section 6. Evaluate IGES Implementation into INGRID

LLNL has assessed the effort to modify INGRID to accept IGES files. This is a multi-step process starting with modifications to surfaces that INGRID is familiar with. The completed upgrade will have the capability to display and erase surfaces, map a mesh to a discrete surface, read discrete surfaces from Computer-Aided Design (CAD) packages, read Analytic and Nonuniform Rational B-Spline (NURBS) Surfaces as defined by IGES, and map a mesh onto these same surfaces. The effort required to accomplish all of the above is estimated to be 2 man-years. This estimate can change depending on the refinement of the actual work definition and will depend on the person selected to perform the work.

This defines a plan to add the capability of INGRID to read IGES formatted files and map a mesh onto the defined surfaces in the IGES files. The following outlines the required tasks. An estimate of the number of man months (labor) required to accomplish each task follows the description. Each task involves software development including design, implementation, and testing as well as updating the INGRID user's manual.

All estimates consider the following caveats concerning this plan.

1. The plan was based on limited interviews of a few LLNL researchers. A more thorough research should be done as part of each task to fully understand the requirements before committing to this plan.
2. It is assumed that the code developer implementing this plan is knowledgeable of IGES and INGRID.
3. The code developer will work full time on this project.
4. Some software may exist that can be used to reduce the 2 man-years effort estimate.

As with any other product, developing requirements for each version of the IGES and each implementation are different. Before any work can be done, the version(s) and implementation(s) must be identified as well as the subset of the IGES to be addressed by the project. For example, which type of surfaces will INGRID accept? The following estimates will change as the requirements are better defined.

Display Surfaces (4 man-months) This task includes modifying INGRID to display and erase surfaces with which INGRID is already familiar. The following capabilities could be provided:

1. Print general surface information.
2. Display all or some of the surfaces.
3. Remove display of all or some of the surfaces.

Other interactive commands such as rotating, scaling, and translating must also apply to surfaces.

Map Mesh to Discrete Surfaces (6 man-months) Implement an algorithm to map a mesh to a discrete surface using either parallel projection or closest point.

Read Discrete Surfaces (4 man-months) Modify INGRID to read discrete surfaces. With the above tasks and this task completed, CAD packages, such as ProEngineer, can output their geometry data as discrete surfaces and INGRID could input these files and map a mesh to these surfaces.

Read NURBS (4 man-months) Add to INGRID the capability to read files containing Analytic Surfaces and NURBS as defined by the IGES.

Map Mesh to NURBS (6 man-months) Develop and implement an algorithm to map a mesh onto Analytic Surfaces and NURBS.

## **Section 7. DYNA3D Airbag Capability**

LLNL has developed and implemented a thermodynamically based unfolded airbag model within the explicit FE code DYNA3D.<sup>(23)</sup> This development is an adjunct to the DYNA3D/MADYMO coupling development described in section 1 and will provide a more complete visualization of the DYNA3D results of these coupled calculations. The governing differential equations for the airbag gas dynamics are derived from fundamental principles and are integrated using an unconditionally stable, but highly precise and computationally effective algorithm. The implementation permits airbag representation with existing element types, material representations, and contact technologies. Airbag inflation initiation occurs automatically when nodal or rigid-body accelerations within the simulation exceed a prescribed threshold and dwell time. This new feature enhances DYNA3D's ability to accurately resolve occupant/vehicle interactions during nonlinear, highly dynamic crash simulations. An example is presented that demonstrates the performance of the airbag algorithms and illustrates the necessity for a thermodynamically based model.

Maintaining passenger safety in modern, lightweight automobiles requires accurate resolution of both passenger and vehicle responses during nonlinear, highly dynamic impact events. Automobile airbags reduce occupant injuries by mitigating the transmitted force between the occupant and the vehicle interior. The proven effectiveness of airbags, coupled with the need for faster and more cost-effective engineering, has placed an additional requirement on the numerical simulation of vehicle crashes. It is now essential to model the occupant, the vehicle, and the airbag system in vehicle crashworthiness simulations.

Numerical simulations of both vehicle crashworthiness and vehicle/structure interaction (e.g., a car impacting a barrier wall) are commonly performed with LLNL's three-dimensional, explicit, nonlinear, FE code DYNA3D. To better resolve human occupant responses during crash simulations, a thermodynamic airbag system has been modeled and incorporated into DYNA3D. The newly developed airbag model is intended to capture the complex occupant/airbag/vehicle interactions after initial airbag deployment (i.e., after initial unfolding), and gives the analyst enhanced freedom in airbag discretization, material representation, and contact algorithms.

Airbag systems operate by sensing the vehicle's dynamics. When the vehicle's dynamics, e.g., its forward acceleration at one or more locations, exceed a threshold level for a specified time period, inflation is initiated. Gas then flows from the inflator into the airbag, causing the airbag to unfold, fill, and eventually deflate. A typical airbag inflation/deflation cycle lasts approximately 50 to 100 ms. The internal airbag pressure



depends upon both the inlet gas conditions and the occupant/airbag/vehicle interaction forces in a nonlinear manner, because gas continuously escapes from the airbag via orifices and skin leakage.

DYNA3D's airbag system was developed in four phases. First, the basic thermodynamic relationships governing the gas behavior within the airbag were identified. Second, the set of differential gas equations was cast in a manner consistent with the existing FE framework and solved using a numerically efficient and accurate algorithm. Third, the entire airbag system was tied into DYNA3D, and user-specified variables were established. Finally, using the new DYNA3D airbag system, representative airbag simulations were run, and the results were compared against other, previously validated, standalone airbag models. Following is an overview of each of these aspects.

### **Thermodynamic Formulation**

The fundamental equations governing airbag behavior were derived directly from thermodynamic and fluid dynamic principles and parallel the approach developed at General Motors.<sup>(24)</sup> A control volume was constructed coincidental with the airbag wall's instantaneous interior location. It is assumed that the airbag cycle is an adiabatic process and that a single, uniform gas state exists everywhere within the airbag. These assumptions allow a single, isentropic, ideal gas relationship to represent the gas behavior inside the control volume. The thermodynamic variables that define the airbag's internal gas state are the instantaneous temperature and pressure. These quantities are related to the airbag's instantaneous volume and total mass via the ideal gas law.

Gas flows both into and out of the airbag during deployment. The inlet flow is characterized by the absolute inlet temperature and inlet mass flow rate. Exhaust gas leaves the airbag through orifices and skin leakage. The exhaust rate depends upon the absolute ambient pressure, the exhaust orifice area, the head loss coefficient, and the airbag deformation. As the airbag skin stretches, the exhaust orifices and leakage vents generally increase in size. To account for this phenomenon, the exhaust area is modulated by the relative orifice area.

Two coupled differential equations describing the rate of change of the airbag's internal temperature and mass were derived. The conservation of mass principle combined with use of the control volume form of the first law of thermodynamics (conservation of energy) results in an energy balance expression.<sup>(25)</sup> Accepted expressions for enthalpy and internal energy are defined in terms of physical constants and the gas temperature. It is assumed that constant volume specific heat and the constant pressure specific heat are linear with respect to temperature and depend upon effective constant and linear coefficients. Next, an expression that relates the exhaust flow rate to the differential between the interior and exterior airbag pressures was derived. Integration of Euler's equation along a streamline that passes through a sudden expansion yields the exhaust flow rate expression.<sup>(26)</sup> These relationships were used to solve the governing equations are solved for the rate of change in mass and temperature as a function of the airbag system specifications for volume, initial temperature, and pressure.

The derived relationships were numerically evaluated at each time step after airbag inflation has begun. The pressure is determined from the current airbag volume, the relative

orifice deformation, and the integration of the differential equations for mass and temperature. This pressure is then applied as a pressure boundary condition on the interior airbag surface in the usual explicit FE manner.

The instantaneous airbag volume is obtained from using a surface integral definition. The integration is performed over all exterior surface segments, using the current segment's centroidal position vector and the segment's outward normal vector. The rate of volume change is approximated using the previous value and a first-order difference formula.

The set of governing differential equations for mass and temperature are integrated in time using a trapezoidal rule with error checking and automatic subcycling. A forward Euler/backward Euler integration method was used to define the governing equations using values for the mass and temperature at the current time and current timestep increment to solve the updated values. The Newton-Raphson iteration procedure was selected for rapid convergence. The advantage of this integration method is that it is unconditionally stable, so its accuracy can be controlled independently of the timestep size used to solve the global DYNA3D problem.

The incorporation of an airbag system into an occupant/airbag/vehicle FE simulation is straightforward. The analyst develops a discretized representation that now includes one or more deflated airbags. (The current implementation requires that each airbag contain a small but finite initial volume.) Any existing DYNA3D material model or element formulation can be used to represent the airbag skin. This freedom provides the analyst with complete control over the airbag's representation. For each airbag, the analyst provides inflation trigger information, an optional exhaust-hole segment number, the effective orifice area, effective gas constants, the ambient pressure, and two load-curves that define the temporal inlet temperature and flow rate relative to the start of inflation. The analyst must also define a list of segments that completely encloses the airbag volume. Because the user prescribes the temporal inlet temperature and flow rate, any inflator can be represented, and both mono- and polyspecies inflator gases can be modeled.

During the analysis, airbag inflation commences when the user-specified node or rigid-body acceleration exceeds the prescribed threshold for the minimum required dwell time. This relieves the analyst of prescribing *a priori* when the airbag should inflate. The governing equations are integrated once, and the internal airbag pressure is then applied to all segments that define that airbag.

An example illustrates the fundamental behavior of an airbag and demonstrates the necessity of a thermodynamically correct airbag model in crashworthiness FE simulation. In this example, the occupant's head, idealized as a rigid sphere, impacts a standard driver's side airbag. The bag is attached to a mounting disk that, in turn, is fastened to a rigid steering column, as shown in figure 14. Representative inflator gas properties and profiles are used. Standard contact surfaces, defined between the sphere and airbag, the airbag and itself, and the airbag and mounting plate, simulate component interaction. The orifice is located at the center of the bag; no elements exist in the orifice hole. An initial vertical velocity is imposed on the sphere, and airbag deployment is initiated by gently plucking one of the airbag nodes at 10 ms into the simulation.

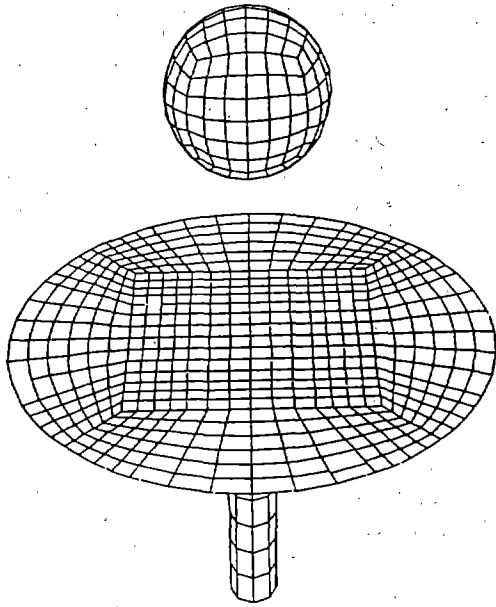


Figure 14. Initial airbag configuration. (Shown are the airbag, mounting plate, steering column, and impacting sphere).

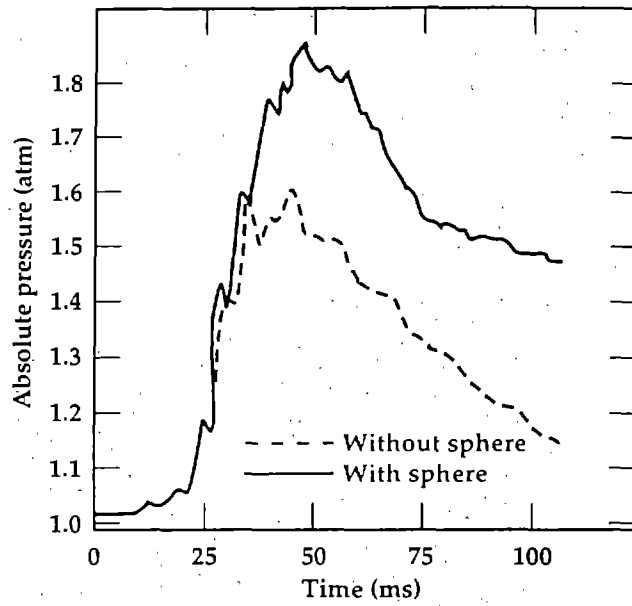


Figure 15. Internal airbag pressure during representative inflation cycles. (The response is shown for an airbag with and without an impacting object.)

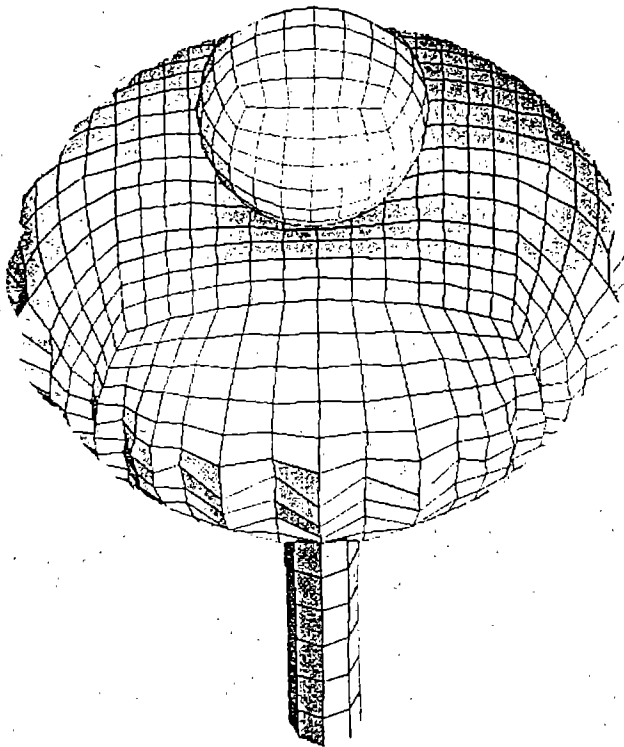


Figure 16. Partially inflated airbag during contact with a rigid sphere.

Figure 15 shows the airbag's internal pressure vs. time for similar simulations performed with and without an impacting sphere. Note, the drastic increase in peak pressure and change in chronological behavior that occur, because the sphere contacts the airbag. Therefore, simulations performed by assuming *a priori* an airbag pressure profile can lead to grossly inaccurate results. The deployed airbag and sphere are shown during contact in figure 16. Note how the airbag cradles the sphere.

The current airbag model has been compared with other experimentally validated airbag models, using the same geometry, initial conditions, and inflator profiles. The results from the different airbags were essentially identical. A more complete description of the previous sample problem, along with the validation study, can be found in Kay and Zywicz.<sup>(27)</sup>

Although much research still needs to be performed to fully understand and quantify airbag behavior, several topics directly applicable to this work should be considered. Comparisons with experiments that use realistic, topologically complex, contacting surfaces should be made. This validation is important since vehicle designers must correctly understand the actual force distributions transmitted to the occupant. Next, while the current approach provides an apparently reliable engineering tool, the limitations and consequences of using an airbag formulation that assumes isotropic interior-gas conditions need to be formally established.

## CHAPTER 3: DYNA-MADYMO VEHICLE CRASH SIMULATIONS

LLNL in collaboration with NHTSA has studied two of the FE vehicle models that have been developed for NHTSA to aid in their understanding of occupant responses to vehicle crashes. A part of the collaboration included refinements that were made to a 1990 Ford Taurus frontal impact mesh which allowed that mesh to be run with DYNA3D. Another study included the generation of a mesh which simulated a Taurus crash with an anthropomorphic crash dummy occupant. This simulation coupled DYNA3D to the rigid body CVS code MADYMO.<sup>(14)</sup> Effort was also expended to validate DYNA3D simulations of the moving deformable barrier (MDB). This barrier was developed for NHTSA to provide a convenient and repeatable method of applying impact loading in vehicle crash tests. As a result of working with the NHTSA Taurus and MDB FE vehicle meshes, improvements were made to DYNA3D to improve its crash simulation ability. It was also determined that a restart capability for linked DYNA3D/MADYMO calculations is a necessity for complex simulations on current workstations.

### Section 1. Frontal Taurus model

LLNL obtained PATRAN,<sup>(14)</sup> generated a DYNA input file of a simple vehicle, and ran DYNA to demonstrate the use of PATRAN at LLNL. LLNL also purchased the PATRAN/DYNA translator. Unfortunately, the contractor that developed the mesh initially used their own translator, which was not compatible with the purchased translator, in the production of the first Ford Taurus meshes. After establishing that another difficulty in working with the vehicle model was the new PATRAN version P3, a request for the older version P2.5-5 (which did work with the Taurus neutral file) was made. This allowed some modification of the frontal model contact descriptions, but reworking of the PATRAN neutral file was still limited by not having the original PATRAN generation command sequences. However, these limited changes were rendered moot by the introduction of automatic contact algorithms in DYNA3D.

### Section 2. Debug frontal impact Taurus model

A contractor-developed version of the Taurus frontal impact mesh was obtained from NHTSA with the intent of running a full frontal impact simulation with DYNA3D which could be compared to available test data. The first task was to debug this large full-size model. After changing the input file to be compatible with DYNA3D requirements, an initial run was attempted. This DYNA3D run terminated after less than 0.001 s due to *flying nodes*; i.e., nodes that have been given unrestrained or greatly exaggerated restoring forces because of perceived or actual surface penetrations by the automatic contact algorithm in the analysis code. Treatment of this meshing difficulty is now briefly discussed, as well as changes that were made to DYNA3D as a result of the Taurus full frontal impact simulation.

Newly installed penetration detection options in DYNA3D identify initial nodal penetrations, the penetration distance, and the normal to the master surface segment that had been penetrated. Using the output from this new option, a code was written that moved the offending nodes to more physically realistic locations. This methodology reduced the number of offending nodes in the Taurus mesh from approximately 1,400 to 110. These remaining nodes were then removed from the automatic contact surface for the remainder of the calculation.

Problems were also encountered in the original Taurus mesh with solid elements that were defined with a reduced number of nodes (with respect to the original element formulation). These degenerate elements included wedges and tetrahedrons with incompatible DYNA3D solid element connectivities. Triangular shell elements were also encountered in the Taurus mesh, which did not take advantage of the DYNA3D triangular shell element formulation. These elements were defined as degenerate quadrilateral shell elements, which can lock up and give overly stiff results.

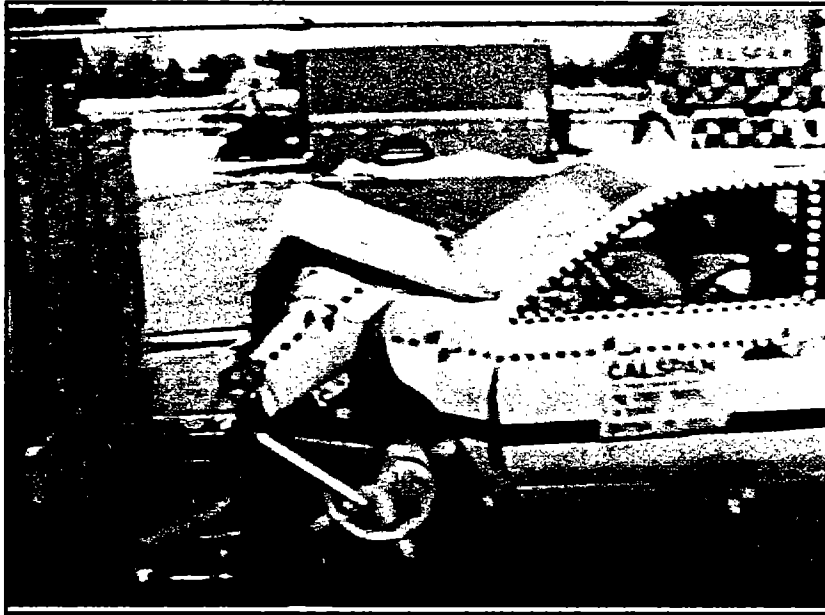
As a result of the Taurus frontal impact calculation, many improvements were made to the DYNA3D automatic contact algorithms. These improvements included the treatment of constrained nodal pairs, triangular shells, solid/shell interfaces, and re-entrant corners in the mesh. New automatic contact options that were added to DYNA3D include the debugging aids for interpenetration mentioned above and constraints on the region of automatic contact activity by spatial windows and material identifications. DYNA3D fixes were also made to the nodal constraint/spot weld options, rotational updates of rigid materials, and miscellaneous restart bugs.

### **Section 3. Frontal impact crash simulation**

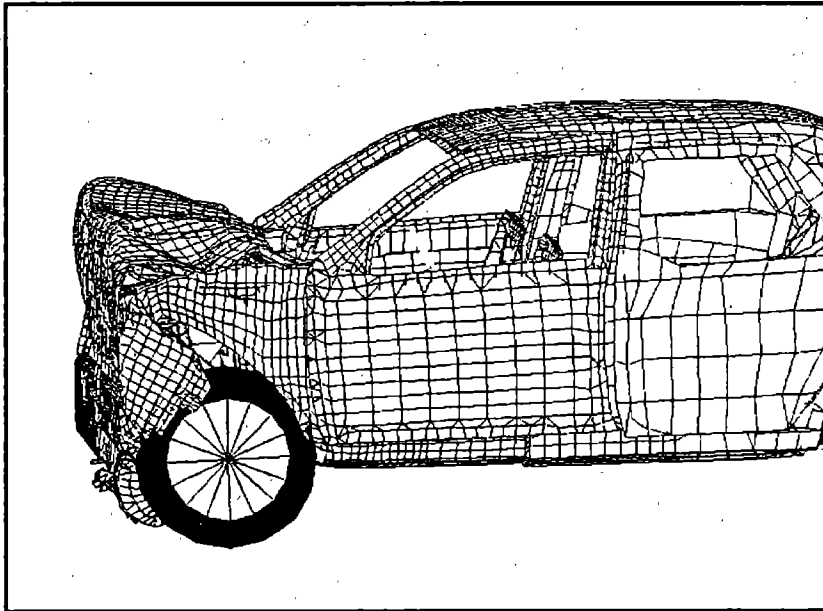
LLNL compared DYNA simulations of frontal NHTSA barrier crashes using the large full-size frontal Ford Taurus model and a rigid barrier. This enabled verification of the Ford Taurus vehicle model. Full frontal calculations were performed using the DYNA to MADYMO link described in chapter 2 for simulations of a vehicle impact containing an occupant. A recent upgrading of MADYMO at LLNL will require a revised DYNA to MADYMO linkage effort before continuing with full-scale linked calculations. Depending on hardware platform availability, the completion time has a large uncertainty. LLNL completed the simulations of two impact models with no linkage and a full frontal linked calculation with a dummy. DYNA input files and example problem results are available for each simulation.

A comparison of test results with DYNA3D results for a full frontal impact of the Taurus sedan into a rigid wall at 56 km/h (35 mi/h) can be seen in figure 17.<sup>(29)</sup> Verification of the simulation includes the calculated deformed shape comparison with the final crash shape that is shown in figure 17. A further verification of the DYNA3D simulation can be seen in figure 18, which compares the calculated engine accelerations with the measured values. As can be seen, the correlation is quite good, with the exception of a small calculated perturbation at 93 ms (most probably caused by an element failure criterion being invoked by DYNA3D).

Next, LLNL set up a DYNA file to simulate a vehicle containing an occupant crashing into a rigid wall. Nonlinear explicit FEA vehicle meshes have been available for some time but validated FEA vehicle/occupant interactions are still being developed. Vehicle/occupant simulations can currently be achieved through coupled FEA/CVS code calculations. These coupled simulations take advantage of the structural response capabilities of the FEA codes and the validated occupant response capabilities of the CVS codes.



**Post-test photograph**



**DYNA3D calculation**

Figure 17. Results of Taurus full frontal impact at 56 km/h (35 mi/h).

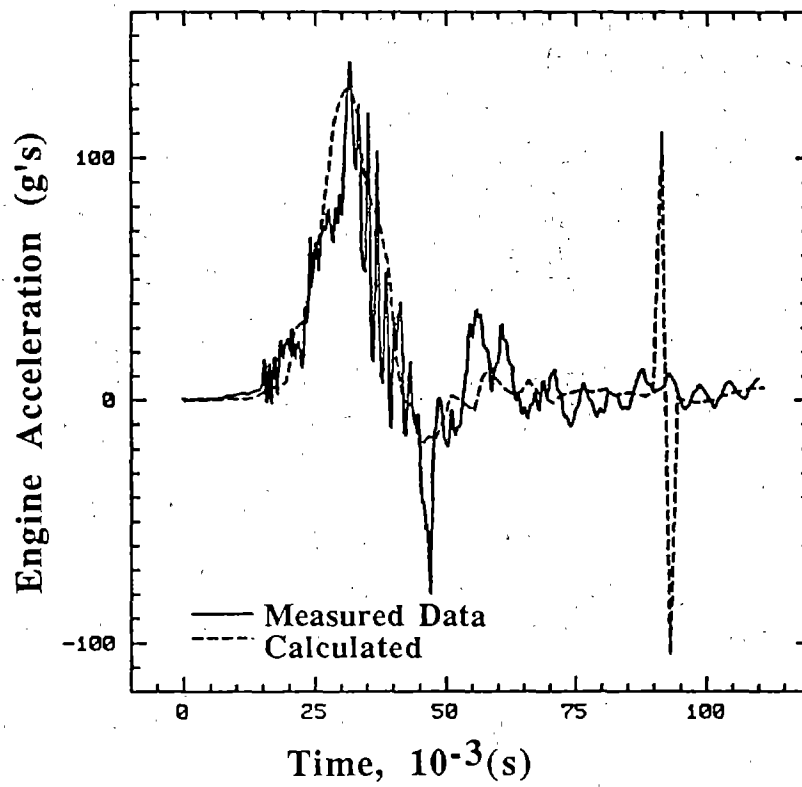


Figure 18. Comparison of engine acceleration test data with DYNA3D results for a Taurus full frontal impact at 56 km/h (35 mi/h).



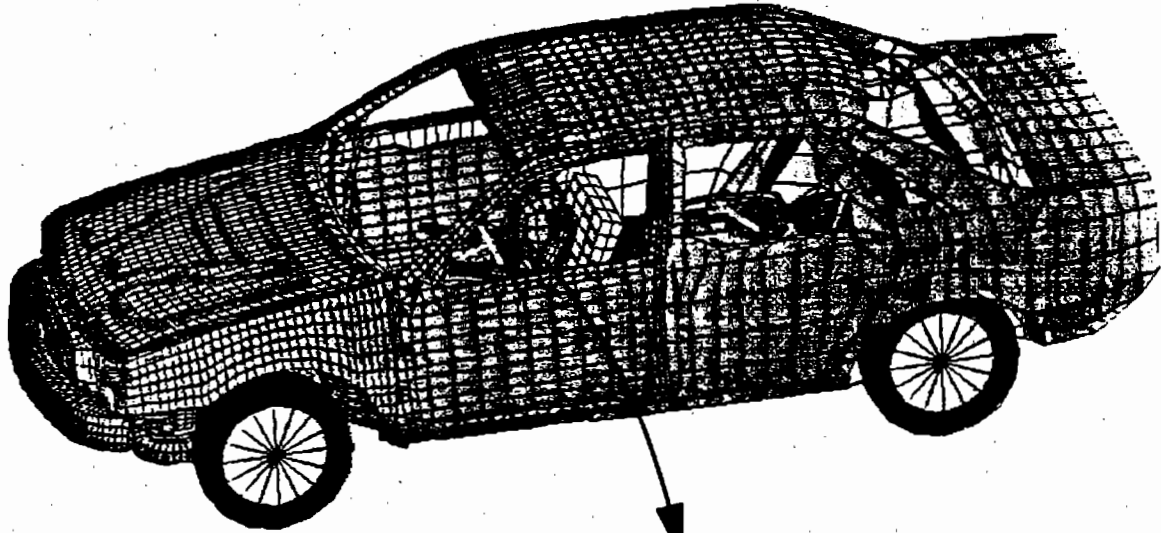
## DYNA3D/CVS Code Linkage Methodology

In the current DYNA3D/CVS coupling, the CVS environment includes the occupant and belt restraint systems. The DYNA3D environment includes an FE representation of the anthropomorphic dummy occupant and vehicle details not included in the CVS environment; e.g., steering wheel, dash panel, and air bag. The CVS occupant motion is with respect to the fixed inertial system of the FEA mesh. Coupling between the FEA code and the CVS code occurs by the interaction of the occupant with the vehicle interior. The coupled interactions are in the form of compatible sets of externally applied forces and displacements during the simulation. The codes communicate via a PVM (parallel virtual machine) library which allows each source code to remain under the control of its originators and is fairly easy to implement.<sup>(30)</sup> The initial occupant equilibrium position is determined by the CVS code. A translator code processes this initial data and creates an INGRID input file that is used to generate a DYNA3D input file with an FEA representation of the CVS occupant.<sup>(31)</sup>

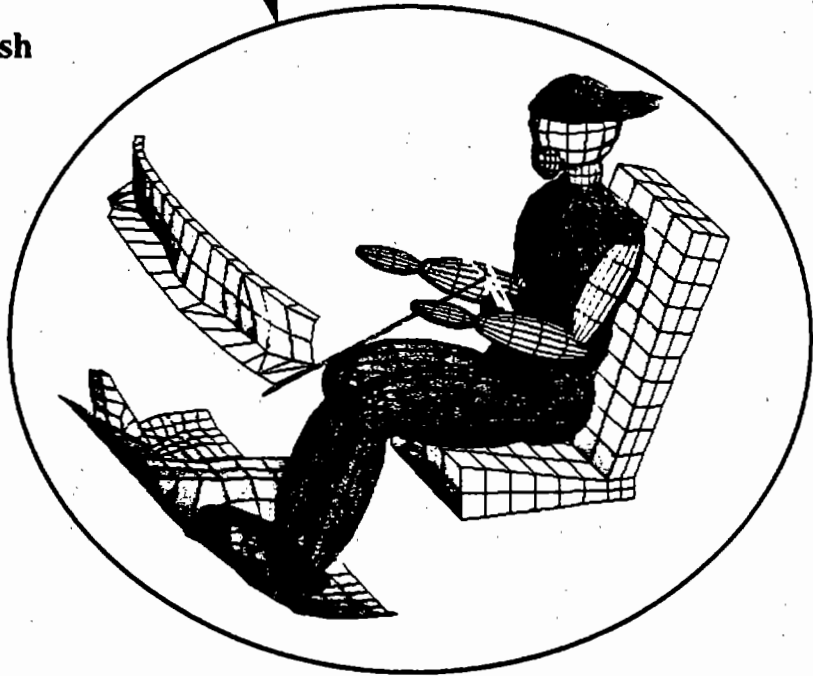
In the current coupling strategy, MADYMO-generated body displacements and angular orientations at  $t_n$  are transmitted to DYNA3D, which then updates the position of its rigid bodies to  $t_{n+1}$ . These updated positions are then checked for any contact forces that may have occurred because of the interaction of the rigid ellipsoids with the vehicle interior. The computed contact forces are then passed back to MADYMO as forces and moments at each body cg. A direct coupling scheme was employed in the coupling, i.e., a common time step ( $\Delta t$ ) was chosen by DYNA3D. The DYNA3D/MADYMO coupling scheme has been fully described in chapter 2, section 1.

A DYNA3D/MADYMO mesh, which included the Taurus frontal impact mesh and a Hybrid III occupant, was constructed. This simulation was intended as a demonstration of the feasibility of performing a complicated coupled calculation. The DYNA3D and MADYMO meshes can be seen in figure 19. Unfortunately, this problem could not be run to completion. The Taurus/Hybrid III simulation problems that prevented completion of the simulation were:

- The only 5.0 version of MADYMO available was an older release that did not have restart capability and was compiled under an older SGI operating system, 4.0.1.
- This restricted MADYMO to running on an older SGI workstation because of operating system upgrades on other new and faster LLNL workstations.
- This older SGI workstation, with DYNA3D and MADYMO installed, would have taken 100 days to run the coupled DYNA3D/MADYMO problem.
- A reduced run time (30 days) resulting from a PVM linkage between two workstations was possible by running DYNA3D on a faster workstation and MADYMO on the older workstation.
- However, because of network problems, the network wasn't capable of a continuous 30-day run.



**Complete FEA Mesh**



**Hybrid III Crash Dummy**

Figure 19. Taurus mesh with a Hybrid III occupant.

Impending upgrades to the coupling capability of MADYMO and DYNA3D should alleviate the problems that were encountered above in trying to run a complicated coupled problem. These upgrades include restart capability; variable starting time for each code; and the linkage of MADYMO planes, ellipsoids, and bodies with DYNA3D rigid bodies.

#### **Section 4. Side impact Taurus model from NHTSA**

LLNL obtained a PATRAN generated LS-DYNA side impact model of a Ford Taurus combined with an MDB model. In this mesh, the MDB was located at a right angle and initially moving toward the drivers door. The mesh was generated by an outside contractor who qualified the mesh with LS-DYNA runs. This mesh was converted to a DYNA3D compatible input form and run through the DYNA3D initialization phase, during which many (2,584) nodal penetrations were observed, and the problem terminated. A DYNA3D compatible input file of the original mesh geometry is available upon request.

#### **Section 5. Debug side impact Taurus model received from NHTSA**

The Taurus side impact mesh, which was described in section 4, was further inspected in an effort to reduce the number of initial nodal penetrations that were detected by DYNA3D in the initialization phase. As a result of this effort, the number of detected penetrations was reduced from 2,584 to 933 and a revised DYNA3D side-impact input file was generated. During subsequent DYNA3D runs, it was determined that the 933 penetrating nodes would still not allow the problem to run to completion unless the nodes were removed from the automatic contact description. This revised DYNA3D input file is available upon request.

#### **Section 6. MDB model for side impact**

A NHTSA-supplied MDB FE model was reviewed and modified to provide improved agreement with test data. This MDB barrier was developed and validated for NHTSA several years ago by the Volpe National Transportation Systems Center. Both the model of the MDB and material model input were modified. The validation consisted of comparisons between calculations and test data for full frontal and 60-degree impacts into rigid barriers. The test data consisted of impact force time histories from transducers that were located on the rigid barriers. Recent computer simulations using the same mesh and a later version of the original FE crash simulation code produced responses of the MDB which were stiffer than the original calculations. Initial DYNA3D calculations with the MDB mesh also produced results that were much stiffer than the test data. NHTSA asked LLNL to help resolve the inconsistencies between the DYNA3D calculations and the test data.

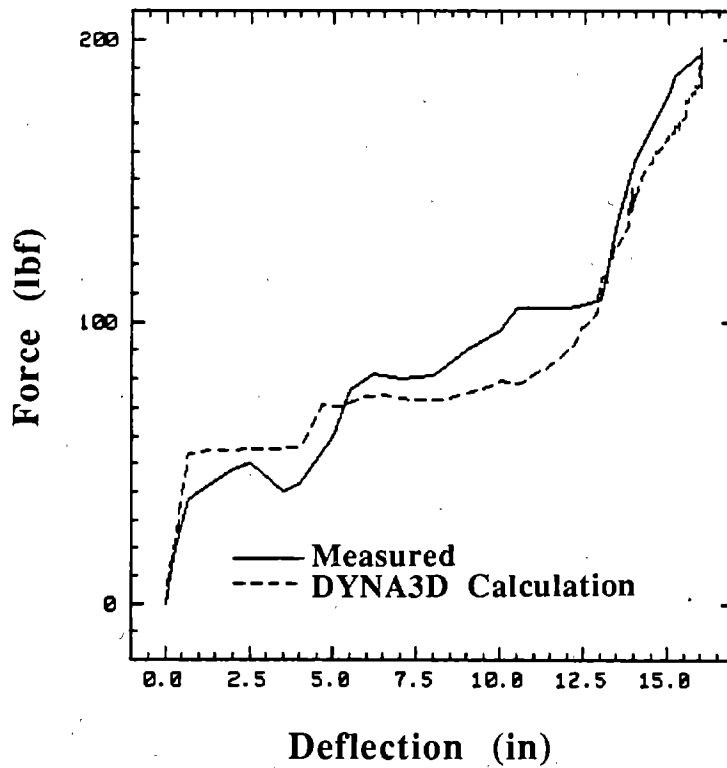
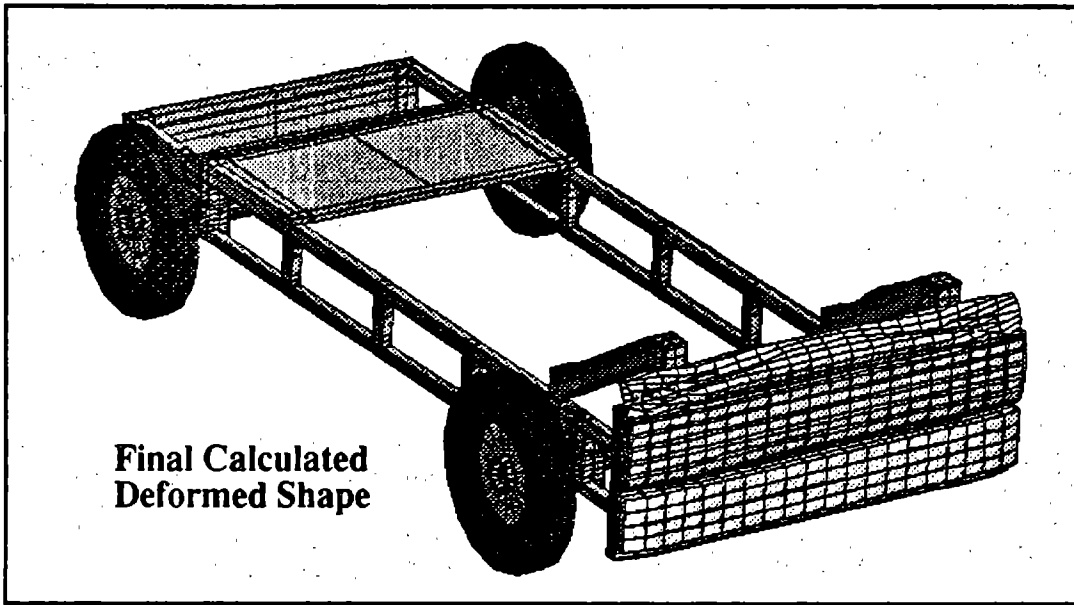
Changes that were made to the MDB mesh included reducing the number of tied contact surfaces and rezoning the honeycomb bumper material to provide more zones in the lateral direction. Contact between the MDB and the barrier was simulated with a DYNA3D *rigid wall*, a kinematic constraint on any MDB nodes which attempt to penetrate the wall surface. MDB impact forces were obtained from the calculated MDB decelerations. Changes were also made to the DYNA3D material Model 26 (Metallic Honeycomb) input to describe a more compliant elastic modulus for the honeycomb in

the fully compacted state, and smoother, stiffer stress limit curves for the honeycomb material in the near fully compacted state.

The changes described above resulted in favorable comparisons of computed and measured force versus deflection results for the MDB in 59 km/h (37 mi/h) full frontal and 60-degree impact tests, as shown in figures 20 and 21. Maximum aluminum honeycomb strain rates of 15.2 m/m/s (600 in/in/s) in the axial (crushing) direction were computed, with no observed yielding, for both of the runs. Based on these results, further material testing of the honeycomb in the partially and fully compacted states at representative strain rates was recommended to validate the changes that were made to the DYNA3D honeycomb material representation.

### **Section 7. MDB side impact simulation**

LLNL has run the intermediate side impact model/MDB mesh without the dummy or detailed interior (see section 5). No coupled computations were possible because LLNL did not obtain the detailed model with the dummy inside. Also note that the recent upgrading by TNO of the MADYMO/DYNA3D link will require additional DYNA3D development efforts before the current TNO coupling format can be used.



**Comparison With Data**

Figure 20. Full frontal 59 km/h (37 mi/h) MDB impact results.

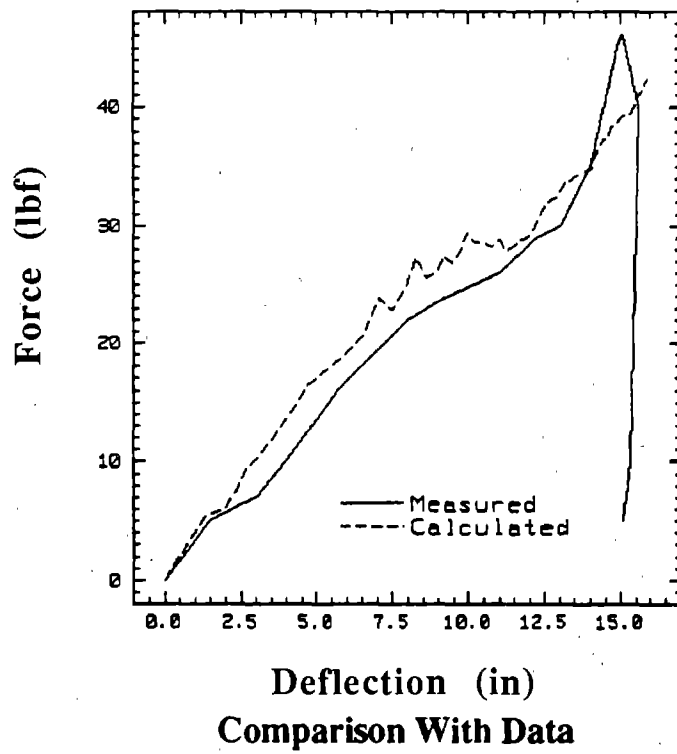
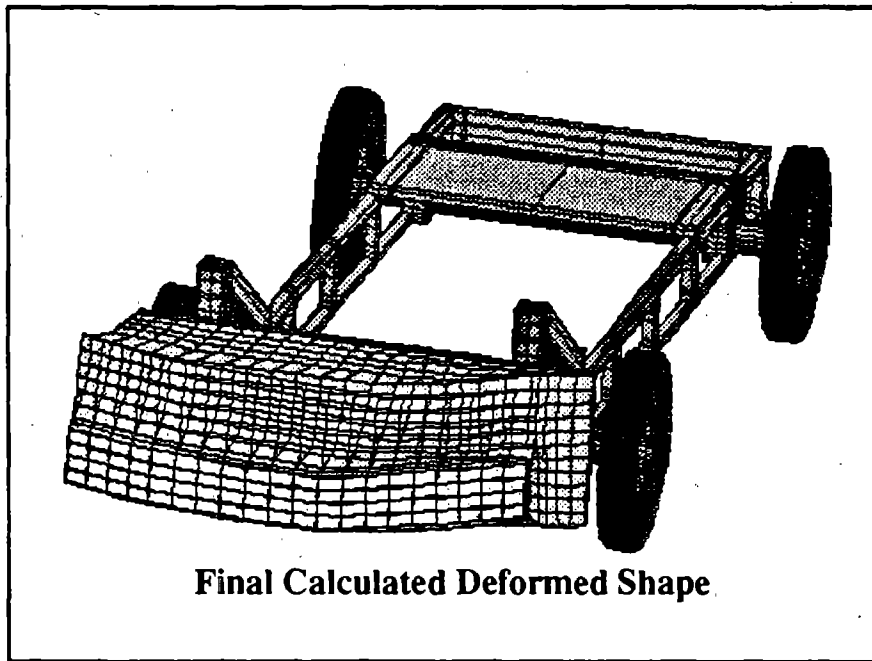


Figure 21. 60 degree 59 km/h (37 mi/h) MDB impact results.

## CHAPTER 4: PASSENGER COMPARTMENT MATERIAL MODELS

### Section 1. Crushable foam

A viscoplastic, orthotropic constitutive model was developed for rigid low density foams. The model has been implemented into a checkout version of DYNA3D for evaluation before final insertion into DYNA.<sup>(32)</sup> This model has application for use in vehicle interior components and crash dummy computer models that simulate interaction between the vehicle and the occupant during a crash. The multisurface yield criterion used in the constitutive model is a modified version of the envelope-of-failure surfaces for cellular materials. The flow direction was chosen to simulate the near-zero 'plastic Poisson's ratio' observed in many experimental tests. Effective stress principles and a phenomenological, nonlinear, hypo-elasticity law were used to capture effects caused by densification in the large strain regime, including the orientation dependence of the rate of densification seen in uniaxial compression tests of orthotropic foams. The rate dependence is modeled by a power law viscoplasticity relation. Experimental results from several loading conditions are shown to be effectively simulated by this model.

This material model was developed and implemented in DYNA3D to simulate the behavior of the rigid, low-density foams used as automotive interior component crash padding for NHTSA to enhance current vehicle-crash-simulation technology. These foams have other uses, such as, protective packaging and impact limiters for nuclear waste containers, because of their energy absorbing capabilities. The main characteristic of such foams is their ability to maintain a near-constant stress (plateau) during compression for strains up to 80 percent as shown in figure 22, after which densification becomes apparent. The foams are typically made from rigid polyurethane, polystyrene, or polymethylmethacrylate and, consequently, exhibit large permanent strains (crush) and are viscoplastic in nature. They range in relative density from 0.03 to 0.3 and have open or closed cellular structure. Because of preferential cell growth in the rise direction during processing, the foam properties are often acutely anisotropic.

To accurately capture the response of this material, the following characteristics were considered: orthotropy, complex yield surface, non-associative flow, viscoplasticity, and densification. To reproduce experimental data, the development of this model combines some of the current microstructural theory of foam with phenomenological methods.

The behavior of rigid, low-density foams in compression can be divided into three regions (figure 22): elastic, stress plateau, and densification. The elastic deformation is caused by bending and stretching of cell walls and struts. The stress plateau is caused by a complicated interaction of plastic hinges and buckling of the cell walls and struts. In the densification region, volumetric compression causes cell walls to contact and a rapid increase in stress. In tension, the foam behaves elastically until it ruptures. Gibson *et al* derived the failure surfaces for foam under multiaxial loads, using microstructural analysis.<sup>(33)</sup> It is the envelope of these failure surfaces that is used for the model presented here. The first failure surface is provided by the plastic hinge growth caused by the bending moments and axial stresses in the cell walls and struts. It has been shown to be applicable to closed cell foams, because the surface tension during forming causes cell walls to be thickest at cell wall junctions, such that closed cell foams can be treated as a system of struts.<sup>(34)</sup> Another failure surface is caused by buckling of the cells. Gibson *et al* do not provide a general relation for this failure mode, but derive a specific form for

triaxial loading (see figure 23). A phenomenological cap surface defined for general loading conditions, and which matches well with the theoretical triaxial buckling surface, is used in our model. The hydrostatic, compressive yield stress is used for the case of isotropic foams. The cap surface is only considered when the hydrostatic stress is negative. Although the buckling is elastic, it precipitates plastic hinge growth and hence plastic strain. Tensile failure is shown to be governed by a principal stress-failure criterion (shown as  $f_3$  in figure 23).<sup>(33)</sup>

When the material reaches its tensile limit, the deviatoric stresses diminish. When the material fails because of buckling or plastic hinges, yielding occurs. Experimental investigations have concluded that these foams experience little to no transverse strain during uniaxial compressive yield.<sup>(34,35,36)</sup> LLNL reproduced this response for rate-independent applications using a flow law that relates the plastic portion of the rate of deformation gradient to the Cauchy stress. This phenomenon is particularly important when reproducing results from Brinell hardness tests.<sup>(35,36)</sup>

The rigid matrix materials, polyurethane, polystyrene, and polymethylmethacrylate, are often viscoplastic; consequently, foams made of these materials can be viscoplastic. A power law version of the Duvaut-Lions viscoplasticity theory was used, since it is amenable to multi-surface yield conditions.<sup>(37)</sup> This projects the Cauchy stress onto the elastic domain. Examination of figure 24 clearly demonstrates the necessity of the power law formulation.

The hardening exhibited at large volumetric compression is caused by the increased contact of cell wall surfaces and struts as the free volume diminishes. Although closed-cell foams have entrapped air that causes increased hydrostatic compression, it is seen for the class of rigid foams that cell walls rupture when buckling occurs, and the air escapes.<sup>(34)</sup> It is assumed that the total stress exerted by the foam after yielding is caused by contributions of the elastic axial and bending stresses in the cellular matrix and contact of adjacent cell walls and struts as they sandwich together. The effective stress is a summation of the stress caused by bending, strut axial stress, and stress densification. The stress is constrained by the failure surfaces described above. The bending stress is constrained by the yield surfaces and is used to determine the plastic strain. The evolution of the bending stress is governed by a relationship between the orthotropic elastic stiffness tensor, which represents the bending and axial deformation of the struts, the volumetric strain (determinant of the deformation gradient), and the elastic portion of the rate of deformation gradient. The evolution of the deformation gradient is governed by a relation between the elastic stiffness tensor for the bulk matrix material (usually isotropic) and an intrinsically defined function of the volumetric strain, the densification strain, and the rate of densification vector. The densification strain represents the strain at which the foam becomes as stiff as the bulk material. The densification vector represents the apparent orthotropic rate of densification seen in uniaxial compression tests.<sup>(34,38)</sup> For example, uniaxial compression tests done on two orientations ( $0^\circ$  and  $90^\circ$  with respect to rise direction) of the same orthotropic foam are shown in figure 25.



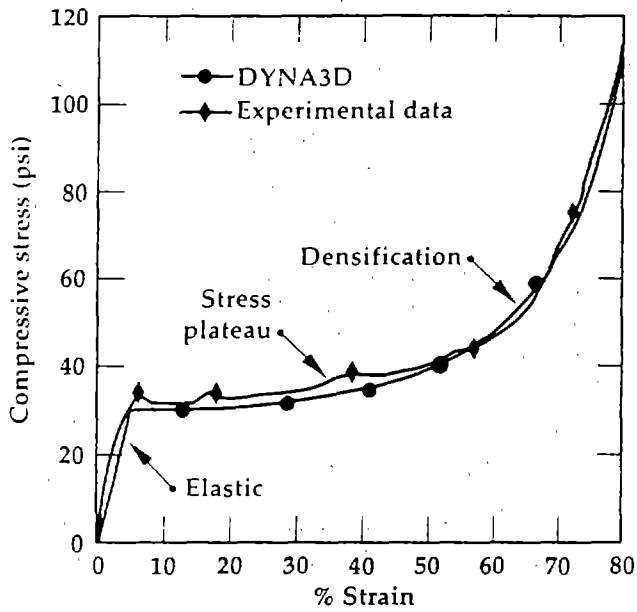


Figure 22. Three regions of stress seen in experimental data from a uniaxial compression test along with DYN3D simulation.

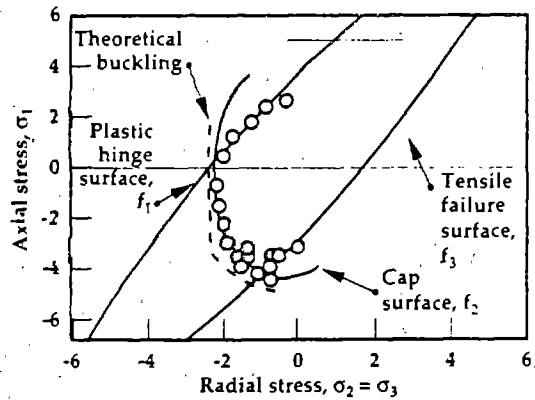


Figure 23. Experimental data for compressive radial stress at failure in triaxial tests, along with the envelope of failure surfaces  $f_1$ ,  $f_2$ ,  $f_3$ .

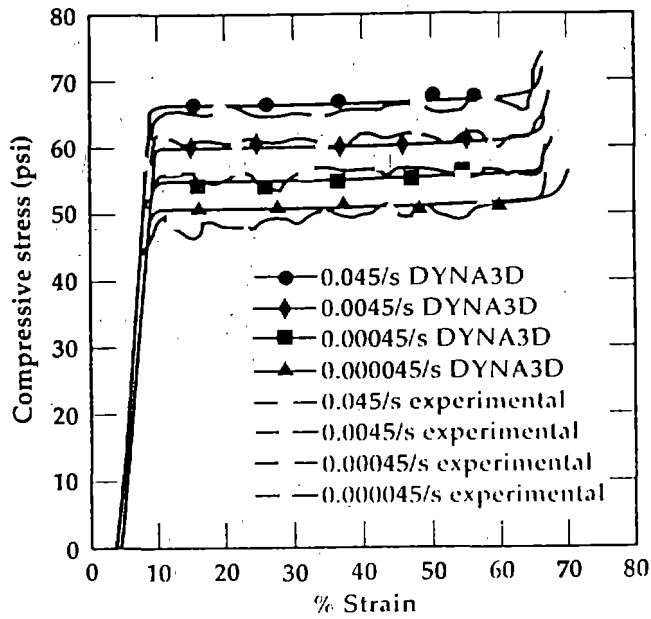


Figure 24. Experimental data and DYNA3D simulation of uniaxial compression tests done at four different strain rates.

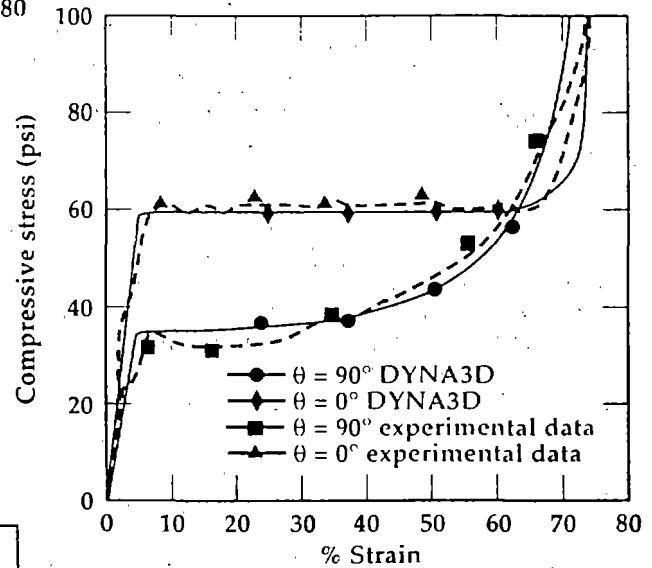


Figure 25. Experimental data and DYNA3D simulation of uniaxial compression tests done on two orientations of the same orthotropic foam (0° and 90° with respect to rise direction).

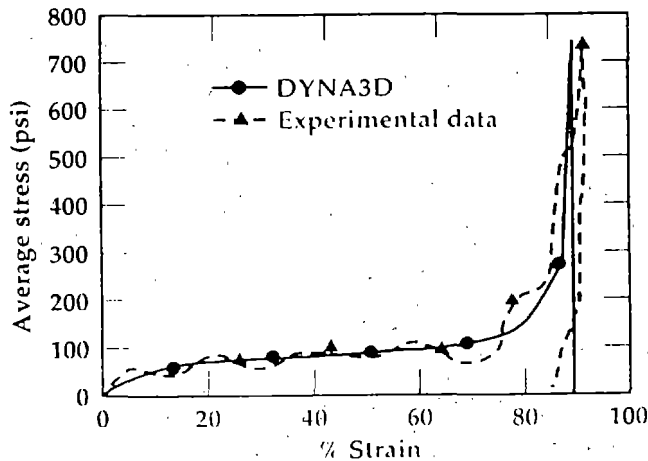


Figure 26. Experimental results and DYNA3D simulation of a drop test in which a 18.2 kg (40 lb) aluminum block traveling at 32.5 km/h (20.3 mi/h) impacts a 0.06-m (2.5-in) thick section of foam.

This material model will typically be applied to crash simulations where high-speed impact results. Figure 26 shows experimental results from a drop test, for the case of a 18.2 kg (40 lb) aluminum block traveling at 32.5 km/h (20.3 mi/h) impacting a 0.06-m (2.5-in) thick section of foam.<sup>(38,39)</sup> The DYNA3D implementation of the proposed model provides a good fit to the experimental data.

Completion of the orthotropic and tension failure implementations of the model in DYNA3D is necessary. As mentioned, this model is applicable to the rigid class of low density foams. The class of flexible polyurethane, polyethylene, and polypropylene type foams remain to be modeled. Unlike the rigid foams, these foams exhibit little to no permanent crush and tend to be viscoelastic in nature.

## **Section 2. Safety glass**

A research effort on advanced material models was internally funded at LLNL with the goal to provide applications of advanced material models in DYNA3D and its sister code ALE3D.<sup>(40)</sup> One programmatic application focused on methodology for earth-penetrating weapon analysis in the traditional weapons mission of LLNL, with benefit also to the commercial world, in the form of improved crack propagation for impact of laminated safety glass.

This work has its origins in the continuing studies of both the defense and commercial applications of LLNL's FE code suite. LLNL has had a tradition of developing methodologies for Earth Penetrator Weapon (EPW) analyses, and this has resulted in the development of well-known techniques for penetration, using Lagrangian codes such as DYNA3D. The potential of the oriented crack model for ALE3D led to a study of this model as applied to laminated safety glass (windshield) impacts. This allowed another technology gap to be filled that had been identified during the TAHRs thrust area activity of FY92 to FY93.<sup>(22,41)</sup>

### **Ball Impact on Laminated Safety Glass**

LLNL investigated the potential of ALE3D to solve the problem of a rubber-cushioned metal ball impacting a windshield. This investigation included the effects of two tensile failure models, the zoning of the glass plate, and the boundary conditions on the plate. The test of goodness is a match to the experimentally observed deceleration of the ball as measured by an on-board accelerometer. One of our models for glass failure showed some of the radial cracking that is observed experimentally. The ball hitting the glass is intended to simulate a person's head impacting a windshield.

The experiment that was calculated is now described. A ball of 16.5 cm (6.5 in) diameter and 10-kg mass impacts a rectangular section of horizontally mounted windshield pane normally at 9.76 m/s. The glass pane measures 0.61 m by 0.91 m (2 ft by 3 ft) and is struck in the middle by the ball. In the experiment, the ball carries an on-board accelerometer whose record one tries to calculate. In the calculation, the ball's upper hemisphere consists entirely of aluminum, while the ball's lower hemisphere consists of a rubber cap of 9.5 mm thickness, with the remaining hemisphere consisting entirely of steel. Any structure internal to the ball is ignored. The glass plate consists of two layers

of glass of 2.29 mm thickness each, that form a bonded sandwich with a layer of plastic of 0.76 mm thickness.

The problem was calculated as a quarter problem on the ALE3D code, using two different kinds of zoning. The cuts were made along the two symmetry planes of the vertical impact problem. The first zoning was similar to Browne and Khalil: square in the plate under the ball and then roughly radial to the edges of the plate, with each layer of pane being one zone thick (see figure 27). The second type of zoning was square all the way to the edge of the plate. The zoning in the ball was assumed to be inconsequential except to resolve the curvature of the ball.

The choice of boundary condition on the edges of the pane was found to be important because of the long time that passed before cracks formed. Clamping the edges of the plate appears to reinforce the plate. The effect is to disallow tensile stresses near the plate's edges. The runs were, therefore, made by confining the plate's movement perpendicular to its plane, but allowing motion parallel to the original orientation of this plane. This is intended to simulate a vertical clamping that allows horizontal slippage.

In addition to the boundary conditions on the plate, the parameters whose importance was investigated include the zoning of the plate, and the material model for the glass. A simple model was used that causes the zone to fail isotropically as soon as any principal stress exceeds the tensile strength of the glass. The simplicity of this model (a model that is apparently very similar to previous work made it suitable for investigating the effects of zoning and boundary conditions.<sup>(42)</sup> A second material model considered is centered around a failure algorithm that generates cracks in discrete directions. When cracks are formed, voids are permitted to open, and the stresses internal to a zone are redistributed accordingly. After a crack forms in a zone, the zone in question can still support tensile stresses in directions parallel to the crack plane. This constitutes a tensorial, anisotropic cracking model. The model is also coupled to a simple, shear failure model, which does not come into play in this problem. The material constants used are those given in Browne and Khalil.<sup>(43)</sup> Unlike that work, identical material constants were used for all portions of the glass.

These calculations were evaluated by measuring the velocity and acceleration of the aluminum and steel portions of the ball. The two materials tracked each other very closely. The cracking in the plates was observed by using contour plots of maximum principal stresses and fractional void volumes (void strains). Results obtained with the simple material model described above match experimental acceleration levels fairly well.<sup>(43)</sup> The accelerations tend to be around 30 g's. However, this problem requires substantially finer zoning than that used initially. Refining the radial zoning pattern in the quarter plate from the initial 384 zones to 2,40 zones (shown in figure 27) and to 5,664 zones, strongly affects the acceleration-time history of the ball. The reason for this zoning dependence appears to be the need to resolve the curvature in the glass near the ball, and where and when cracks are initialized.

The detailed structure of the acceleration-time history of the latter two problems is sufficiently different to make a direct comparison difficult. Figure 28 shows the velocity-time histories, which are easier to compare. These two runs are represented by curves A and B, respectively, and are seen to track each other fairly well until about 2 ms, when they

diverge. The agreement up to this point suggests that the plate region in the area of ball contact (the footprint) is resolved sufficiently well with either zoning to give consistent results. The run that gave curve C uses square zoning everywhere in the plate, which, however, is also coarser than the radial zoning in the footprint region. A very different crack pattern from that of the other two runs was noted.

In general, the cracking seen in the upper layer of glass (side closest to the ball) cracked differently than the lower layer. Typically, the upper layer right under the ball was heavily cracked; i.e., most zones were cracked, while the lower layer showed some tendency to crack along the symmetry planes as well. The cracks seem to be formed not so much by any sharp signals that are generated by the ball's impact, but rather by the general flexure that is induced in the plate. In this model, details of the crack pattern are difficult to evaluate, but differences in the timing of their appearance and in the extent of the cracked region seem to contribute to differences in the ball's velocity-time history.

As expected, changing the tensile strength of the glass for a given zoning has a profound effect on the acceleration history of the ball. This effect is shown in figure 29, which compares the velocity-time history of two identical problems that differ only in the tensile strength. The higher tensile strength gives the sharper decelerations. Comparison with figure 28 suggests that lower tensile strength has an effect similar to that of coarser zoning, in that the velocity-time histories become more linear with a reduced average slope (reduced average deceleration).

Care had to be taken in each run to assure that void closure between the ball and the plate proceeded properly. The void closure was sensitive to the zoning mismatch between the plate and the ball, as well as to the time step during the closure process. Improper void closure sometimes manifested itself in premature damage in the plate, which had a strong effect on the subsequent deceleration of the ball. Several runs were made with the tensorial failure model that was described above and that has been recently installed in the ALE3D code. This model is still under development, but in the limited time that it was able to run before giving nonsense answers or crashing outright, it produced some amount of radial cracking that was not seen with the simpler material model.

The first type of zoning used for this sequence of calculations was the same as that in figure 27, which also shows the cracking obtained with this model. The problem ran to nearly 2 ms and developed cracking in the entire region of the ball's footprint. In addition, the upper layer had a small radial crack along the long symmetry line of the plate. The lower glass plate, in addition to the cracking in the central region, displayed long cracks along both symmetry lines. This type of cracking was also observed with the simpler model. A fairly long radial crack is visible on the 45° line. An additional, very short radial crack is noticeable nearby. These radial cracks were not seen in any of the runs with the simpler model, despite the fact that they ran to 20 ms as compared to just 2 ms. It is, however, exactly this type of cracking that is most prominent in the experiment. Unfortunately, time histories for this run were lost, due to general systems problems.

As a test of a possible zoning dependence of the crack direction using the tensorial crack-ing model, a problem was run that used square zoning in the plate, as discussed above. This problem also showed the heavy cracking in the ball's footprint in the top plate with only a very small amount of radial cracking. The bottom plate showed long radial cracks

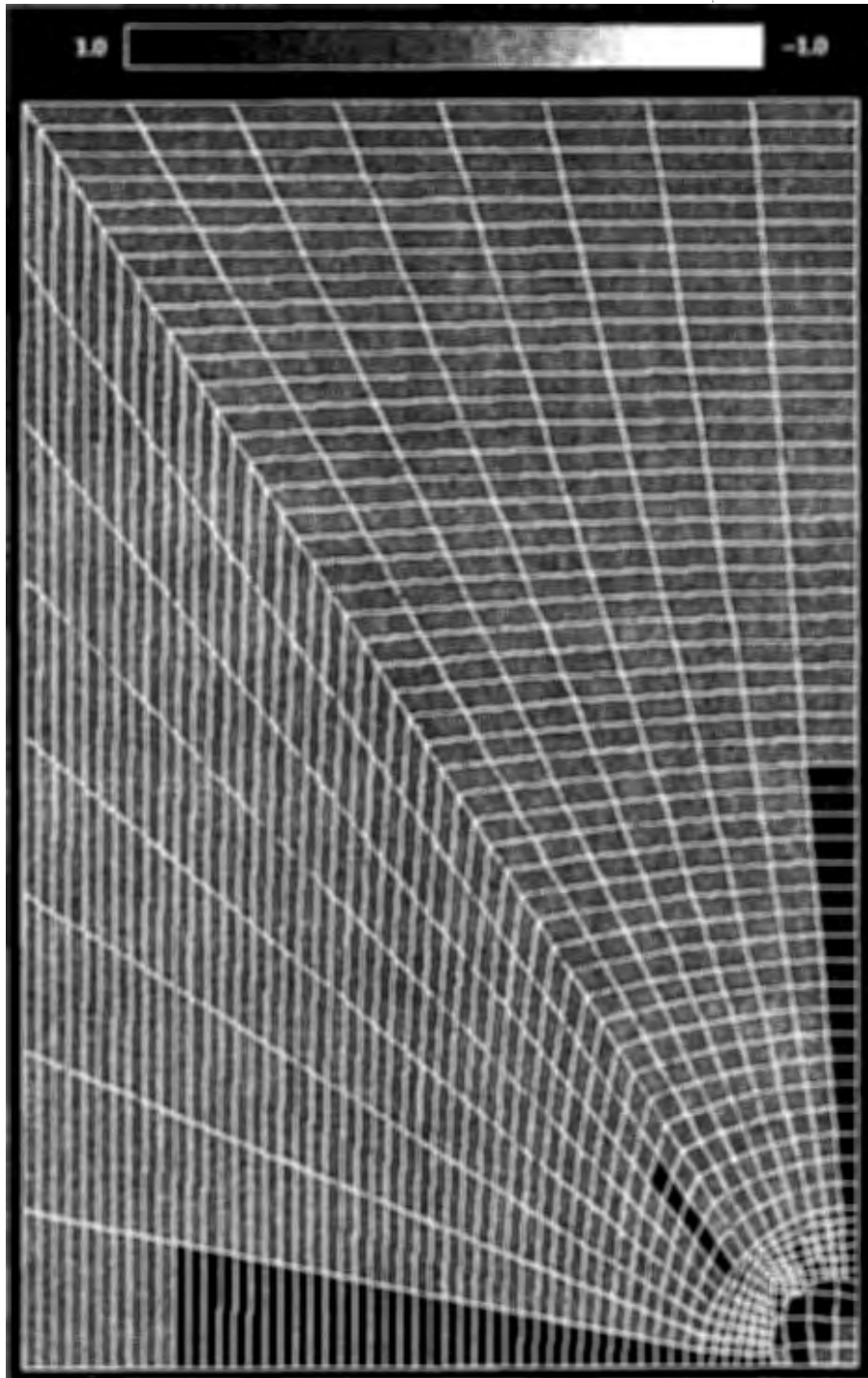


Figure 27. Plan view of the underside of the quarter pane, showing the mesh and the cracked zones.

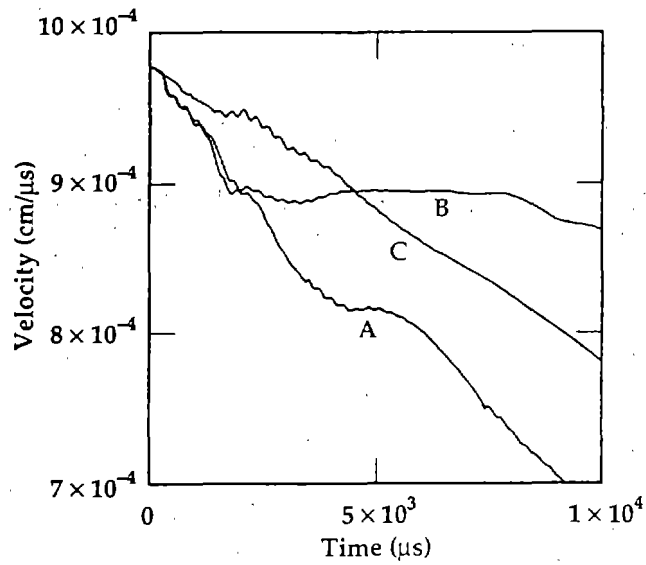


Figure 28. Velocity vs. time of the steel ball for three problems. (In all three cases, a simple model with a tensile strength of 0.6 kb was used for the glass, but the zoning is different. Curve A has zoning shown in figure 27. Curve B has double the angular zoning; curve C uses 0.1-m square zones.)

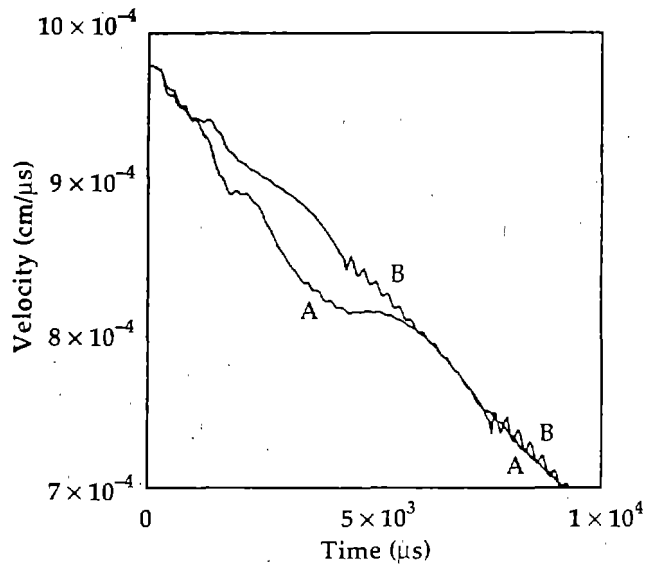


Figure 29. Velocity vs. time of the steel portion of the ball for two problems. (Both problems use the simple material model and the zoning shown in figure 27. The tensile strength is 0.6 kb for curve A and 0.1 kb for curve B.)

but, unfortunately, an additional pattern of heavy cracks developed here that is non-physical and points to additional shortcomings in the material model at its current state of development. Such unphysical cracking was not observed using the simpler crack model with identical zoning. Considering the strong dependence of the acceleration-time histories on the damage that occurs in the plate, one must assume that the details of the plate delamination are also of great importance. While ALE3D has a model to represent such a phenomenon, one reserves pursuit of this question until a tensorial damage model is fully functional.



## CHAPTER 5: VEHICLE AND BARRIER CRASH SIMULATIONS

Traditionally, roadside safety devices are designed and evaluated mainly by extensive testing. With high performance computer workstations becoming more affordable and FE codes becoming more sophisticated in the areas of impact dynamics and material modeling, the use of computer simulation to design roadside safety devices is becoming an attractive alternative to testing. To explore this alternative, the FHWA has initiated a program to develop an FE model for a small-size car that can be used to perform vehicle/barrier impact simulations. The computer code of choice is DYNA3D, a nonlinear explicit FE code developed at LLNL. A detailed DYNA3D model of a 1982 Honda Civic hatchback was used to represent a typical small-size vehicle. Using digitized data obtained by scanning all the parts in the Honda Civic, a DYNA3D model was generated using LLNL's mesh generator INGRID.<sup>(30)</sup> FHWA has conducted four Honda frontal crash tests at its Federal Outdoor Impact Library (FOIL), located at the Turner-Fairbank Highway Research Center in McLean, Virginia. The purpose of these tests was to collect crush characteristic data that can be used to verify the results from the DYNA3D analysis. LLNL was commissioned to first debug, then fine tune a contractor-developed model, and finally develop a validated frontal impact Honda model using the FOIL test data as the benchmarks.

LLNL has debugged the full-size, contractor-developed model so that it is possible to simulate the frontal crash tests conducted at FOIL. However, a more numerically efficient and stable model was developed to perform the parametric analyses required to fine-tune the model. The comparison made between the DYNA3D results from the modified Honda model and the FOIL test data are presented. The comparison between the simulation and test data is quite good, but better correlation was obtained after additional model refinements. The correlation obtained is sufficient to qualify the modified Honda model as validated for the three pole tests described in section 1. Emphasis has been on retaining overnight timing on a workstation. Nonstructural members and nonessential contact were deleted, but were included for the model refinement described later in section 3. Also, LLNL identified two model regions that were further improved during model refinement. The present bumper bracket representation was modified to reflect the design existing in the test vehicles. The modeling of the cradle aft-engine mount which influences the correlation at the major center of gravity (c. g.) acceleration peaks was improved. Since the cradle aft-engine rubber mount was sheared off in the center bumper test, assumptions for the failure mechanism used in the model greatly effected the test data correlation. In section 2, the validated modified Honda was impacted against the u-sign post model obtained from FHWA. Good c.g. acceleration correlation was obtained at early time where the car/post impact is not influenced by the post/soil interaction. Later on, the post/soil interaction completely dominates, and the comparison is not as good. The correlation is dependent on consideration on how to properly compare measured and computed vehicle accelerations. This is highlighted in section 3 with a focus on the post and soil behavior. Therefore, LLNL considers the modified Honda model as validated for the u-post as well.

### Summary

DYNA3D analyses were performed to simulate four crash tests involving small-size vehicles impacting a rigid pole and a u-channel embedded in soil. The total force acting on the rigid pole and the acceleration at the vehicle c.g. were compared between the test data and the computer simulation. In general, the DYNA3D results show good correlation

with the test data up to 0.4 s after impact. Although the correlation is not as good between 0.4 and 0.75 s, the maximum load compares very well in the rigid pole impact tests. Discrepancies identified between the bumper support representation in the computer model and the test vehicles have created some uncertainties of the validity of the data correlation. Comparison between the data in the u-post impact test is reasonable. However, the vehicle response is highly dependent on the complex nature of the soil/u-post interaction and the use of a simple soil material model. Most of these analyses required about 3.5 CPU hours on a Cray YMP or 18 CPU hours on an IBM RS/6000 workstation. The Honda Civic model could be further improved by correcting the discrepancy in the bumper support and by fine-tuning the slidelines. The results obtained from this study demonstrate the feasibility of designing roadside safety devices using computer simulation.

### **Section 1. Frontal Honda model impact with rigid poles**

The global properties of the Honda Civic and geometries of the various car parts were based on a 1982 and a 1983 model Civic that the contractor purchased from private owners. The 1983 Civic was used to determine the global properties, such as total mass, moment of inertia, and c.g. of the vehicle. The 1982 Civic was disassembled to determine the surface geometries and thicknesses of the various parts. Using these data, a DYNA3D model was generated by INGRID. The Honda Civic model is shown in figure 30. A detailed description of the computer model has been documented.<sup>(44)</sup>

Only the front end of the Civic was meshed in detail. Discrete mass points were added to the model to accurately represent the total mass, the moment of inertia, and the c.g. of the vehicle. The original model has more than 13,000 nodes, about 100 beam and truss elements, 11,000 shells, and 260 solid elements. Beam elements were used to represent the suspension, drive shafts, and sway bar. Truss elements were used for the engine support mounts linked to the front cross member and the firewall. The rigid pole was modeled by solid elements. The remainder of the model was shell elements. Sliding contact surfaces (slidelines) were used to capture the impact interaction between the barrier and the vehicle.

Four frontal crash tests involving 1981 to 1983 Honda Civic two door sedans were conducted at FOIL. Three of the cars impacted an instrumented rigid pole and one impacted a single leg 6-kg/m (4-lb/ft) u-channel sign post embedded in strong soil. The nominal impact speed was 32 km/h (20 mi/h). The hoods of the car were removed before testing to film the engine compartment during the test. The weight of the test vehicles was 830 kg (1,830 lb). The test matrix is shown in table 1.

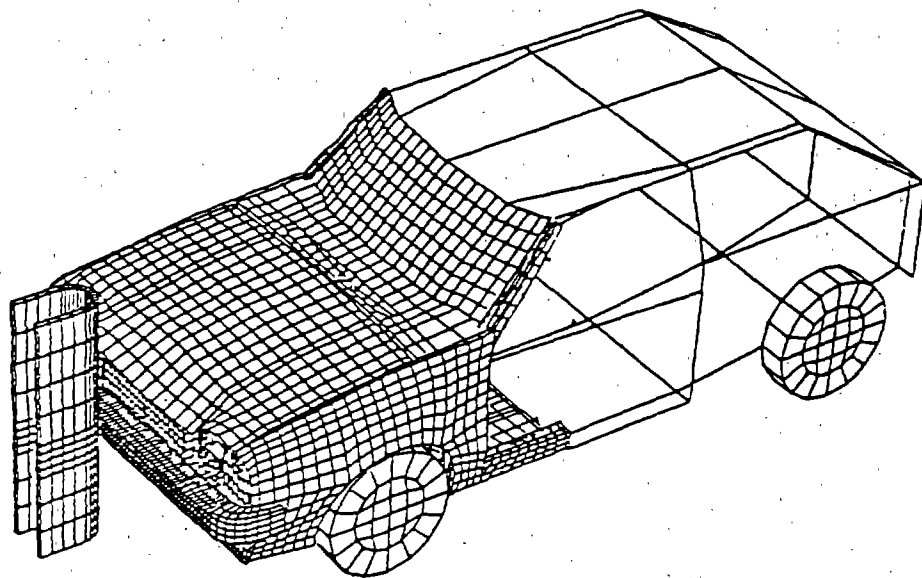


Figure 30. Original Honda Civic model.

Table 1. Test matrix.

Test Number	Test Article	Impact Location
93F008	Rigid Pole	Center of Bumper
93F009	Rigid Pole	457 mm left of Center Bumper (left bumper support)
93F010	6 kg/m U-Sign Post	228 mm left of Center Bumper (quarter point of bumper)
93F011	Rigid Pole	254 mm right of Center Bumper

A total of 16 channels of electronic data was collected during each test. Ten channels were collected by an on-board data acquisition system. They were mainly uniaxial accelerometers mounted at various parts of the vehicle, such as the top of the engine, control arms, and instrument panel. The data were pre-filtered with a 4,000 Hz analog filter and digitally sampled at 12,500 Hz. The remaining channels were uniaxial accelerometers mounted close to the c.g. of the vehicle to monitor the accelerations in the three local directions. Two load cells were also mounted on the rigid pole, one at each end of the pole. These data were collected by an off-board tape recorder system. The data were pre-filtered with a 500 Hz analog filter and digitally sampled at 2,000 Hz. After the FOIL test data were converted from the tape recording system into ASCII format, the data were again digitally filtered with a Butterworth low-pass filter of 100 Hz before they were put into final graphical form.

Description of the test setup and data plots for the FOIL crash tests are presented in the test report from FHWA.<sup>(45)</sup> The acceleration data and rigid pole load cell histories were compared with the simulation results from the DYNA3D analyses.

### Modified Honda Civic Model

Although the detailed model was debugged to make it possible to simulate some of the crash tests, the computation time was unacceptably long. The rigid pole impact with the model required about 9 CPU hours on a Cray YMP 8/128 for a simulation time of 0.1 s. In addition, the meshing techniques used made the model very susceptible to numerical instabilities that both extended the CPU time and made the results suspect. Some of the simulations became unstable and terminated prematurely. To benchmark the analysis results with the FOIL test data, the model needed to be fine-tuned using many parametric analyses. It became clear that the model would have to be made numerically stable and more CPU-efficient.

The original model contained many parts that did not merge together properly, parts that were severely distorted by poor zoning and improper merging, and shell elements whose edges were improperly used as impact surfaces. The model also included detailed representations of many nonstructural components such as the freon bottle, windshield, plastic fans, and plastic stone guard. The LLNL modified model was generated by eliminating a number of interpenetrating parts in the original model. Non-structural

members, such as the fenders, which were deemed to contribute little during the frontal impact were removed. The hood was eliminated as it was not present in the FOIL tests. To reduce the model size, certain parts, such as hinge pillar and its reinforcements, were combined as a single part with equivalent thicknesses. All impact surfaces were defined so that either shell faces were being impacted or discrete node-impacting-surface slidelines were used. The resulting modified model was about half the size of the original model. Although most element grids were in general coarser, the critical components at the impact locations were meshed with appropriate zoning.<sup>(46)</sup> With the modified model, a rigid pole impact simulation time of 0.1 s required about 3.5 CPU hours on a Cray YMP 8/128 or about 18 CPU hours on an IBM RS/6000 workstation.

In the three rigid-pole crash simulations, the pole was modeled as rigid material and was completely fixed at the back. The modified Civic model for the center bumper impact with the rigid pole is shown in figure 31.

### **Comparison of Test and Simulation Data**

Each of the three rigid pole crash tests was designed to provide a specific impact characteristic of the vehicle. The impact locations of the rigid pole impact tests encompass all the representative load paths on the front bumper. Although much data was collected during the test, the total force acting on the rigid pole and the acceleration histories near the vehicle c.g. were used as benchmark data to compare with the DYNA3D results. The total force acting on the rigid pole was derived by summing the forces from the two load cells mounted on the pole.

For the analysis, acceleration time history was gathered for a point on the floorpan close to the DYNA3D model c.g. Since this point on the floorpan is away from the frontal crash area and has no local deformation, its acceleration history approximates the rigid body acceleration of the whole vehicle. The total force impacted on the rigid pole by the vehicle was estimated from the product of the acceleration at this point on the floorpan and the car mass. The time history results were saved every 0.25 ms, and all analyses were calculated to 0.1 s.

**Center Bumper Rigid Pole Impact (93F008).** The center bumper impact test was performed to investigate the effects of the engine cradle on the vehicle response. The engine cradle is located on the center line of the vehicle and is a direct link between the cross member in the front and the floorpan in the back of the car. It also supports the engine/clutch/transmission assembly via a bracket at each end of the cradle. During the crash test, the rubber pad on the rear cradle engine mount was sheared off, transferring the impact load into the floorpan area. The aft-end of the engine cradle buckled severely and the floorpan near the firewall was badly distorted. The plot of the deformed car from the DYNA3D analysis at a simulation time of 0.1 s is shown in figure 32. Figure 33 shows the deformation in the engine compartment at 0.02 s and 0.08 s. From the time of initial impact to about 0.02 s, only the front bumper is crushing into the pole. After 0.02 s, the pole starts to impact the front cross member and the loads are transferred directly into the engine assembly via the engine supports. A force time history plot showing the comparison between the test and the DYNA3D result is shown in figure 34. As mentioned earlier, the test data were filtered with a 100 Hz low-pass filter, while the DYNA3D data were unfiltered. The correlation between the two is very good up to 0.04 s. The DYNA3D result drops off, then peaks at about 0.07 s, and finally decreases to

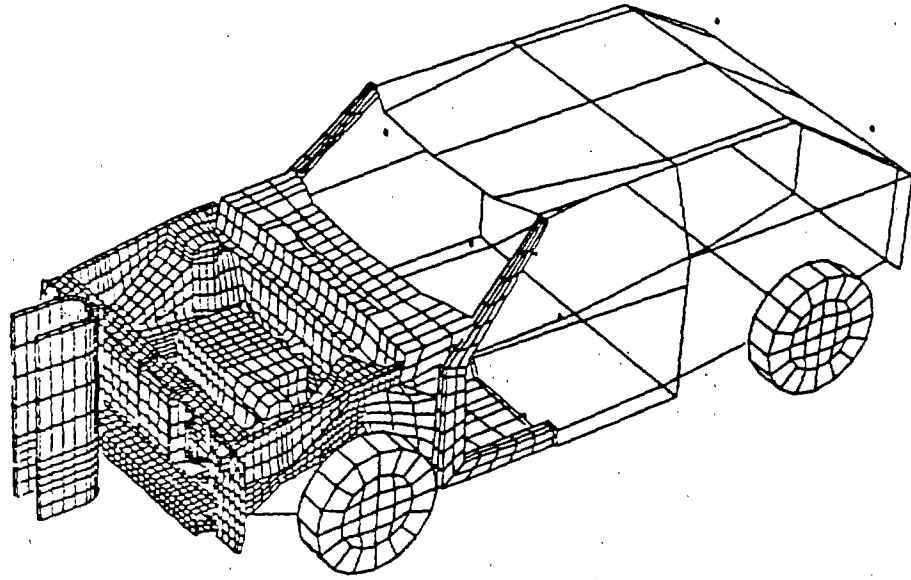


Figure 31. Modified center bumper rigid pole impact model.

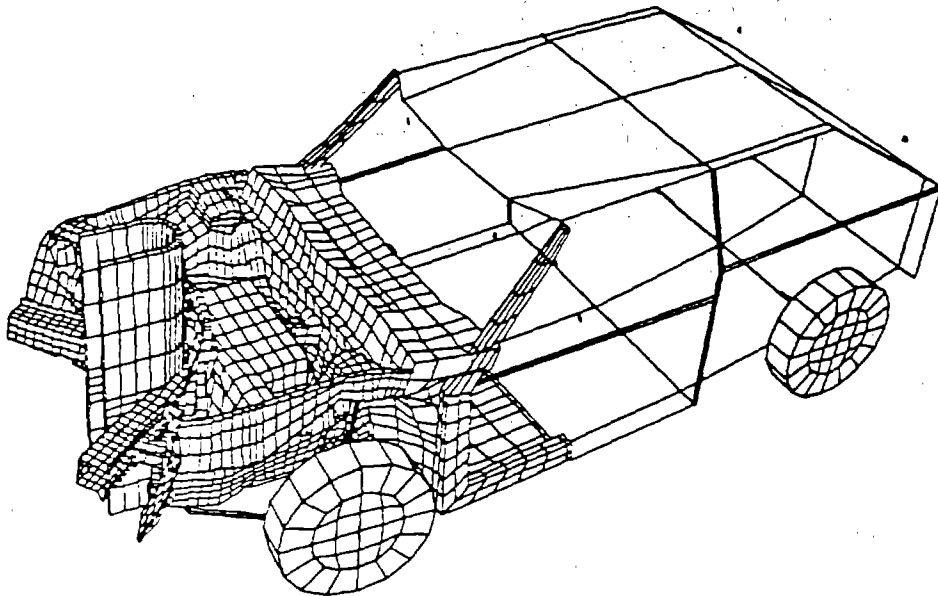
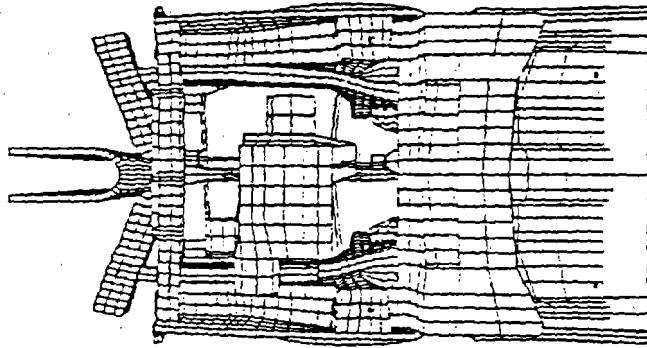
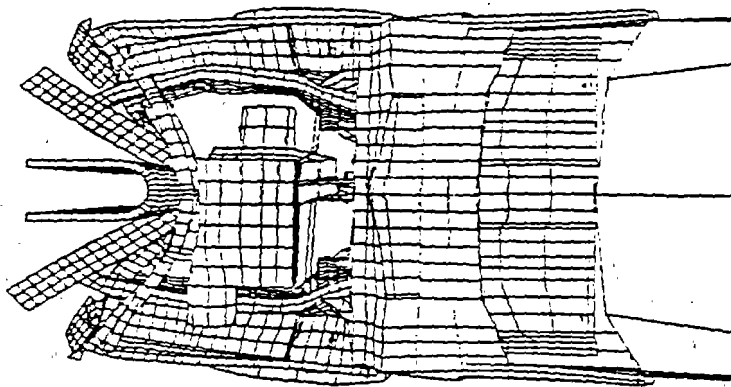


Figure 32. Center bumper impact model deformed shape at 0.1 s.



time = 0.02 sec



time = 0.08 sec

Figure 33. Center bumper impact model deformed shapes.

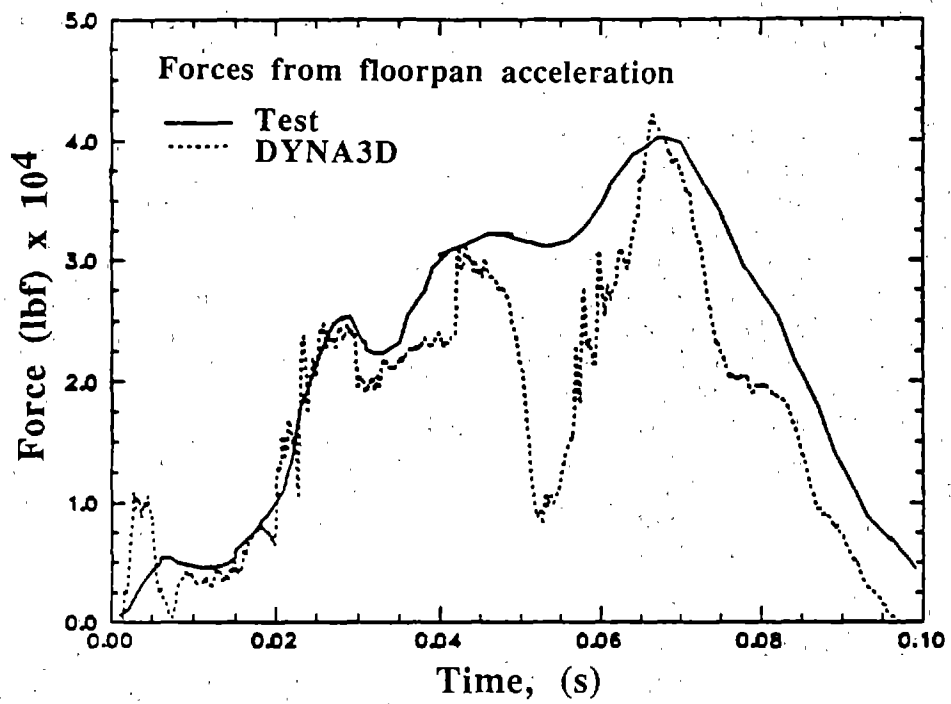


Figure 34. Comparison of test and DYNA3D results for center bumper impact.



zero at 0.1 s. The peak load correlates very well with the test data. Note that the computer model did not include any failure criteria at the cradle engine mount, and therefore the shearing failure at the engine mount that occurred during the test was not captured in the analysis. The response from a parametric analysis in which the rear engine mount was not connected to the engine differs drastically from the current analysis. To achieve good correlation with the test data, proper failure criteria must be included in the model.

**457 mm (18 in) Left-of-Center Bumper Rigid Pole Impact (93F009).** The impact point was 457 mm (18 in) left of the bumper center exactly where the left bumper support is located. The bumper support transfers loads from the bumper directly to the frame rail and the wheel house assembly. The undeformed DYNA3D model and the deformed shape at 0.08 s after the impact are shown in figures 35 and 36, respectively. A force time history plot comparing the test and simulation data is shown in figure 37. The DYNA3D result tracks the test data fairly well up to about 0.06 s but then decreases more rapidly than the measured acceleration. In general, the simulation result is below the test data curve. During the post-test inspection of the crashed vehicle, the bumper support was observed to be different from the one modeled in the computer model. The bumper support in the test vehicle is made up of a round strut while it is meshed as a rectangular tube-like member in the FE model. Since the bumper support is the key element of the left bumper crash test, this discrepancy implies that further refinements of the model are needed for a better correlation between the test and simulation results.

**254 mm (10 in) Right-of-Center Bumper Impact (93F011).** Figure 38 shows the initial condition of the 254-mm (10-in) right-of-center rigid pole impact model. The impact point in this case is half way between the engine cradle and the right bumper support. The load path is the least direct among the three rigid pole impact tests. The deformed shape at 0.1 s is shown in figure 39. The force time histories at the rigid pole collected from the test and from the analysis are compared in figure 40. The data correlate very well up to 0.025 s, but the DYNA3D result begins to deviate thereafter until it gets fairly close to the peak load at about 0.07 s. It was observed that the right wheel house and frame rail assembly in the test vehicle were not severely damaged from the impact. However, the frame rail and the wheel house assembly were buckled in the computer simulation as shown in figure 39. This disagreement can be due to the fact that the connection between the bumper support and the frame rail assembly in the model was over-constrained. With a strut-type bumper support properly included in the DYNA3D model, the correlation with the deformed shape would improve.

**U-Channel Sign Post Impact (93F010).** In the u-post crash simulation, the soil was explicitly modeled as strong soil, holding the u-post with sliding contact interfaces. This test was performed to evaluate the effects of a non-rigid barrier when the vehicle runs over the post after the initial impact. The modified Civic model for the u-channel sign post impact model is shown in figure 41.

The major difference between this impact test and the other three rigid pole tests is that the u-channel post is much more flexible and is embedded in soil. The impact point is between the engine cradle and the left bumper support. During the test, the u-channel post started to bend upon impact and was partially pulled out from the soil as the vehicle ran over it. The test vehicle eventually stopped further down the road. The bumper was only slightly damaged, as compared to those from the rigid pole impact. The soil holding the u-post was modeled with an elastic-plastic material model. Sliding contact surfaces were

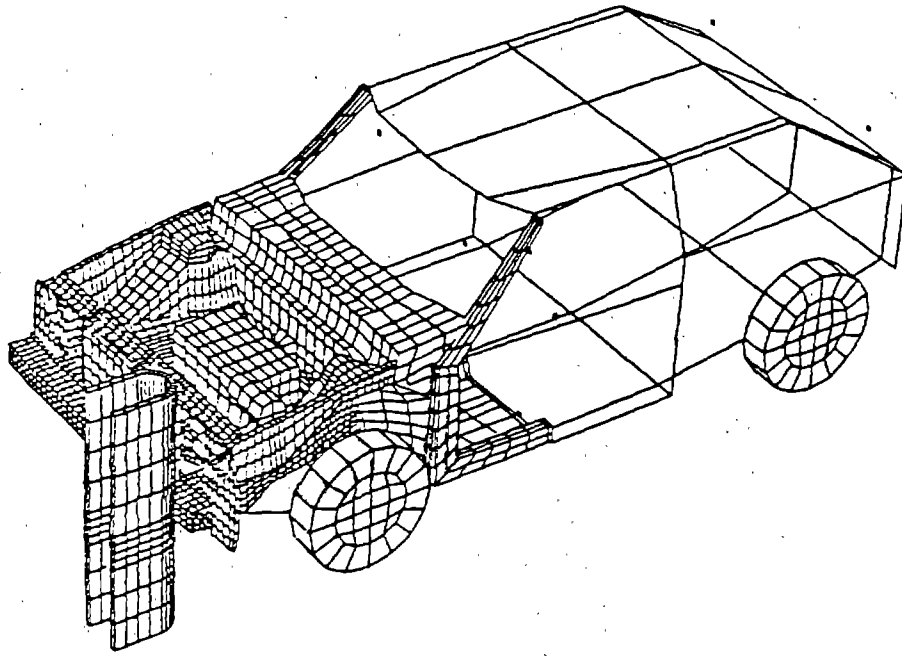


Figure 35. 457 mm left-of-center bumper impact model (bumper support).

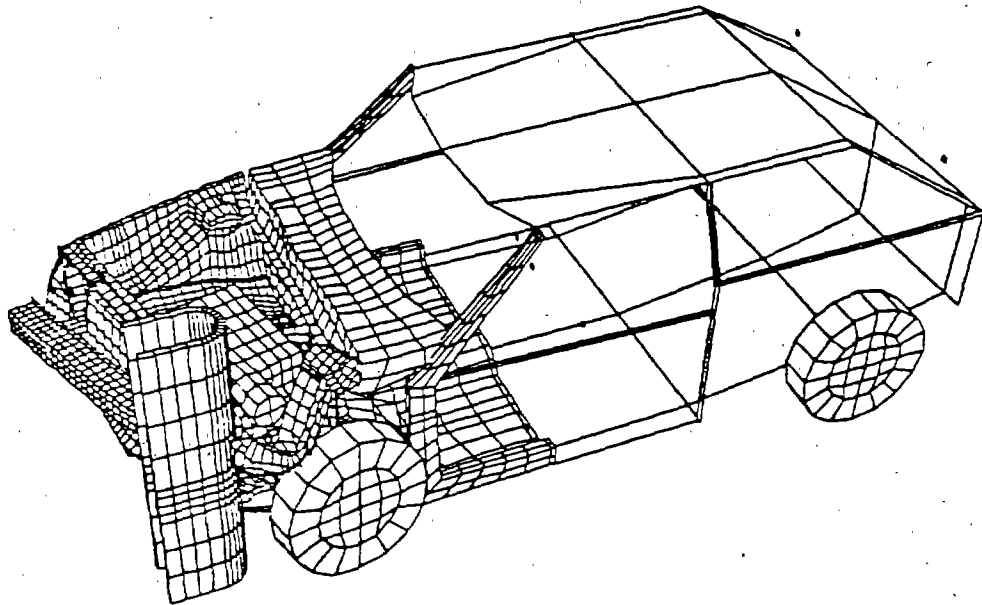


Figure 36. Deformed bumper support model at 0.08 s.

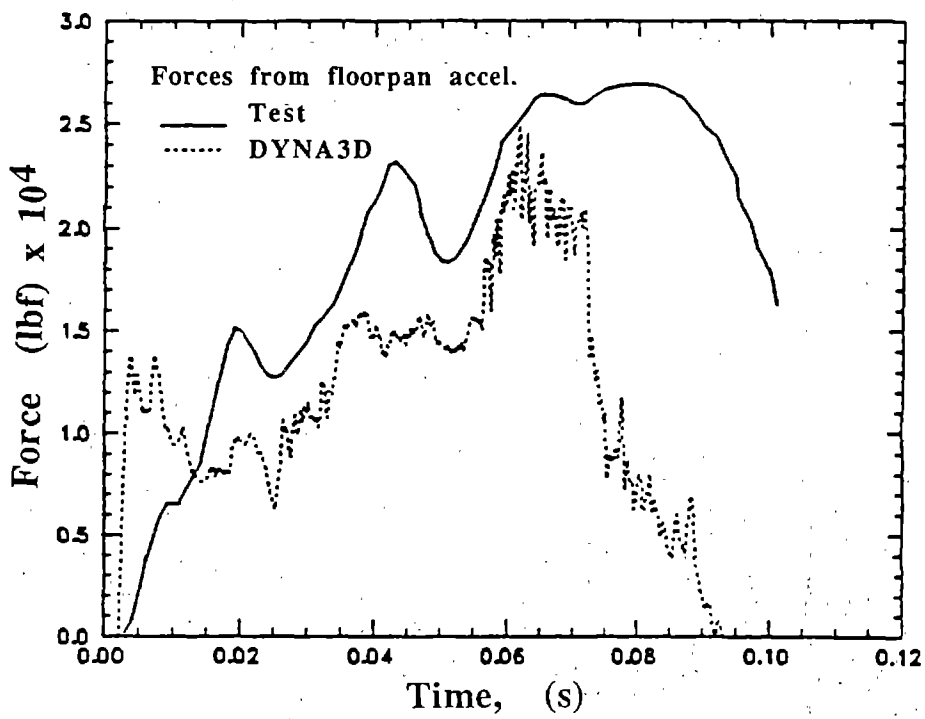


Figure 37. Comparison of test and DYNA3D results for bumper support impact.

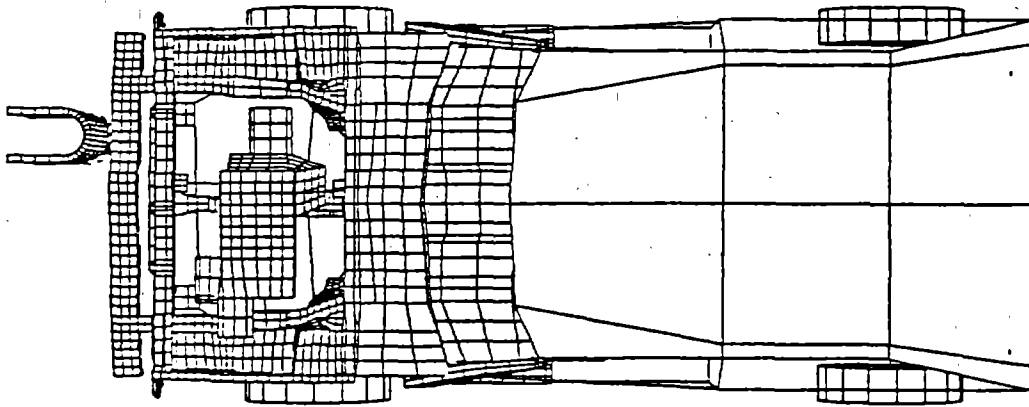


Figure 38. 254-mm (10-in) right-of-center bumper impact.

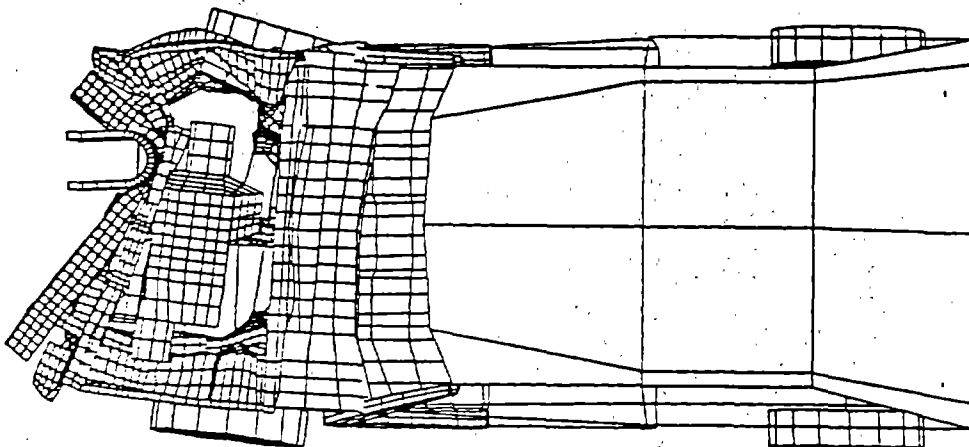


Figure 39. Deformed 254-mm (10-in) right-of-center impact model at 0.1 s.

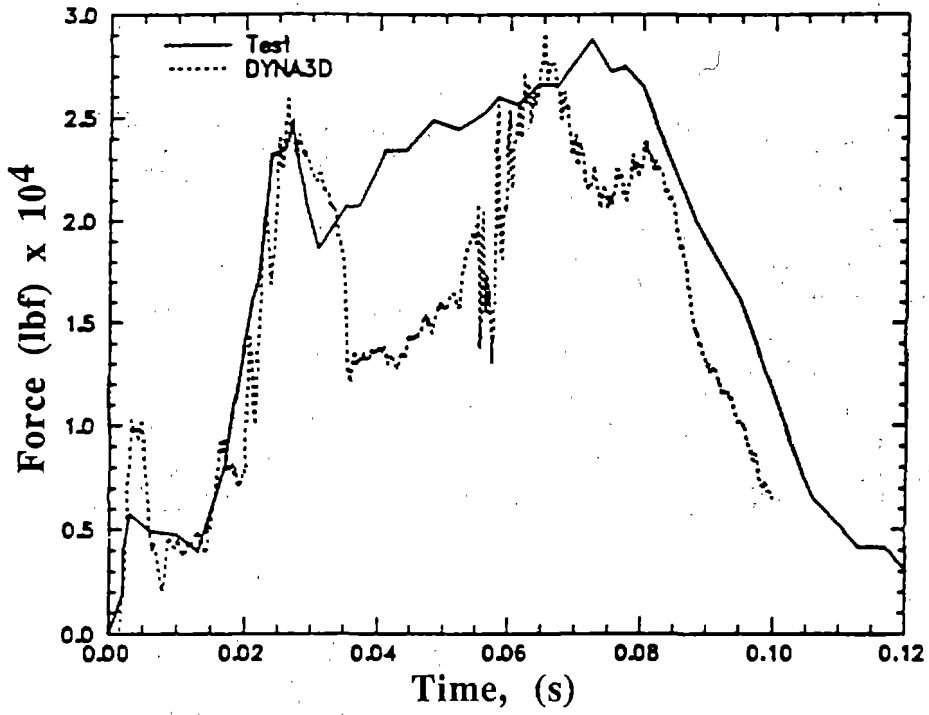


Figure 40. Comparison of test and DYNA3D results for 254-mm (10-in) right-of-center bumper impact.

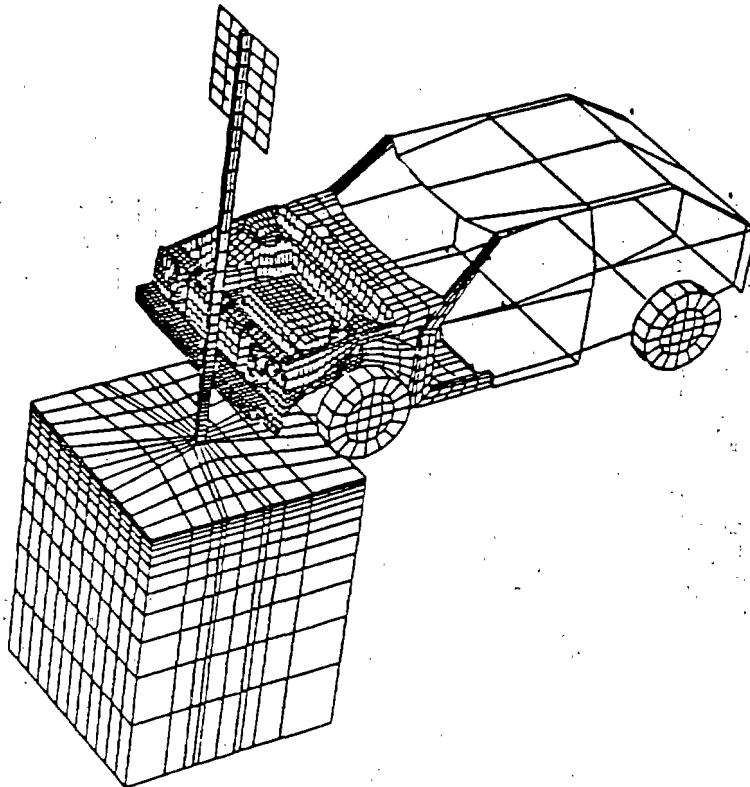


Figure 41. Modified u-channel sign post impact model.

used to keep the post in place and allow it to be pulled out from the soil during the impact. Figure 42 shows the deformed model at 0.1 s. Since it was not possible to mount load cells on the post, acceleration data at the c.g. of the vehicle was used to compare with the DYNA3D result. The comparison of the data is shown in figure 43. In this particular simulation, the DYNA3D acceleration history was also filtered by a 100 Hz low-pass filter. Note that the acceleration was quite low and the car did not slow down within the time span of 0.12 s. The simulation result has a couple of peaks that compare fairly well with the test data; but after 0.06 s, the correlation is poor. This was not surprising since the complex soil/u-post interaction played a key role in the vehicle response. Parametric analyses show that varying the coefficient of friction in the sliding contact surfaces greatly effected the vehicle response. Fine-tuning with the soil/u-post-sliding interface parameters and soil material model would improve the correlation. The DYNA3D analysis required 6.5 CPU hours on the Cray YMP for 0.1 s simulation time. The longer computer runtime was caused by the increased size of the model and to the smaller time step introduced by the small shell elements used in the u-post.

## **Section 2. Frontal Honda model impact with u-channel sign post**

Computer simulation of a Honda Civic impacting a u-channel sign post reported above were compared to an actual impact test conducted at the FOIL (93F010 in table 1).<sup>(45)</sup> The correlation between the test and the analysis results were fair, and it was pointed out that the discrepancies may be caused by the simplistic isotropic elastic-plastic soil model employed in the simulation. More sophisticated soil models were used in the modified Honda Civic model to determine the sensitivity of the vehicle response predictions to the soil constitutive assumptions. Coefficients of friction between the u-post and the soil were also varied. Results indicate that the response of the vehicle is influenced by the friction at the contact surfaces between the post and the soil.

## **DYNA3D Geological Material Models**

DYNA3D has an extensive material library that can be used for a wide range of applications. Three models are designed for the constitutive modeling of geological materials. These models are type 5 for the soil and crushable foam model, type 16 for the concrete/geological model, and type 25 for the extended two-invariant geologic cap model.

Type 5 (the soil and crushable foam model) is an elastic-plastic type of constitutive model originally developed for cellular concrete. The yield surface description in this model consists of a surface of revolution with a plane of end cap and the yield surface increases in radius with increasing pressure. The plane cap, normal to the hydrostatic in principal-stress space, is movable because of volumetric work-hardening. Plasticity is handled in two decoupled parts: volumetric and deviatoric; and the plastic flow is non-associative.

Type 16 (the concrete/geological model) was developed from model 10 (isotropic elastic-plastic-hydrodynamic model) by incorporating the option of a constant Poisson's ratio material, rate effects, and an improved treatment of spall and fracture. In addition, concrete reinforcement and loading-rate sensitivity for both the principal material as well as the reinforcement material are considered. The model also includes a damage scaling-factor and a pressure-hardening coefficient.

Type 25 is the extended two-invariant geological cap model where the yield surface and the cap have curved shapes in the first and second stress-invariant space. Two special features of this model are (1) exact satisfaction of algorithmic normality and consistency on the failure envelope; and (2) correct treatment of the singular cone at the corner. Eleven model parameters are required.

A principal objective of this study was the determination of the variation of vehicle response because of a range of soil material properties. Type 5 was selected for the present study because of its simplicity in comparison with the other two models. Material type 5 can be characterized by six parameters: shear modulus  $G$ ; bulk modulus  $K$ ; yield function constants  $a_0$ ,  $a_1$ ,  $a_2$ ; and tensile pressure cutoff. These parameters can be characterized using conventional laboratory tests on soil samples.

### Finite Element Model Soil Properties

Three sets of material properties were used in this parametric study. The first set modeled an elastic-plastic constitutive relationship. Table 2 shows the model parameters for the elastic-plastic model. The second set of parameters was based on a constitutive model developed from the soil samples taken from Antelope Lake, Tonopah Test Range, Nevada. These soils consisted of very stiff silty clays over very dense, slightly sandy silts with occasionally gravely sands.<sup>(47)</sup> The geotechnical properties and material type 5 model parameters of Antelope Lake soil are presented in table 3 and the pressure-volumetric strain curve is shown in table 4. The third set of properties was based on experimental data performed at the Sandia National Laboratory. The desert soil was basically a sand-clay mixture.<sup>(48)</sup> The soil properties and the material type 5 model parameters are presented in table 5, and the pressure-volumetric strain curve is shown in table 6. Notice that material type 5 model parameters have been converted from the original English units to the metric units used for the modified Honda model.

To compare the initial relative stiffness among the three material models, an equivalent Young's modulus was derived for the two material type 5 models using the following isotropic elastic constants:

$$K = E/[3(1-2u)] \quad \text{and} \quad G = E/[2(1+u)],$$

where  $K$  is the bulk modulus,  $G$  is the shear modulus, and  $u$  is the Poisson's ratio. The equivalent Young's modulus and Poisson's ratio are also listed in tables 3 and 5. Based on these equivalent stiffnesses, the Sandia desert soil is the softest (20.7 MPa), the original elastic-plastic model is slightly stiffer (100 MPa), and the Antelope Lake soil is the stiffest (997.6 MPa).

Table 2. Material type 3: elastic-plastic.

Young's modulus (MPa)	100.0
Poisson's ratio	0.3
Yield stress (MPa)	0.4

Table 3. Material type 5 model for Antelope Lake soil.

Parameters or Properties	Average
Bulk density (metric ton/mm <sup>3</sup> )	1.874e-9
Unloading bulk modulus (MPa)	1523.82
Shear modulus (MPa)	358.55
Poisson's ratio	0.350
Pressure cutoff (MPa)	-0.550
Yield function constant a <sub>0</sub> (MPa <sup>2</sup> )	0.158
Yield function constant a <sub>1</sub> (MPa)	0.124
Yield function constant a <sub>2</sub>	0.024
Equivalent Young's modulus (MPa)	997.60
Equivalent Poisson's ratio	0.391

Table 4. Pressure-volumetric strain curve for Antelope Lake soil.

Pressure (MPa)	Volumetric Strain *
0.00	0.000
0.30	-0.073
1.20	-0.134
2.50	-0.191
4.99	-0.263
9.03	-0.313
15.03	-0.333
40.00	-0.390
70.00	-0.460

\* Volumetric strain is defined as the natural log of relative volume.



Table 5. Material type 5 model for Sandia desert soil.

Parameters or Properties	Average
Bulk density (metric ton/mm <sup>3</sup> )	1.425e-9
Unloading bulk modulus (MPa)	13.80
Shear modulus (MPa)	8.27
Poisson's ratio	0.25
Pressure cutoff (MPa)	-10.00
Yield function constant a <sub>0</sub> (MPa <sup>2</sup> )	7.28e-4
Yield function constant a <sub>1</sub> (MPa)	0.04
Yield function constant a <sub>2</sub>	0.69
Equivalent Young's modulus (MPa)	20.7
Equivalent Poisson's ratio	0.25

Table 6. Pressure-volumetric strain curve for Sandia desert soil.

Pressure (MPa)	Volumetric Strain *
0.00	0.0
0.69	-0.0513
2.07	-0.1625
4.14	-0.3567

\* Volumetric strain is defined as the natural log of relative volume.

### Parametric Analysis

The FE model for the u-channel sign post impact simulation consisted of a vehicle mesh and a post/soil mesh. The vehicle mesh was identical to the LLNL modified Honda model described in reference 49. The combined post/soil discretization used shell elements and solid elements to represent the post and the soil, respectively. Contact surfaces, or *slidelines* were prescribed between the post and the soil, and also between the two soil blocks (figure 44). A complete analysis matrix together with the corresponding figure number showing the vehicle c.g. acceleration history is presented in table 7. A range of friction coefficients was also applied to the slidelines. The analyses associated with Antelope Lake soil and Sandia desert soil in table 7 used 0.3 coefficient of friction for the slidelines between the sign-post and the soil. But friction coefficients of 0.0, 0.15,

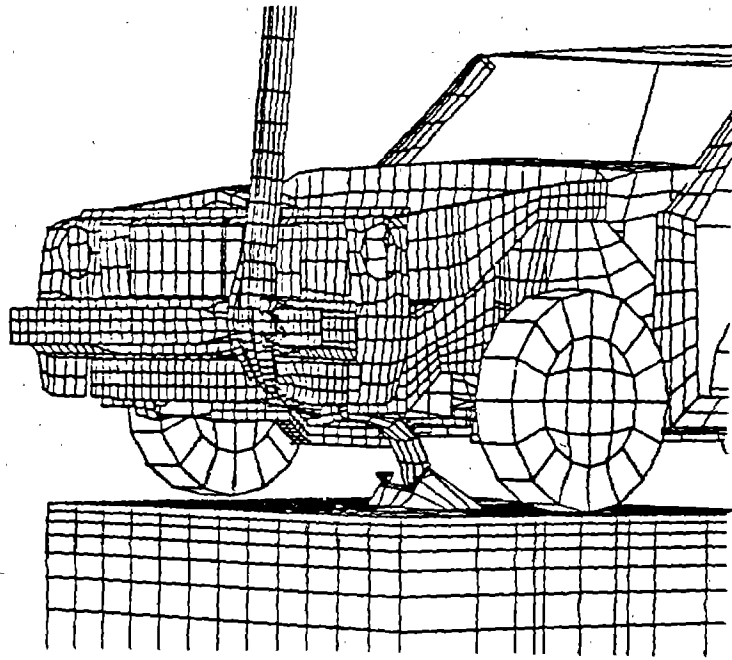


Figure 42. Deformed u-channel sign post impact model at 0.1 s.

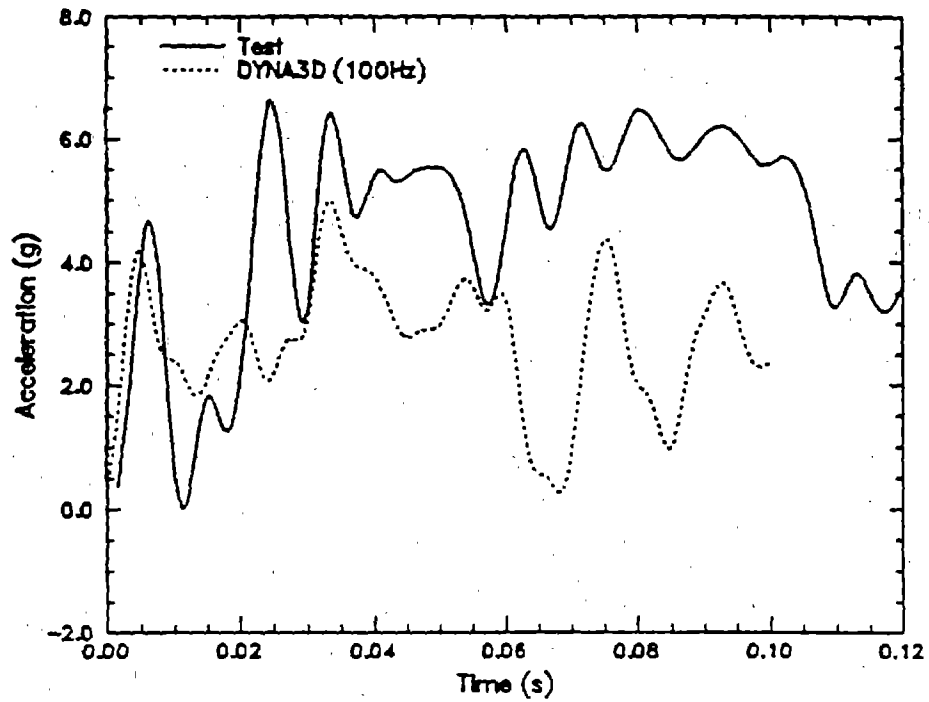


Figure 43. Comparison of test and DYN3D results for u-channel sign post impact model.

and 0.5 were also evaluated. Table 8 identifies the figure number for the acceleration history plots resulting from these friction coefficient parametric analyses. Note that all the analysis accelerations were extracted at the c.g. of the vehicle and they have been low-pass filtered at 100 Hz. Figure 45 presents the acceleration history from the original elastic-plastic type 3 soil model. In this analysis, no friction was enforced between the post and the soil. Generally, the analysis acceleration data were below the test data, particularly between 0.06 and 0.1 s. The same kind of behavior can be observed from a type 3 Antelope Lake soil analysis in which the coefficient of friction was also zero.

Figure 46 compares the accelerations between the two type 5 models that were based on the Antelope Lake and Sandia desert soils. The Antelope Lake type 5 model correlated very well with the test data up to 0.1 s. After 0.1 s, the acceleration test data diminished to zero, while the simulation results fluctuated about -6.0 g. The acceleration from the Sandia desert type 5 model was always lower than the test data. Figure 47 compares the accelerations between the two type 3 models from the Antelope Lake and Sandia desert soil analyses. The same behavior noted in figure 46 can be observed in figure 47 as well, although the correlation with the test data is better with the type 3 Sandia desert model than with the type 5 model.

Figures 48 and 49 compare the responses between type 3 and type 5 models for the Antelope Lake soil analysis and the Sandia desert soil analysis, respectively. Figure 48 clearly showed that the accelerations from type 3 model and type 5 model from the Antelope Lake analysis were essentially identical. On the other hand, there was some difference between the type 3 and type 5 models from the Sandia desert soil analysis (figure 49). It was noted that the pressure in the soil surrounding the post was quite low and therefore the volumetric response remained elastic. As the sign post was pulling out from the soil due to the impact, the deviatoric response of the soil became more prominent. Since there is no strain hardening in the soil model and the deviatoric response is perfectly plastic at any constant pressure, the behavior is similar to those of type 3 material model.

Based on the above results, it is clear that if the deviatoric behavior of the soil is significant, the coefficient of friction prescribed for the slidelines between the post and the soil, and between the soil blocks has a strong influence on vehicle response. To investigate the sensitivity of the friction coefficient, analyses with friction coefficients of 0.0, 0.15, and 0.5 were evaluated. The results are plotted in figure 50 for the Antelope Lake soil model and in figure 51 for the Sandia desert soil model. In general, the results from the analyses with 0.15 and 0.5 friction coefficients showed similar response patterns, but the one with 0.0 friction coefficient deviated drastically from the others after the initial impact at about 0.03 s. The sign post was also deformed in a different manner depending on whether the coefficient of friction was included in the slidelines. With no friction, the sign post was bent into a curve at the base (figure 52). On the other hand, with friction included, the post was pushed completely into the soil as depicted in figure 53.

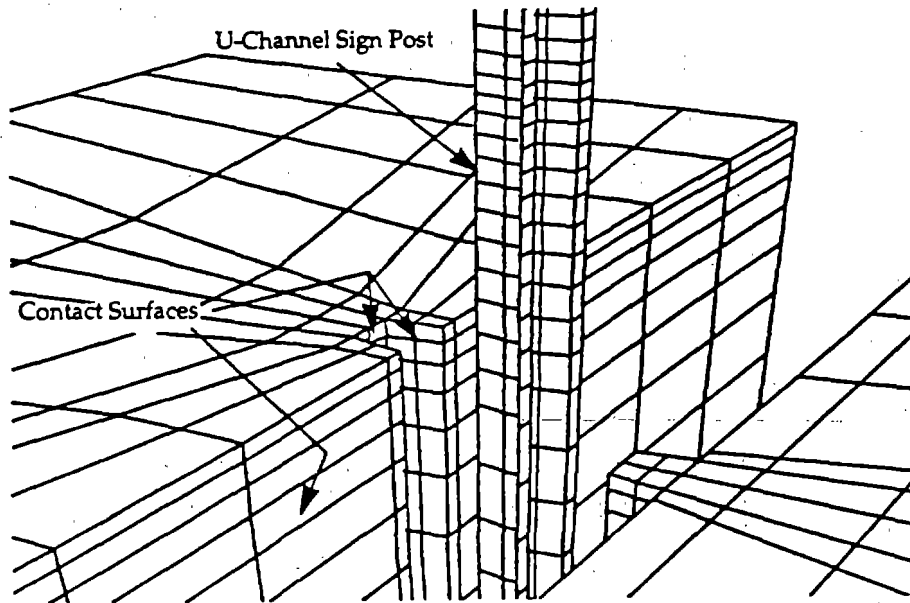


Figure 44. Exploded view of soil/u-channel sign post showing slideline surfaces.

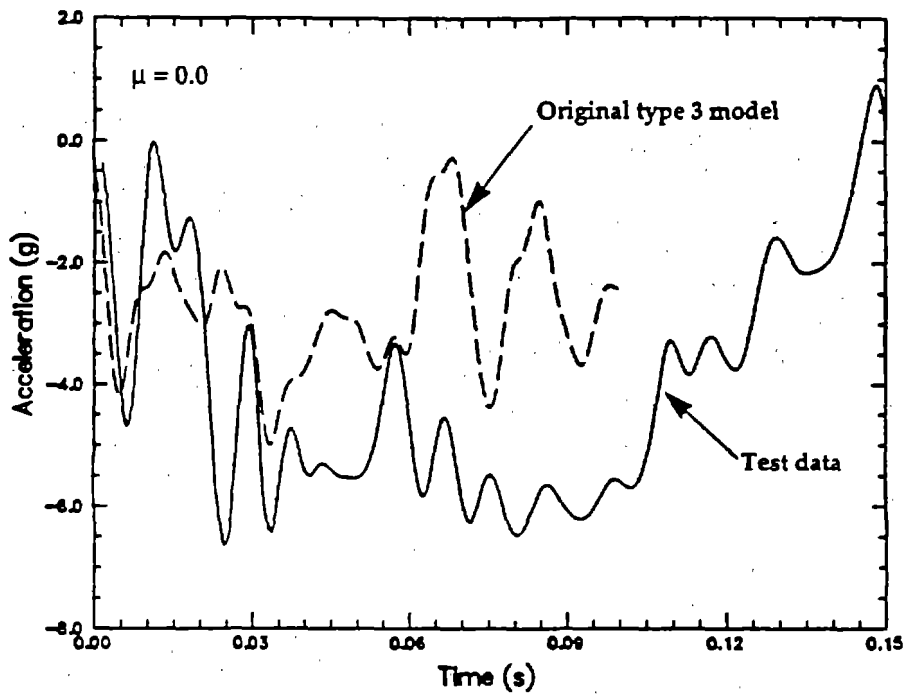


Figure 45. Acceleration history of the original type 3 soil model.

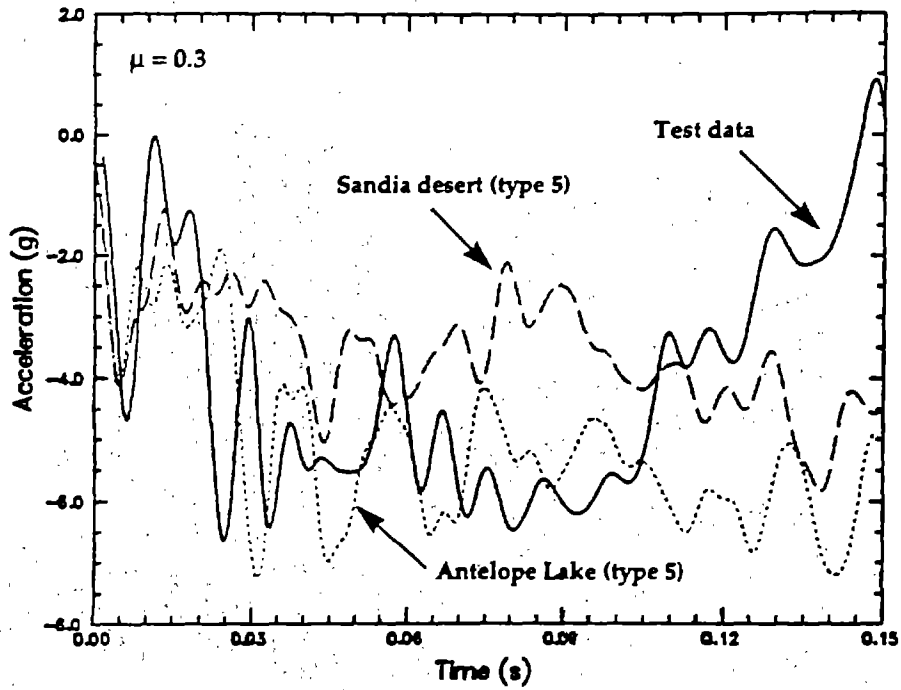


Figure 46. Acceleration histories of type 5 soil models based on Antelope Lake and Sandia desert soil.

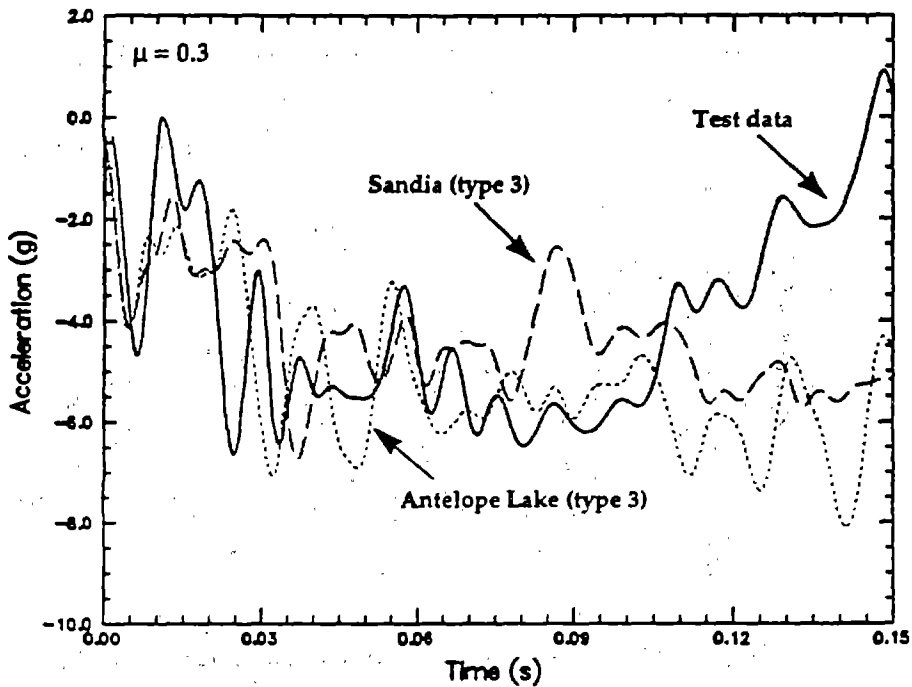


Figure 47. Acceleration histories of type 3 soil models based on Antelope Lake and Sandia desert soil.

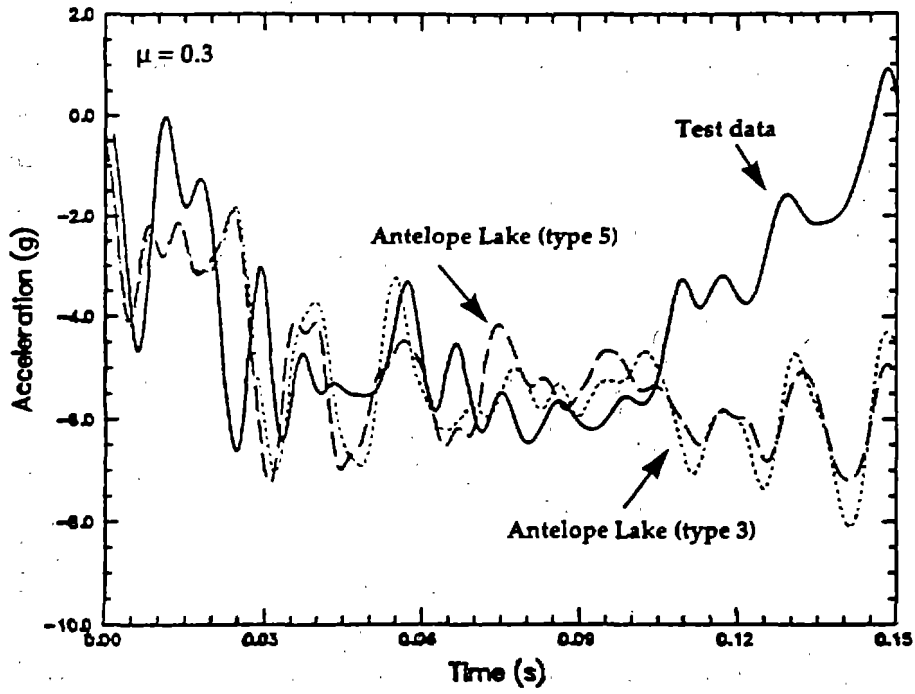


Figure 48. Acceleration histories of type 3 and type 5 soil models based on Antelope Lake soil.

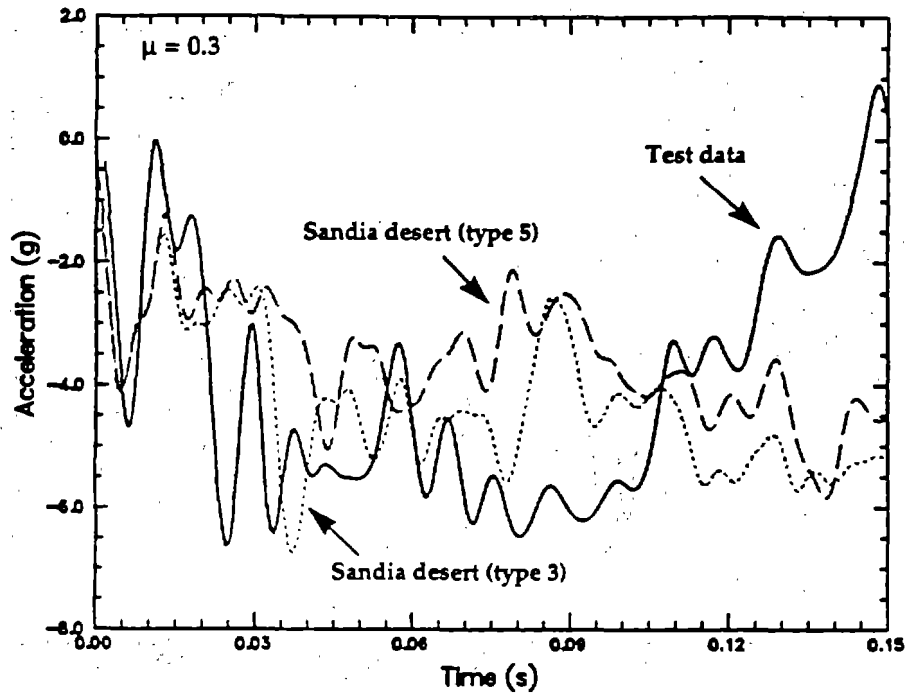


Figure 49. Acceleration histories of type 3 and type 5 soil models based on Sandia desert soil.

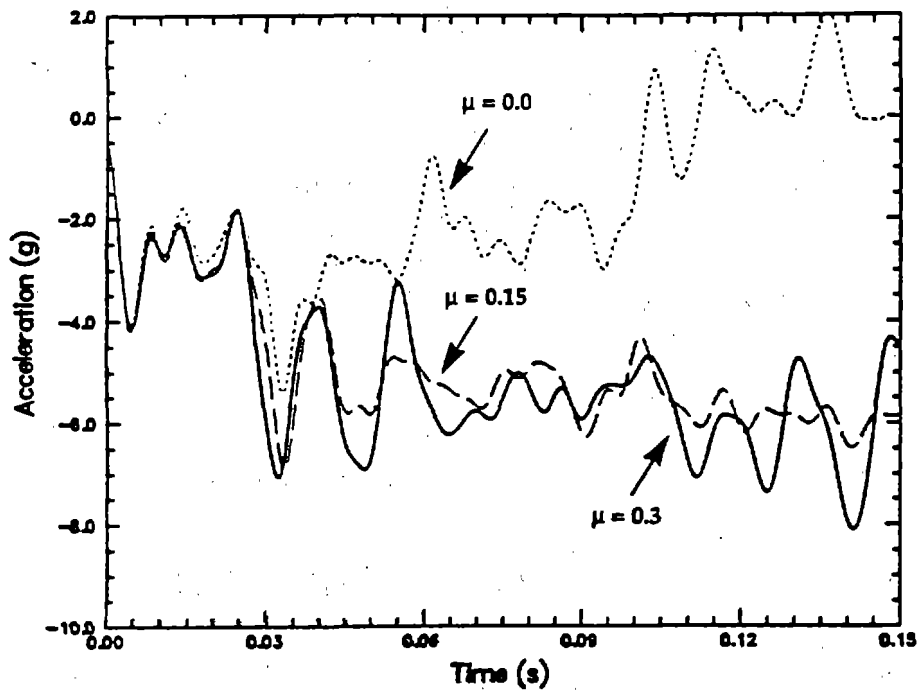


Figure 50. Acceleration histories of type 3 soil models based on Antelope Lake soil with different friction coefficients.

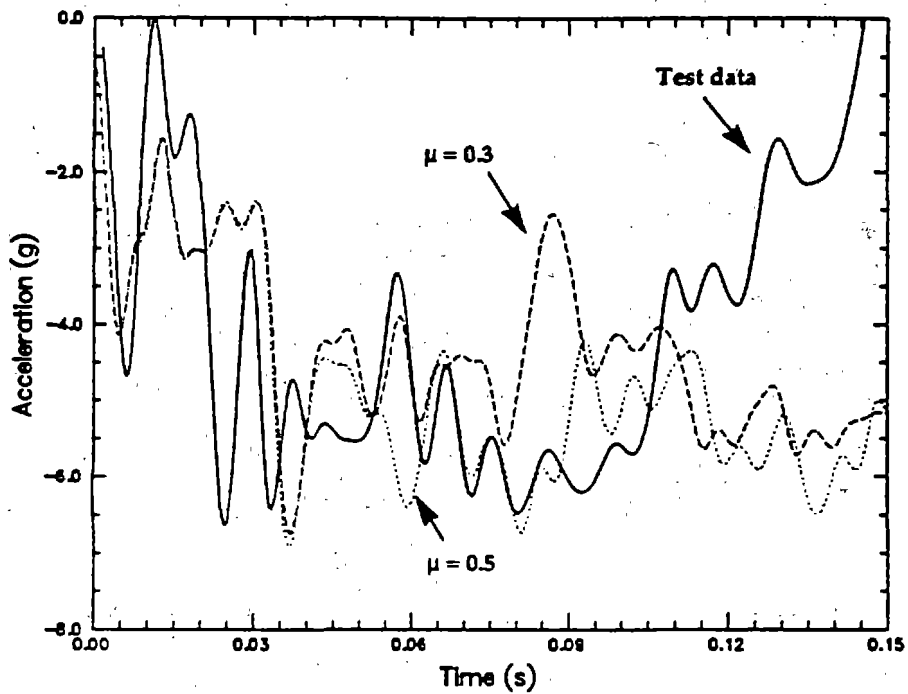
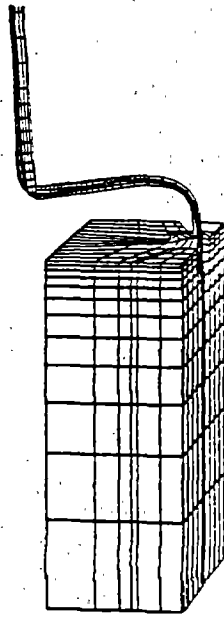
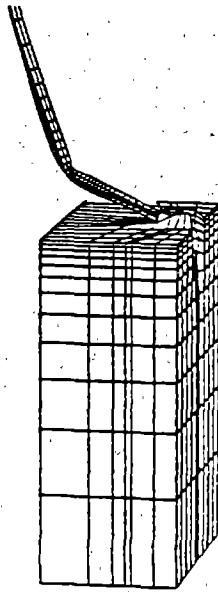


Figure 51. Acceleration histories of type 3 soil models based on Sandia desert soil with different friction coefficients.



time = 0.155 s

Figure 52. Deformed shape with friction coefficient = 0.0.



time = 0.155 s

Figure 53. Deformed shape with friction coefficient = 0.15.



## Conclusions

The results from the two parametric analyses clearly indicated that:

1. The behavior of the soil in the u-channel sign post impact simulation is primarily deviatoric. Because of the low pressure generated in the soil from the impact, a more sophisticated model, such as the DYNA type 5 material model that includes volumetric strain hardening and pressure dependency of the deviatoric yield function, may not necessarily improve the soil behavior.
2. The response of the vehicle is very much influenced by the coefficient of friction prescribed in the contact surfaces between the post and the soil.
3. None of the simulations performed so far was able to correlate satisfactorily with the test data after 0.10 s.

To improve the fidelity of the u-channel sign post impact simulation, the interaction between the post and the soil need to be understood better. Well designed experiments such as static pull out test of the post or dynamic impact test would provide the data to investigate the true slipping mechanism between the post and the soil. With better understanding of the slipping mechanism, it would be possible to improve the impact simulation by either developing an appropriate soil constitutive model or devising a new modeling scheme for the sign post/soil slippage phenomenon. The experimental data obtained from the pull-out test would provide the necessary data to validate the new material model or to prove the new modeling scheme.

### Section 3. Vehicle model refinement

With the advance of both computer hardware and software technologies in the past few years, the use of computer simulation in designing highway roadside safety features have become an attractive alternative to the traditional design by testing approach. Initial results from a rigid pole and u-channel sign post impact simulation using a DYNA3D FE model of a 1992 Honda Civic Hatchback developed in the FHWA Pre-VISTA program were promising.<sup>(50)</sup> The Honda FE model has since been modified to include the engine cradle failure observed in the crash tests but were neglected in the earlier analyses. Parametric studies were conducted to optimize the model as well as to determine the proper failure mechanism modeling technique. From the results of these analyses and the correlation with the deceleration histories of the Honda Civic crash tests, a set of general modeling criteria was developed for the Honda frontal impact model.<sup>(45)</sup> Because of the general nature of these criteria, they may be applied to other vehicle FE impact models.

### Model Modification Methodology

Accurate computer impact simulation of roadside safety features requires FE models that can capture the dynamic response of the impacting vehicle and the resulting structural deformation of the roadside features. Furthermore, the fidelity of the vehicle model is crucial to the structural behavior of the roadside features. Because the FE mesh of the vehicle is generally more complex than the roadside feature models, considerable efforts are required to debug and fine tune the vehicle model throughout the analysis.

Typically, the FE model of a vehicle is first developed by model developers, or mesh modelers, and then passed to the analysts to perform the impact simulation. The FE mesh is usually generated from digitized data of the vehicle components. Many modeling choices, such as mesh discretization, assumptions for the boundary conditions between individual parts, and selection of contact surface options, are entirely up to the mesh modeler. The initial mesh is usually a fairly detailed model as the model developers may not necessarily know in full detail about the final applications of the model. During the debugging and fine-tuning phase of the simulation, the analysts frequently have to modify the vehicle mesh to address certain model deficiencies and unanticipated conditions that occur in the analyses, as in the case of the Honda Civic model.

The Honda FE model developed in the Pre-VISTA program was used for rigid pole impact simulations at three different bumper locations and for another impact analysis onto a u-channel sign post that was embedded in soil. The FE model for the rigid pole/center bumper impact simulation is shown in figure 54. The steps involved in modifying the original mesh to the final model are presented in a flow chart shown in figure 55. The components that were eliminated and significantly modified are also listed along the flow chart. The principal motivation for the modifications is to create a CPU-efficient and numerically stable model so that the impact simulations can be completed in a few CPU hours with a CRAY YMP or a CPU day with a high-end computer workstation.

The initial Honda mesh included representations of many components that are either non-structural or have very low frontal impact resistance. These parts were completely eliminated from the model. Elimination of these components did not adversely alter the vehicle response but did offer the benefits of reduced model size. Many load-carrying members at the front end of the Civic that are critical to the frontal impact vehicle response were modified to enforce the proper boundary conditions and the contact surface definitions between the various components. Since the cradle was buckled and the rear cradle engine mount was sheared away from the engine during the center bumper rigid pole crash test, the cradle and its engine mounts were evaluated in parametric analyses and were subsequently modified to include the observed failure.

Only the front end of the Civic was meshed in detail. Unchanged from the original mesh, a rigid material was used to represent the rest of the vehicle body panels. Discrete mass points were added to the model to accurately represent the total mass, the moment of inertia, and the c.g. of the vehicle.

### **Cradle Failure Parametric Analyses**

The cradle in the Honda Civic is located on the center line of the vehicle and is a direct link between the cross member in the front and the floor pan in the back of the car. It also supports the engine and transmission assembly via a bracket mount at each end of the cradle. Clearly, the cradle and its engine mounts are the key load transferring mechanism for the center bumper impact. Table 9 list the cradle engine mount configurations investigated in the cradle parametric analyses. The study included analyzing different combinations of forward and aft engine mounts models. Figures 56 and 57 show the cradle with rigid beams and the shell engine mounts configurations, respectively. To simulate the failure observed in the crash test, node spot welded slidelines were used at

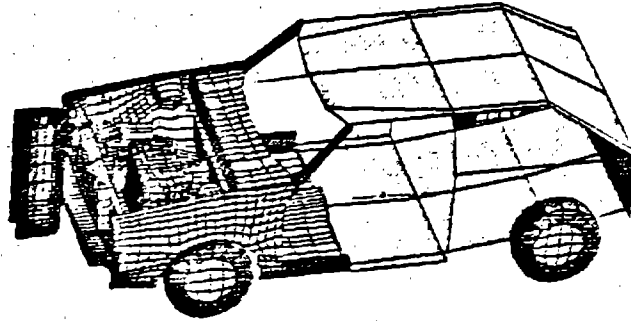


Figure 54. Rigid pole impact model.

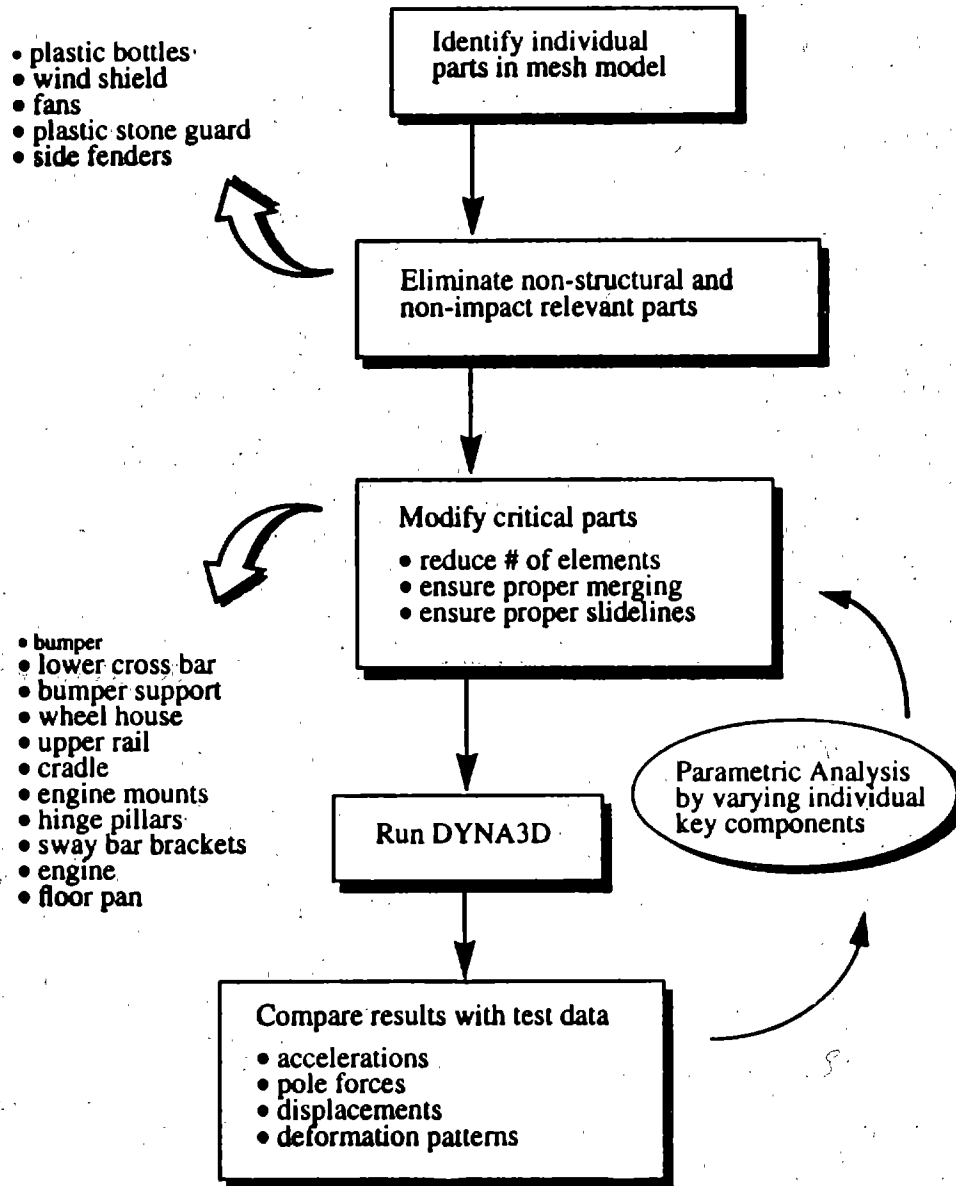


Figure 55. Model modification flow chart.

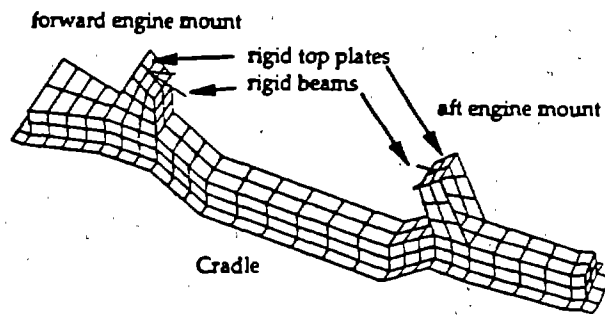


Figure 56. FE mesh of the original cradle with rigid beam engine mounts.

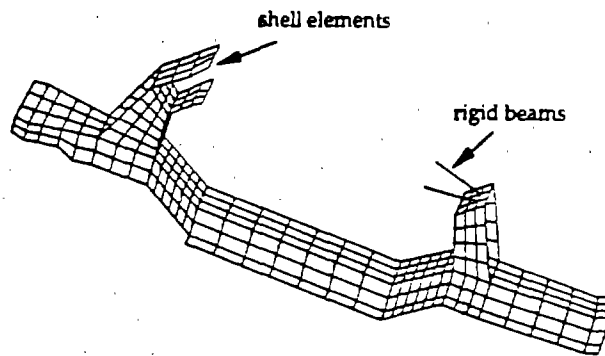


Figure 57. FE mesh of the modified cradle with forward shell and aft rigid beam engine.

the aft engine mount. The deformed shape of the buckled cradle from the rigid-pole center bumper impact simulation is depicted in figure 58. Note that the aft engine mount is separated from the engine, an effect similar to what was observed in the crash test.

The results of the parametric analyses showed that the deceleration at the c.g. of the vehicle is dependent on the engine mounts configurations. Figure 59 compares the vehicle c.g. decelerations of a model that has rigid beams for both the forward and aft engine mounts to another model that uses normal beams as the engine mounts. Similarly, correlation of the c.g. decelerations between a fwd shell with an aft rigid beams engine mount model and a springs engine mount model is shown in figure 60. The measured vehicle c.g. deceleration from the crashed test is also plotted in those figures. The results from the simulations and the test data both generally capture the 0.12 s impact duration time. However, though the temporal correlation with the test data at the early times are quite good, the simulation results do not replicate the peaks and valleys of the test data.

The decelerations from the simulations shown in figures 59 and 60 were based on the nodal deceleration at the c.g. of the vehicle model. The c.g. location in the FE model is very close to the true c.g. location of the Civic and is situated at the last row of elements in the floor pan as shown in figure 61. As mentioned earlier, the rear portion of the Civic was modeled with rigid material as no structural deformations were expected in those regions. To tie the rear vehicle rigid body to the detailed vehicle mesh at the front, the last row of the floor pan elements were modeled with the same rigid material of the rear body panels.

During the crash test, data from two accelerometers mounted on the left and right rear seats in the Civic were also collected. As expected, the two deceleration histories were practically identical. Figure 62 shows the measured rear right seat deceleration plotted against the same analytical deceleration history shown earlier in figure 60 for the fwd shell with aft rigid beam model. The correlation between the two data is very good, both in terms of temporal phasing and peak values. Effectively, the nodal deceleration at the c.g. of the vehicle FE model represents the deceleration of the entire rear portion of the vehicle. For this model, it is inappropriate to compare the FE model's c.g. nodal deceleration to the true c.g. deceleration obtained from the crash test.

### **Modeling Criteria**

Based on experience in modifying the FE model and from observing the c.g. deceleration correlation of the parametric analyses results with the crash test data, a set of modeling criteria was developed for the Honda Civic FE model. Because of their generic nature, the following criteria may be used as guidelines on developing other FE vehicle impact models.

**Analysis objective.** The objective of the analysis and the intended usage of the vehicle model should be clearly defined before the meshing begins. If the objective of the analysis is to evaluate the impact response of the occupants, the meshing of the vehicle FE model needs to be finer and the interior of the vehicle should be modeled in more

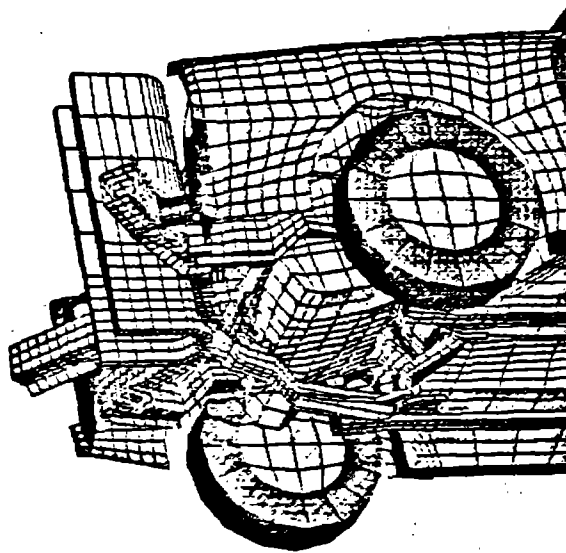


Figure 58. Buckled cradle in the rigid pole center bumper impact simulation.

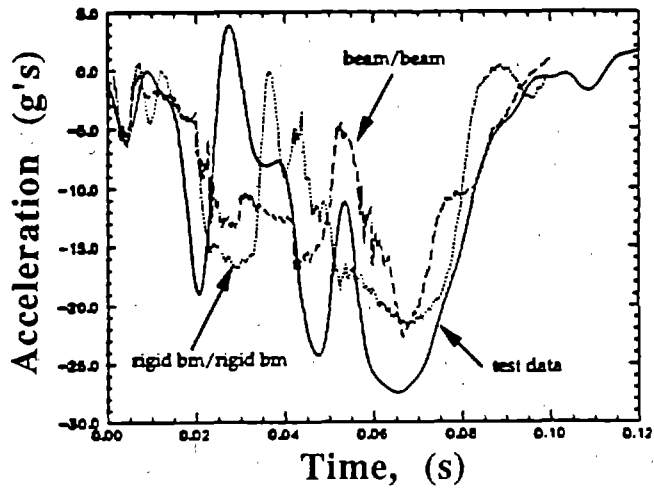


Figure 59. Correlations between rigid beam/rigid beam and beam/beam engine mounts from the center impact simulation.

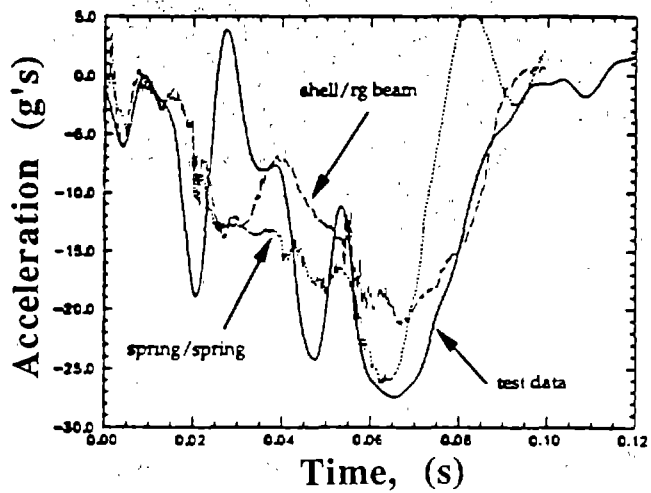


Figure 60. Correlations between shell/rigid beam and spring/spring engine mounts from the center bumper impact simulation.

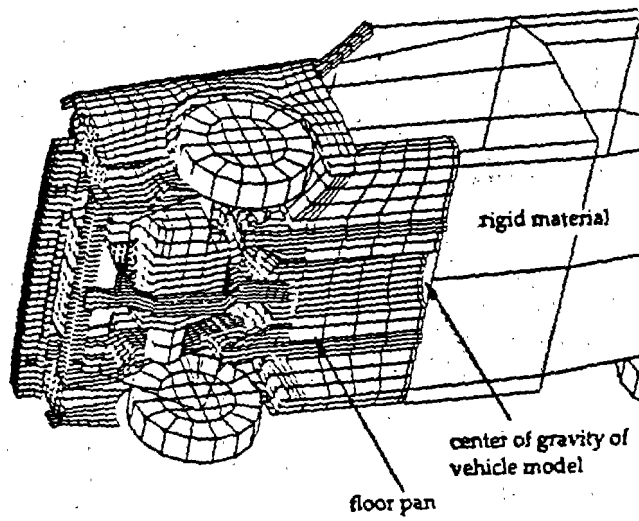


Figure 61. Location of c.g. in the vehicle model.

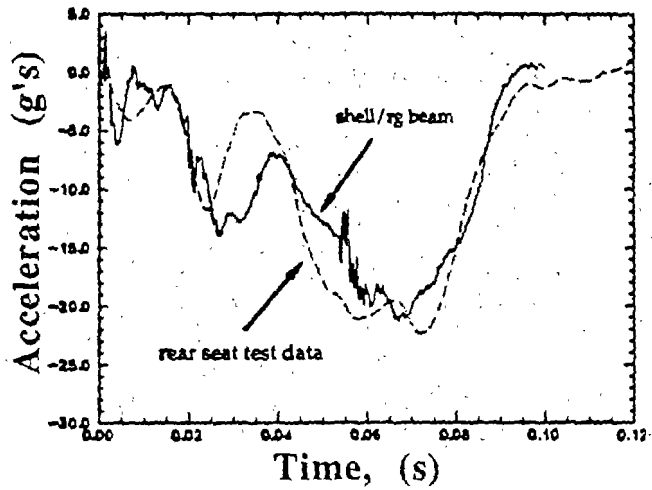


Figure 62. Correlations between shell/rigid beam model and rear seat deceleration data from the center bumper crash test.



detail. On the other hand, if the objective is to design roadside safety features, the meshing of the vehicle model needs to be modeled in detail only in the impact region and in the areas that large deformations are expected.

**Computer resources.** The computer resources available for the analysis should be considered in determining the optimal mesh size for the vehicle model. When fast computers are not available, the ability to perform parametric analysis for model modification and improvement for a very fine vehicle model will be limited. At LLNL, a rigid pole impact analysis with the Honda mesh for a 0.1 s simulation time typically required about 3.5 CPU hours with a CRAY YMP supercomputer.

**Boundary conditions.** Boundary conditions between the vehicle parts must be properly defined. In fact, adjusting the boundary conditions in a model that has been modified is the most time consuming step in the model refinement process. Vehicle components are frequently joined by spot-welds. They are typically represented in the FE model by nodal constraints or other methods that are dependent on the nodal numbering scheme. Since a modified model usually alters the node numbers in the individual parts, new nodal constraints lists have to be generated. Therefore, good planning and meshing strategies must be carefully laid out for the initial mesh to minimize the subsequent model modification effort.

Contact surfaces, or slidelines, must be properly defined to provide the correct load path from the impact. Twenty contact surfaces are employed in the Honda model, and they need to be adjusted whenever the model is modified. However, at the expense of longer computing time, the automatic-contact-surface option in DYNA3D is recommended as an alternative to the individual contact surfaces. Using automatic contact would eliminate any update to the contact surface definition after a model has been modified.

**Rigid Materials.** Rigid materials can be applied to the vehicle components that are acting as a rigid body or undergoing insignificant deformation. Since rigid materials have limited degrees of freedom, it is an expedient way to reduce the size of the vehicle model. However, the presence of rigid materials may alter the load path and can also change the deformation patterns significantly, so they should be used with care. Another side effect of rigid materials is that the responses of the individual parts are governed by the response at the center of mass of the rigid material volume. For example, if the rigid material volume does not experience any rigid body rotation, the response of all the individual parts are essentially identical to the response at the c. g. of the rigid material. In the case of the Honda model, the c.g. of the FE model is modeled with a rigid material identical to the one used to define the aft body. Therefore, the deceleration derived from the simulation at the vehicle c.g. location is the response of the aft body, rather than the true c.g. response of the vehicle. This sort of side effect should be avoided.

**Beam element Usage.** Beam elements are typically used to represent linkages and bars found in the vehicle. Frequently beams are also used as an approximated representation of more complex two-dimensional components. However, beam elements would not be a good choice if the two-dimensional components are experiencing large deformation, such as crushing.

**Failure modeling.** Failure mechanisms should be incorporated into the model when failure is expected or observed from tests. Without a failure mechanism in the model, the load path would not be established accurately and the deformation patterns would also be questionable. The node spot welded (nsw) contact surfaces used in the Honda model were able to simulate the breakage of the cradle engine mount. However, it should be pointed out that the failure in the nsw formulation occurs in one time step while the real failure may have occurred at a longer duration.

**Material properties.** Generally, the mechanical properties for various vehicle components are not well identified. So the properties from a generic automotive material are used in the FE, as in the case of the Honda model. Obviously, more identifiable materials for the components and better material properties are badly needed as they would improve the validity of the computer model. Moreover, study on strain rate effect is another area that would improve the fidelity of computer impact simulation.

**Interaction between modelers and analysts.** Because of the complexity of the model, analysts need to know the rationale and underlying assumptions implemented by the model developers so that the model may be modified diligently and optimally as required. Since the analysts have more experience running the DYNA3D code, they may have ideas as to how to model certain components by exercising special features of the code. The importance of interaction between the modelers and the analysts should not be overlooked, especially during the mesh generation phase.

**Validation Criteria.** In performing the parametric analyses and correlating analysis data with test data, it became evident that to evaluate the performance of various models, validation criteria that qualify a model being good or poor must first be established. In the impact analysis of the Honda, the reference data for all the parametric analyses and correlations was based solely on the deceleration histories at the c.g. of the vehicle. The c.g. deceleration is certainly a good reference, but is it sufficient to qualify a model as being thoroughly validated? At the present time, validation criteria do not exist and the development of such criteria should be one of the highest priorities in the vehicle impact computer simulation community.

## **Summary**

The methodology employed in modifying a DYNA3D FE model of a Honda Civic used in impact simulation was presented. Parametric analyses were performed in order to debug, fine-tune, and capture the failure in the engine cradle which was observed in crash tests. The analysis results and their correlation with the test data were also presented. Using the results from the analyses and experience in modifying the vehicle model, a set of modeling criteria was developed for the Honda Civic FE model. These criteria could be used as guidelines in generating other impact vehicle models.

Table 7. Soil models parametric analysis matrix.

Figure #	Original	Antelope Lake Soil		Sandia desert Soil	
	Type 3	Type 3	Type 5	Type 3	Type 5
2	x				
3			x		x
4		x		x	
5		x	x		
6				x	x

Table 8. Friction coefficient parametric analysis matrix.

Figure#	Soil Model	Friction Coefficient			
		0.0	0.15	0.3	0.5
7	Antelope Lake (Type 3)	x	x	x	
8	Sandia desert (Type 3)			x	x

Table 9. Engine cradle parametric analysis matrix.

Forward Engine Mount				Aft Engine Mount			
shell	rigid beams	beams	spring	rigid beams	beams	spring	no support
x				x			
x					x		
x						x	
x							x
	x			x			
		x			x		
			x	x			
			x			x	

## Section 4. Ford Festiva FE model impacting a rigid pole

FHWA funded this research to investigate the feasibility and reliability of using simplified FE models that can be analyzed overnight on a workstation to study the behavior of vehicles during impacts into roadside structures.<sup>(17)</sup> A 1992 Ford Festiva was used as the basis for this FE model, partly because it is representative of the 820C class of vehicles specified in NCHRP Report 350 and partly because full-scale test data on centerline impacts were available for three similar Ford Festivas for comparison and validation studies.<sup>(51)</sup> A report details the development of the FE model, the element and material types used, the contact surface definitions used, and the modeling strategies and techniques used.<sup>(52)</sup> A brief overview is presented of the DYNA3D simulation results for three different rigid pole impact cases: (1) centerline; (2) left-of-center; and (3) right-of-center.

### Model Description

The model (1992 Ford Festiva) had measured dimensions of 3.51-m total length, 1.42-m height, and 1.5-m total width. It was developed using the INGRID preprocessor and was later converted to the TrueGrid preprocessor.<sup>(53)</sup> The vehicle model consists of 28 parts, 4,295 nodes, 60 beams, 2,898 shell elements, and 633 solid elements. The following assumptions were made in the development of this model:

1. Only structural components of the vehicle considered to be part of the load path in a frontal collision were modeled.
2. Dimensions and shapes used in this model were based on physical measurements taken on a 1992 Ford Festiva used at the FOIL.
3. The mass of the various parts of the model was distributed to ensure that the center of mass of the model approximately agreed with actual 1992 Ford Festiva measured at the FOIL. No effort was made to match the mass moments of inertia.
4. Parts were generally joined by merging adjacent nodes. Tied contact surface definitions were used to merge parts with incompatible meshes.
5. The suspension system was modeled using beam elements.
6. Shell element aspect ratios were generally kept below four.

Figure 63 is a view of the underside of the model showing the engine cradle and its attachment point to the lower core support and firewall, the tires, the rims, and the floor pan. Details of the actual model construction including material properties and slide line definitions used are fully documented.<sup>(52)</sup>

### Finite Element Analysis

The FE model of the 820C vehicle was designed to simulate an impact into a 218-mm diameter rigid pole at a zero-degree impact angle and 32 km/h impact velocity. Three rigid pole impact scenarios were simulated: a centerline impact, a 254-mm offset to

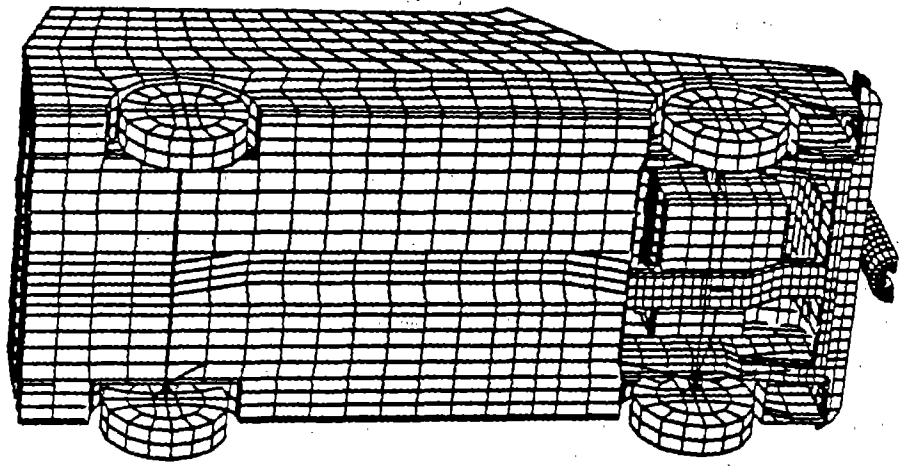


Figure 63. Festiva FE model.

the right-of-the-centerline impact, and a 457-mm offset to the left of the centerline impact. The FEA results were compared with full-scale test results for the centerline impact. The analysis results for the two off-center impacts were not compared with test data since no test data was available.

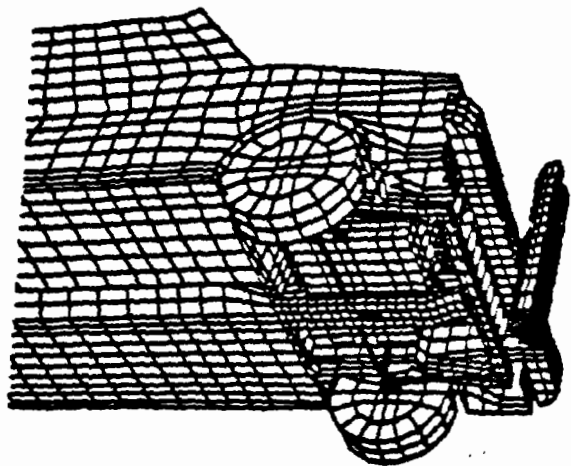
The total impact simulation time for all three test was 120 ms. This allowed the vehicle to strike the pole, reach its maximum deformation, rebound from the pole, and then lose contact. Plot states were collected at 2 ms intervals and the time history data was collected at 0.5 ms intervals.

The rigid pole was modeled as a hollow semicircle solid. Because reaction forces cannot be directly calculated during the DYNA3D analysis, two indirect approaches were used to obtain reaction forces on the rigid pole. In the first approach, the pole is given a relatively large mass compared to that of the vehicle and restrained from displacement in all but the longitudinal impact direction. If the relative displacement of the pole in the direction of motion is very small compared to the total deformation of the vehicle (i.e., below 1 mm), the pole may still be considered rigid (i.e., not deforming). In this case, the acceleration of the pole multiplied by the mass of the pole can be assumed to be approximately equal to the impact force acting on the rigid pole. Thus, the force acting on the pole,  $F$ , can be found directly from Newton's second law,  $F=ma$ , where  $m$  is the total mass of the pole and  $a$  is the acceleration of the pole in the longitudinal direction. The second approach relies on the interface force features of DYNA3D. Interface forces can be written to a file during an analysis and then examined with the TAURUS post-processor.<sup>(54)</sup> From equilibrium considerations, the sum of interface forces on the vertical face of the pole equals the reaction force on the pole. Clearly, the sum of the interface forces should equal the pole impact force calculated in the earlier approach.

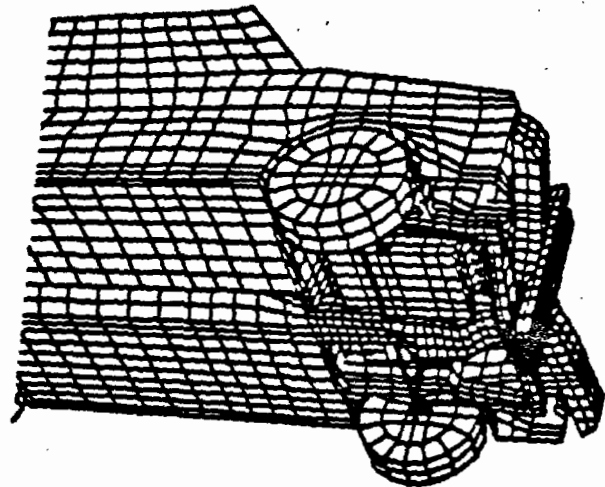
### Centerline Impact

Figure 64 shows plots of the deformed shape at various times between 0.0 and 120.0 ms during the event. To get a good view of the engine compartment, the hood was removed from the plots although the hood is present in the simulations. Figure 64 is a view from below the vehicle showing the deformed states of the engine cradle during the impact. The cradle first makes contact with the bottom of the engine block, then later buckles causing the front engine mount to deform downward resulting in pitching of the vehicle. At 1.0 ms into the impact, the vehicle bumper first makes contact with the rigid pole. At this point, the only part of the vehicle resisting the impact is the bumper. At about 20.0 ms into the impact, the rigid pole first makes contact with the lower core support and the bumper contacts the radiator. At 40.0 ms, the engine cradle starts to buckle and the back face of the evaporator core makes contact with the front face of the engine block, crushing the front engine mount between the radiator face and the engine block. The acceleration continues to decrease until 70.0 ms, when the back engine mount yields and the engine block makes contact with the firewall. During this time, the evaporator core, radiator, bumper, lower core support, and pole are all in contact with the engine block, and all components in the engine compartment including the firewall are involved in the impact. Kinetic energy of impact has been transferred to plastic strain energy and subsequently into heat energy through the buckling and local deformation of the engine cradle, engine mounts, frame horns, bumper, radiator, and fenders. At 90.0 ms, most of the kinetic energy in the system has been expended and the vehicle begins to rebound from the rigid pole because of residual elastic strain energy stored in the deformed parts.

$t = 0 \text{ ms.}$



$t = 20 \text{ ms.}$



$t = 40 \text{ ms.}$

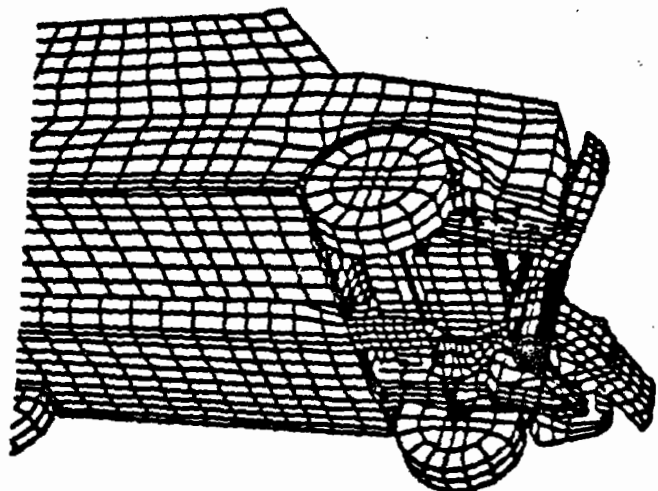
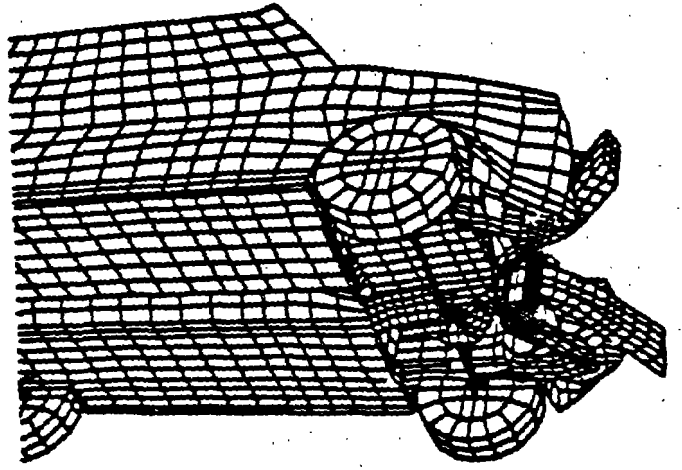
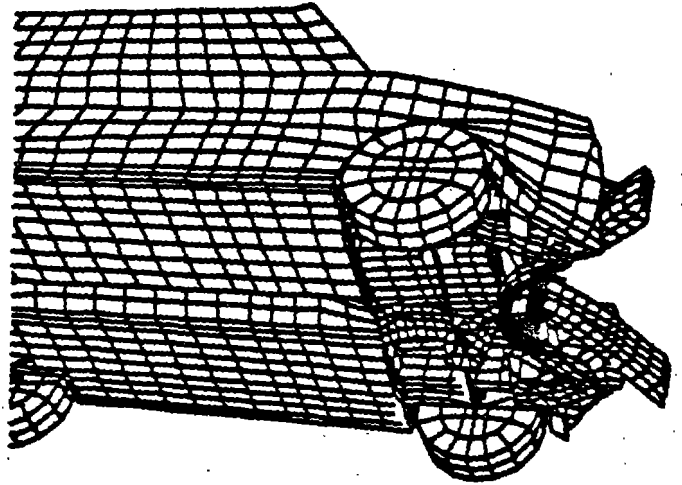


Figure 64. Festiva deformation from center pole impact. 0 to 120 ms.

$t = 60 \text{ ms.}$



$t = 80 \text{ ms.}$



$t = 120 \text{ ms.}$

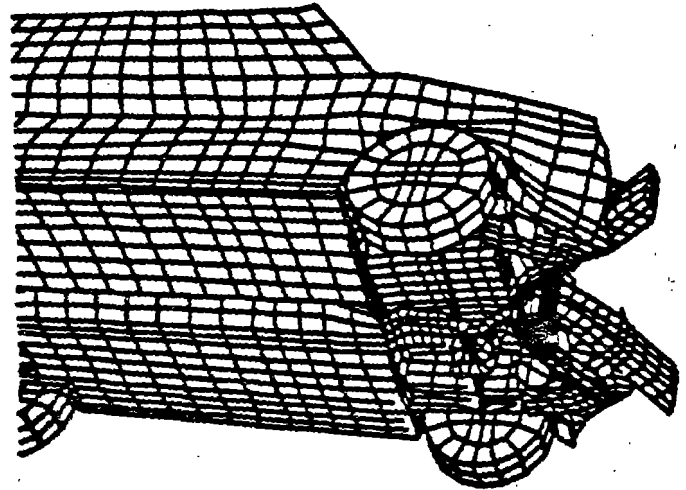


Figure 64. Festiva deformation from center pole impact, 0 to 120 ms. (continued)



The centerline impact simulation results were compared with actual full-scale crash test results. Crash test accelerations were collected, and velocities and displacements were calculated at the c.g. of the vehicle. During the test, impact forces were also collected at the rigid pole. Since the c.g. may not necessarily coincide with a specific node, the average result of several nodes on a box around the vicinity of the c.g. of the model were gathered for time history plots of the simulated vehicle. The test data used for the comparisons were obtained from tests performed at the FOIL between 1992 and 1993.

Figure 65 is the plot of the acceleration in g's (gravity) versus time for full-scale crash tests 91F049, 92F032, 92F033, and the simulation.<sup>(55)</sup> All three tests were performed with identical vehicles and impact conditions.<sup>(51)</sup> The simulation results generally corresponded reasonably well with the three tests. The initial stages of the impact were very noisy as evidenced by the fluctuations in the accelerations of the three tests. The peak acceleration from the simulation (35 g's) was within 5 percent of the average peak acceleration reported in the three tests. Averaging the three test accelerations dampens the noise in the earlier part of the event and removes the variability between tests. The shape of the simulation curve agrees reasonably well with that of the average acceleration. The first peak, on figure 65, at 20.0 ms corresponds to the time when the bumper, radiator, and lower core support first compress together in contact with the rigid pole (see figure 64 for the deformed shape). During the impact, very little deformation takes place in the engine compartment. The second peak occurs, at around 40.0 ms into the event, when the evaporator core first makes contact with the engine block. The next peak, at about 70.0 ms, corresponds to the time when contact is first made between the engine and the firewall, as shown in figure 64. At this point, the vehicle starts to reverse direction and begins to move away from the pole.

The whole impact can be divided into three stages. The first stage was the beginning of the impact to the time when the bumper contacted the radiator and lower core support. This part was referred to as the external impact stage because very little deformation took place in the engine compartment. The component most deformed in the impact at this point (the bumper) was external to the vehicle. The second stage was referred to as the internal impact stage because most of the components involved in the impact at this point were internal to the vehicle (located in the engine compartment) as shown in figure 64. The third stage, termed the rebound stage, described the event from the end of the internal stage, when the vehicle begins to recoil to the time when the vehicle comes to rest.

The displacement curves of the test and simulation agree very well until the rebound occurs. The maximum displacement of the event is within 8 percent of those recorded in the test. The displacement curve is linear during the initial stages of impact. The maximum displacement occurs at approximately the same time as the peak acceleration was reached and then begins to recoil.

There is reasonable agreement between the simulation and test results. The variations in the curves toward the end of the event maybe caused by possible factors. For instance, in the actual test, the weight of the vehicle and the attendant friction between the tires and the ground provides resistance to the motion of the vehicle during the rebound. Whereas, for the simulation, gravity is not applied which results in no resisting force on the FE model during its rebounding phase.

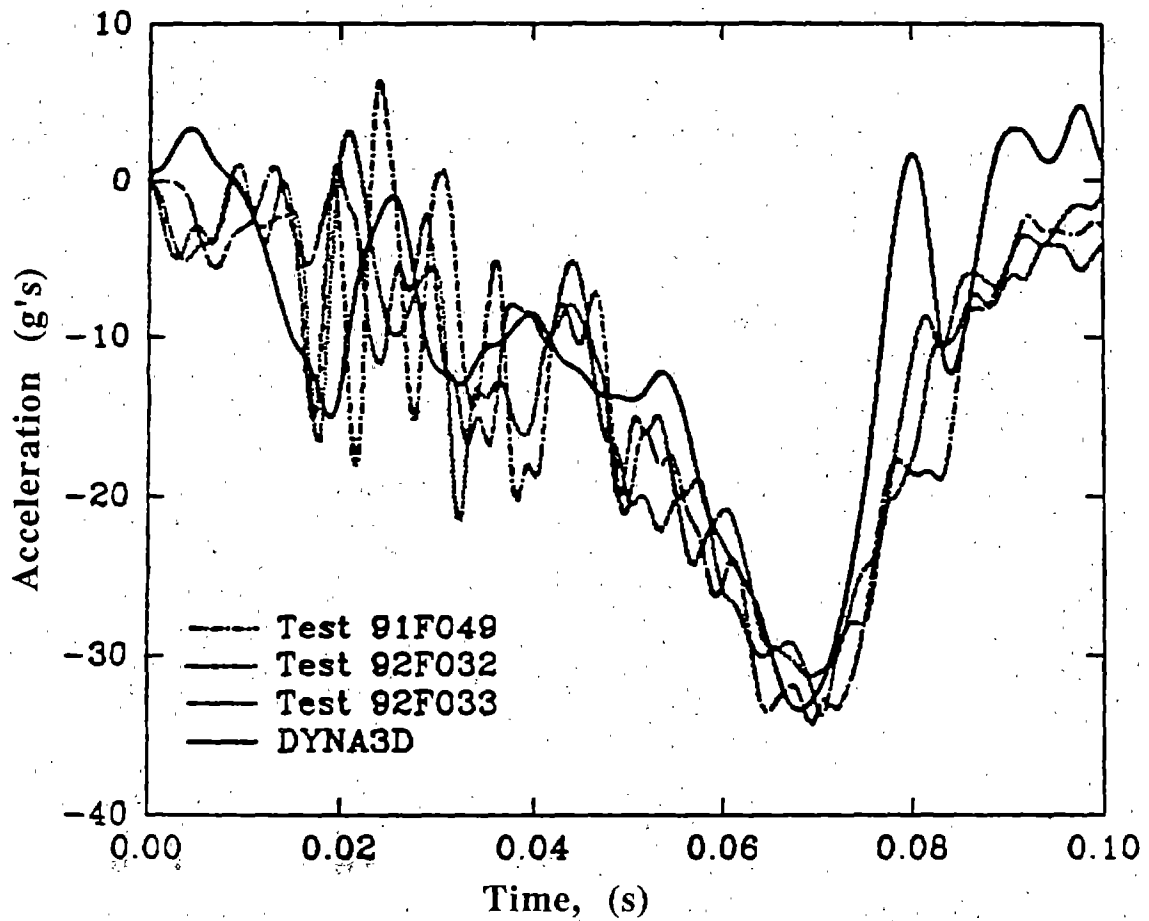


Figure 65. Accelerations at c.g. of vehicle.

Figure 66 is a plot of the resultant force on the rigid pole versus time for the simulation and tests. The area under the curve is the total impulse of the event. The test results are from load cell readings. The force on the rigid pole for the simulation was obtained by multiplying the acceleration of the rigid pole by the mass of the pole. The maximum simulated pole force is about 220 kN which is about 15 percent higher than that obtained from the test.

The first sharp peak force in figure 66 (at approximately 20 ms) is coincident with initial contact with the edge of the hood. This impact causes an increase in the forces applied to the pole, but stabilizes within a short time. The second sharp peak (at approximately 40 ms) is coincident with the impact with the front face of the engine. From the plot, one observes that the pole force builds up very fast, remains at or near the peak over a period of time, then decreases first rapidly and then gradually towards the end of the event.

The increase in kinetic energy of the simulated vehicle during the initial stages of the event may be caused by the initial pitching motion of the vehicle. The vertical location of the accelerometers in the test vehicles is not accurately known and, thus, the vertical location in the simulated vehicle is the best approximation possible. It is reasonable to suspect that the accelerometer location in the simulated vehicle may have been slightly higher than the actual test vehicle.

One observation is that the maximum longitudinal work done on both the test and simulated vehicles, is approximately 96 percent of the initial kinetic energy at impact. This tends to indicate that little yawing took place in the vehicle. The longitudinal changes in velocities, kinetic energy, impulse transferred, and the longitudinal work done on the vehicle at rebound and at the end of impact are shown in table 10. The changes in velocities, kinetic energy, impulse transferred, and work done on the vehicle agreed well up until the rebound (70 ms). The changes in velocities, kinetic energy, impulse transferred, and work done were lower for the FE simulation than for the tests.

### **Left-of-centerline and right-of-centerline impacts**

No full-scale test was available for comparison study. However, results of accelerations, displacements, velocities, and rigid pole forces were shown to (a) demonstrate the reliability of the model in simulating another impact scenario; (b) serve as a guide for designing the full-scale test; and (c) provide simulated data for comparison studies should the full-scale test become available.

### **Summary and Conclusions**

Figures 67 and 68 show plots of the acceleration, displacement versus rigid pole force for all three simulated impact cases. The peak accelerations and rigid pole forces were highest in the left-of-center (strong side) impact and smallest in the right-of-center (weak side) impact. The forces build up and decrease rapidly in both the centerline and left-of-center impacts but tend to maintain a constant value over a much longer period of time in the right-of-center impact. The displacements were, however, highest in the centerline impact and smallest in the left-of-center impact. Table 11 is a summary of the simulation and test results. The peak acceleration in all three impact cases together with the time

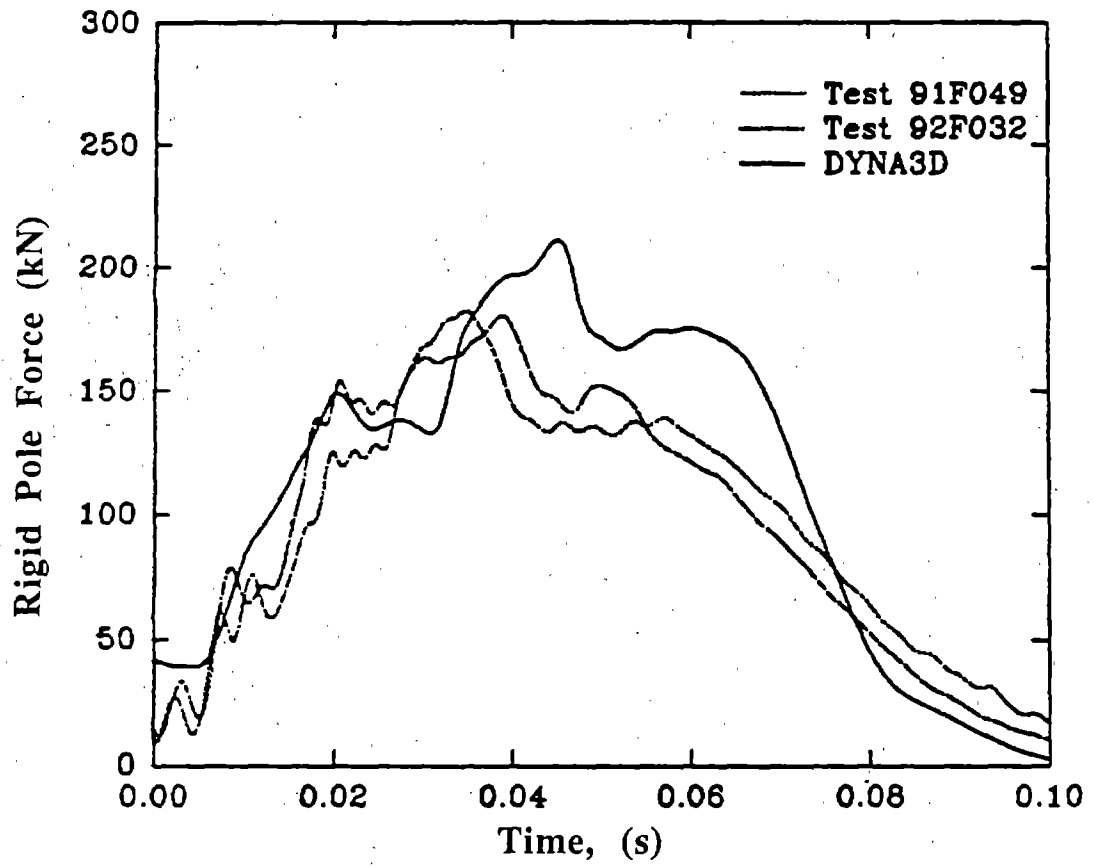


Figure 66. Rigid pole force.

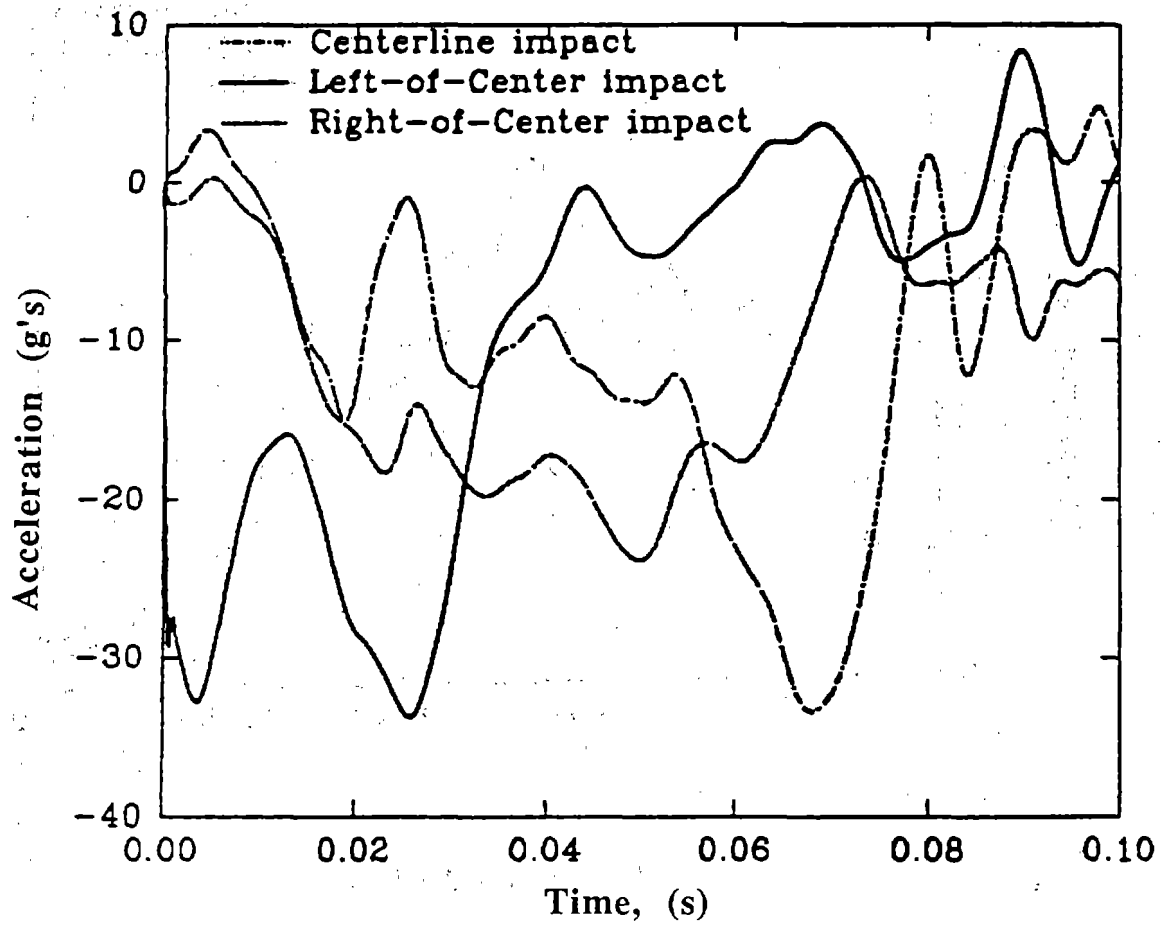


Figure 67. Acceleration at c.g. for all three simulations.

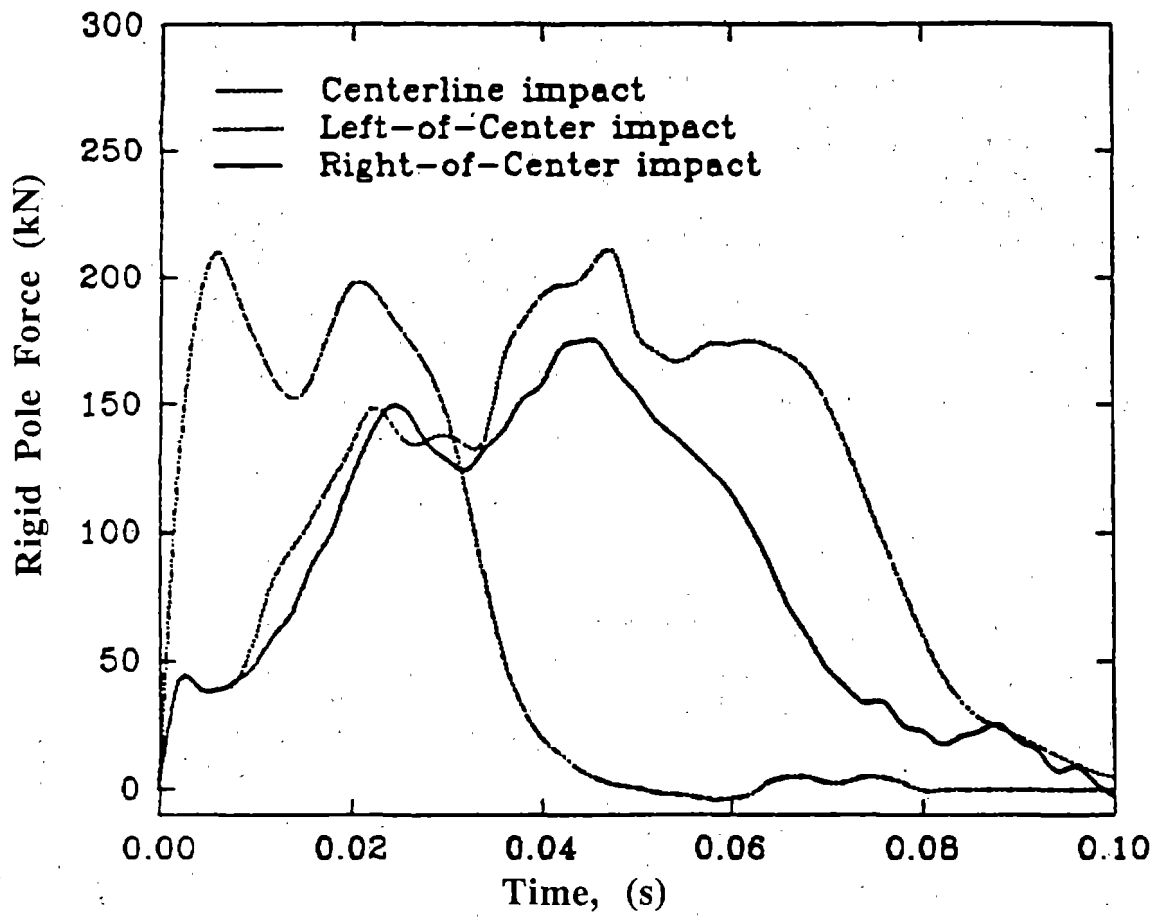


Figure 68. Rigid pole forces for all three simulations.

when these peaks occurred are shown in the table. Also shown in this table are the maximum displacements at the c.g. of the vehicle and peak rigid pole forces. Simulation performance of the three impact cases on the Risc 6000/370 are shown in table 12.

This simplified model was found to be computationally efficient, reliable, and suitable for the rigid-pole impact test. Peak values and the shape of the accelerations, displacements, and force curves agreed well with test data. Peak values were found to correspond to unique events in the impact that were clearly identifiable. This model can be useful in providing better insight into the behavior and response of vehicles during frontal impacts into roadside hardware.

The location of the engine block, modeling of the engine mounts, and the way the engine block was supported by the engine mounts were found to play a crucial role in the response of the vehicle. The use of shell elements to model the engine mounts was found to be the most reliable. Beam and truss elements were tried and discarded because they produced unsatisfactory results. Proper modeling of the engine mounts is a topic which deserves much more thought and effort.

One of the deficiencies of this study was that no attempt was made to properly match the mass moments of inertia with those of the actual vehicle. These inertial properties tend to be significant in impact scenarios with large rolling, pitching, and yawing.

During the rebound of the vehicle away from the rigid pole, the velocity could be better correlated during the rebound phase of the curve if the effect of gravity were included.

Table 10. Summary of centerline impact results.

	longitudinal change in velocity (m/s)	longitudinal change in kinetic energy (kJ)	longitudinal work done (kJ)	longitudinal impulse transferred (kN-s)
	time = 70 minutes			
Simulation	8.9	32.65	32.50	6.33
Test 91F049	9.0	32.65	33.10	6.53
Test 91F032	8.9	32.65	32.36	6.45
Test 91F033	8.9	32.65	32.36	7.00
Percent difference	0.40%	0.0%	0.4%	5.0%

Table 10. Summary of centerline impact results. (continued)

	time = 100 ms			
Simulation	9.6	32.65	32.50	8.07
Test 91F049	12.5	27.40	30.0	10.17
Test 91F032	12.3	27.40	30.0	9.97
Test 91F033	12.3	27.40	29.0	9.99
Percentage difference	22.4%	18.3%	9.5%	19.7%

Table 11. Summary of results.

	Acceleration	Displacement	Time of peak	Max. pole
Centerline impact				
DYNA3D	35.0	450.0	70.0	210.0
Test 91F049	33.5	455.0	70.0	170.0
Test 92F032	33.0	440.0	70.0	170.0
Test 92F033	31.5	430.0	69.0	--
Left of center	36.0	165.0	26.0	210.0
Right of center	23.0	370.0	50.0	170.0

Table 12. Simulation performance.

<u>Number of elements</u>		Hardware:	Risc 6000/370
Beams	60	Simulated time:	120 ms
Shells	2898		
Solids	633		
<u>Contact surfaces</u>		<u>Type of impact</u>	<u>CPU time</u>
Vehicle-pole	1	Centerline impact	12.2 h
Vehicle-Vehicle	27	Left-of-center impact	12.2 h
		Right-of-center impact	10.2 h



## Section 5. Breakaway cable terminal model

### Introduction

The breakaway cable terminal (BCT) was developed in the 1970's to address the dramatically poor performance of blunt-end and turned-down end W-beam guardrail end treatments. The BCT, shown in figure 69, consists of two 1,905-mm sections of a parabolically flared guardrail with two breakaway posts and a wrap-around nose section. The first full-scale crash tests of BCT's were performed as part of an NCHRP project to identify new and innovative W-beam terminal concepts.<sup>(56)</sup> The following decade resulted in many improvements in the BCT design that made it a more attractive system from both a crashworthiness and maintenance point of view. (See references 57,58,59,60,61, and 62.) All of this early testing used the 2,000-kg and 930-kg passenger cars recommended in the then current crash testing specifications.<sup>(63,64)</sup>

The relatively low cost of the BCT and good crash test results reported in the NCHRP projects resulted in the wide-spread use of the BCT in the United States. In the late 1970s, more than 100,000 installations were in place and tens of thousands have been installed each year since.<sup>(65)</sup> Just as the BCT's became widely accepted, researchers began to observe performance problems in the field when BCT were struck by a new generation of smaller passenger vehicles.<sup>(66,67)</sup> The eccentric loader BCT (ELT) and more recently the modified eccentric loader BCT (MELT) were developed in an attempt to improve the performance of BCT's with small cars. (See references 65, 68, 69, and 70.) While these devices succeeded in improving the crash test performance, a system with the simplicity and cost effectiveness of the BCT and improved crashworthiness still eludes the highway safety community.

Computer simulation programs for collision analysis of roadside safety hardware that were used in the past were not well suited to investigating end-on impacts with the BCT and other terminals. Programs like Barrier VII were only two dimensional and had only crude modeling capabilities.<sup>(71)</sup> Other programs like NARD and GUARD used assumptions in their formulations that precluded the analysis of terminals. While several new variations on the BCT have been developed during the past decade, further performance improvements are still being sought. The early stages of a nonlinear FEA of small vehicles in impacts with BCT's are summarized. An FE model of the BCT was developed using the INGRID preprocessor for the DYNA3D FEA software.<sup>(30,13)</sup> The development of the model and preliminary comparisons to crash tests are presented.

### BCT Model

There are several variations of the BCT: the breakaway wood post in a concrete footing BCT; the steel slip-base post BCT, the breakaway wood post in a steel foundation tube, as well as the more recent eccentric loader and modified eccentric loader variations. The system discussed in this paper is the breakaway wood-post in steel foundation tube described in NCHRP Research Results Digest No. 124.<sup>(61)</sup> This particular system was chosen because it is believed to be the most common type of BCT in use today. The geometric details of the individual BCT components were taken from a draft of Guide to Standardized Barrier Hardware.<sup>(72)</sup> Material properties were generally taken from standard engineering references; no material testing was performed to obtain material properties.

The entire 11.4-m long system was modeled using the parabolic flare specified in FHWA Technical Advisory T 5040.23.<sup>(73)</sup> A view of the whole BCT system is shown in figure 69. The last four meters of the system, shown in figure 70, are by far the most critical in terms of predicting the behavior of a small vehicle end-on impact. The BCT, shown in figure 69, is made up of the following parts:

- A buffered end section.
- A terminal connector.
- Two sections of parabolically flared W-beam guardrail.
- Two breakaway timber posts.
- Five standard wood post.
- One anchor cable.
- One anchor-cable/guardrail bracket.
- One bearing plate bolted to the anchor cable.

The buffered end section, shown in figure 71, in combination with the terminal end connector, shown in figure 72, form the nose of the BCT. Material properties for the terminal connector and buffer section were obtained from vendor compliance reports and from AASHTO material specification M 180-89.<sup>(74)</sup> An elastic-plastic material model (DYNA3D material type 3) was used for the buffer section and terminal connector. Table 13 shows the material properties used in the simulation. The W-beam guardrail was modeled as a seven-segment cross-section, shown in figure 73, with the mechanical characteristics shown in table 14. The geometry was discretized so that the total depth, total width, moments of inertia, and radii of gyration were exactly the same as an actual W-beam. Table 15 shows the material properties of typical W-beam material as delivered from manufacturers and specified in AASHTO M 180-89 along with the particular material properties used in the FE model.<sup>(75)</sup>

The first two posts in the BCT are 150- by 190-mm timber posts with a 60-mm diameter breakaway hole. Several assumptions were made in modeling the breakaway posts. First, the base of the post was assumed to be fixed at the ground line. This is a reasonable assumption since the timber post is fixed inside a steel foundation tube that has only very rarely been observed to displace in actual crash tests.

The method chosen to model the breakaway performance of the post necessitated the second assumption. Timber is a nonlinear orthotropic material with very complex material properties, including a variety of possible failure modes. A nonlinear orthotropic material model is available in DYNA3D but the material properties needed to characterize timber are not available, at least without an extensive materials testing program. Timber properties are given in table 16.

Fortunately, there are many pendulum tests of both standard 150- by 190-mm posts and BCT breakaway posts available in the roadside hardware testing literature, as shown in table 17.<sup>(75,76)</sup> The USDA Wood Handbook lists moduli of rupture, which is an upper bound measure of the ultimate strength of wood in bending, for green Douglas Firs and Southern Yellow Pines at between 45 MPa to 60 MPa.<sup>(77)</sup> The observed ultimate stresses calculated from pendulum tests agrees reasonably well with the solid values listed in the Wood Handbook. When timber posts are supported in rigid-test brackets or the BCT foundation tube, the post nearly always fails in bending; the longitudinal fibers of the timber progressively fail in tension on the impact face of the post.

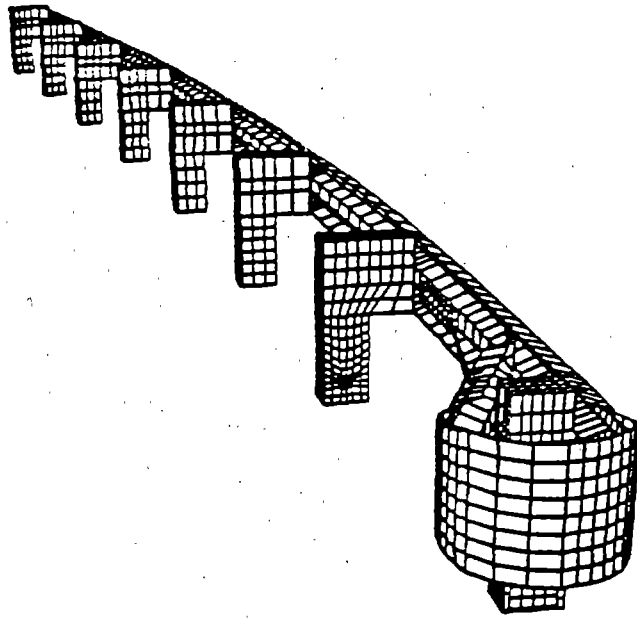


Figure 69. View of the BCT FE model.

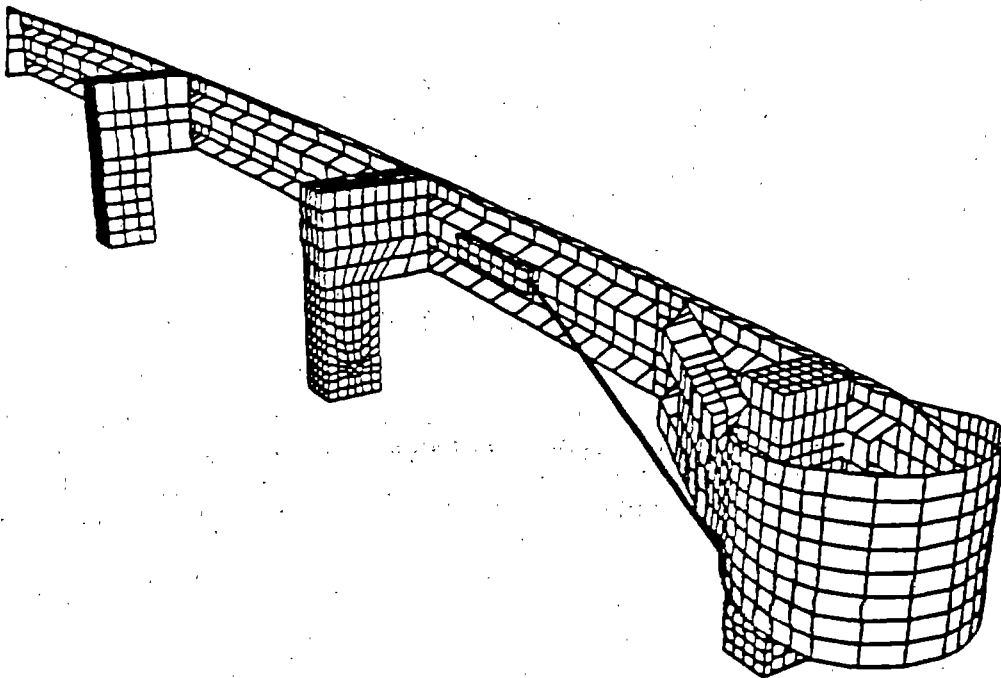


Figure 70. View of the end of the BCT model.

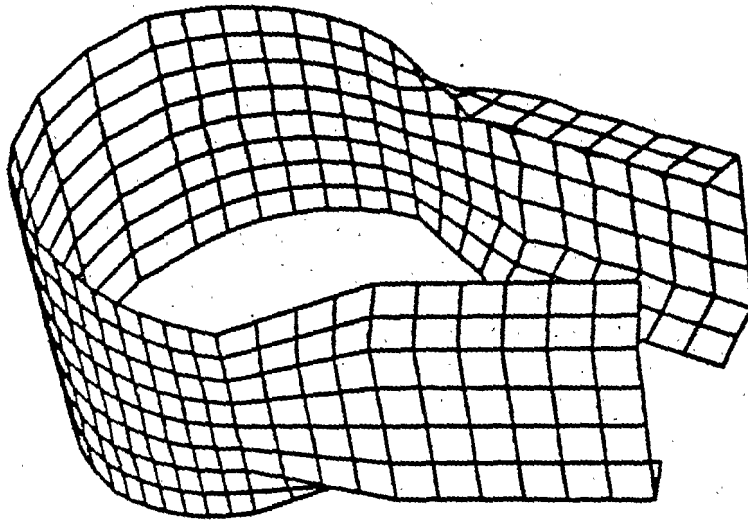


Figure 71. Buffered end section.

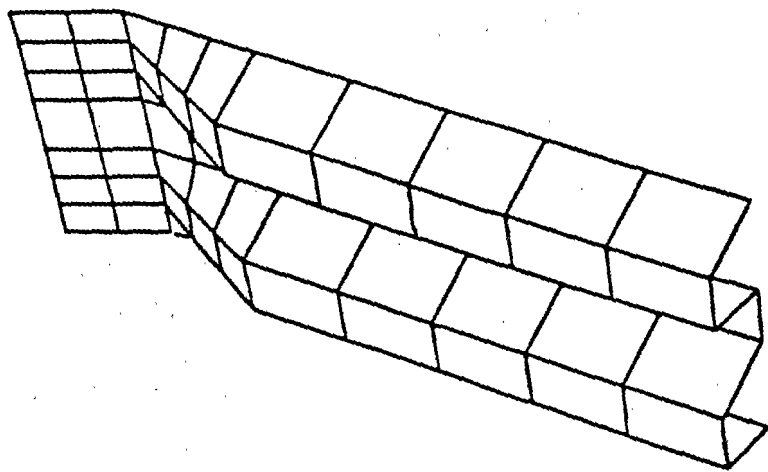


Figure 72. Terminal end connector.

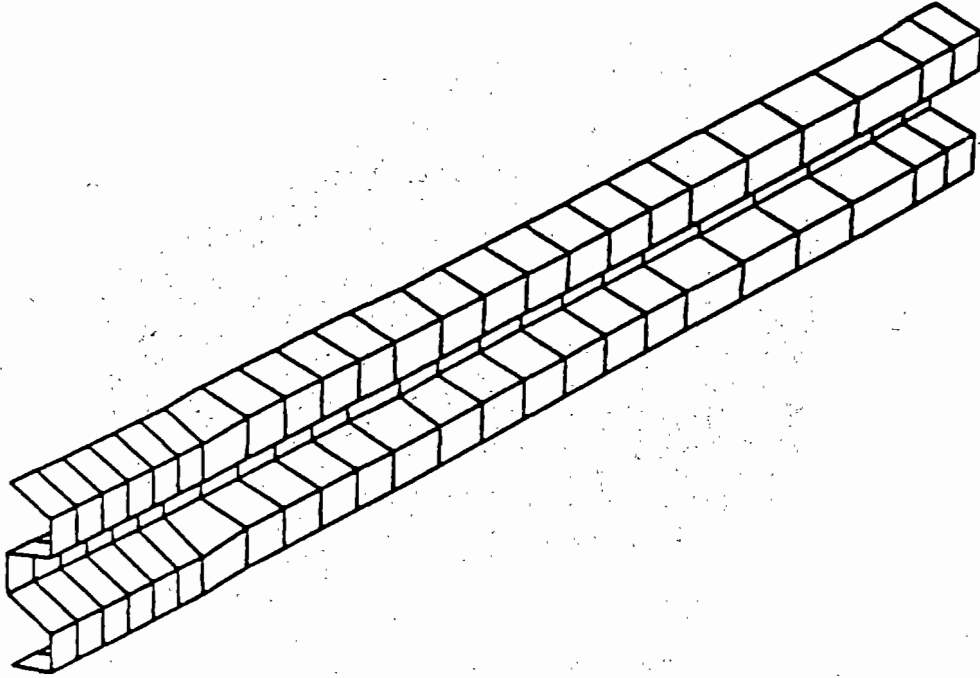


Figure 73. W-beam guardrail.

The post could have been modeled using a failing material (i.e., DYNA3D material 24). The advantage to this approach is that the analyst need not know *a priori* where the failure occurs. Unfortunately, the TAURUS post-processor for DYNA3D contains an error that prevents post-processing output files that include both material type 24 and beam elements.<sup>(54)</sup> Since it was imperative to use beam elements for the cables, it was not possible to use a failing material for the post. This is a limitation that the authors hope to solve by using the GRIZ post processor.<sup>(78)</sup>

Instead of using a failing material, the post was divided into two parts: the part above the center of the weakening hole and the part below (i.e., the post stub). The two were connected using a tied-with-breaking contact surface (contact type 9). A normal and shear stress may be specified where nodes tied on the surface will break apart. The normal stress for breaking was set to 40 MPa. The shear stress was set to a very high value since timber posts do not fail in this mode.

The remaining posts are unmodified 150- by 190-mm timber posts embedded directly in soil. Only the third post is directly involved in the impact and since this occurs very late in the impact event, these posts are also assumed to be fixed at their bases.

The cable anchor assembly is an important feature of the BCT design that provides anchorage in down-stream impacts. Without the cable anchor, the tensile forces in the guardrail during a down-stream impact would cause a large cantilever bending moment on the weakened breakaway posts that could cause failure. The cable anchor transfers this tensile load directly to the foundation through a cable that is secured to the guardrail with the cable-anchor bracket. The cable fits through the breakaway hole in the post and attaches to a bearing plate on the front of the BCT post. During an end-on impact like the one considered in this report, the cable is released as soon as the post breaks. The cable was modeled as a linear elastic material with a modulus of elasticity of 90 GPa based on the published properties of 19-mm 6 by 19 strand internal-wire-rope-core (IWRC) cable at less than 20 percent of its loading.<sup>(79)</sup> DYNA3D truss elements can transmit both tensile and compressive axial loads whereas real cables, of course, can only resist tensile loads. The cable was modeled as a series of 16 truss elements so that the cable would resist tensile forces properly but would buckle if loaded in compression.

Unfortunately, the cable reinforces the parabolically bent section of the guardrail before the breakaway post failing with the effect of increasing the buckling strength of the guardrail when hit end-on. The guardrail cable-anchor bracket also reinforces the guardrail locally inhibiting buckling near the second BCT post. The anchor details, while designed for other impact scenarios, have important and possibly negative effects on the BCT performance in end-on impacts.

## Simulation Results

Figures 74, 75, and 76 show plots of the collision simulation. As shown in figure 74, the vehicle contacts the nose at time zero and quickly collapses the nose section until the vehicle bumper contacts the first breakaway timber post at about 27 ms. Serious vehicle damage begins to accumulate in the process of breaking the first post. After the post has fractured and the W-beam rail begins to buckle, the vehicle continues intruding into the BCT, rolling the collapsed nose and crumpled W-beam rail in front of and under the front

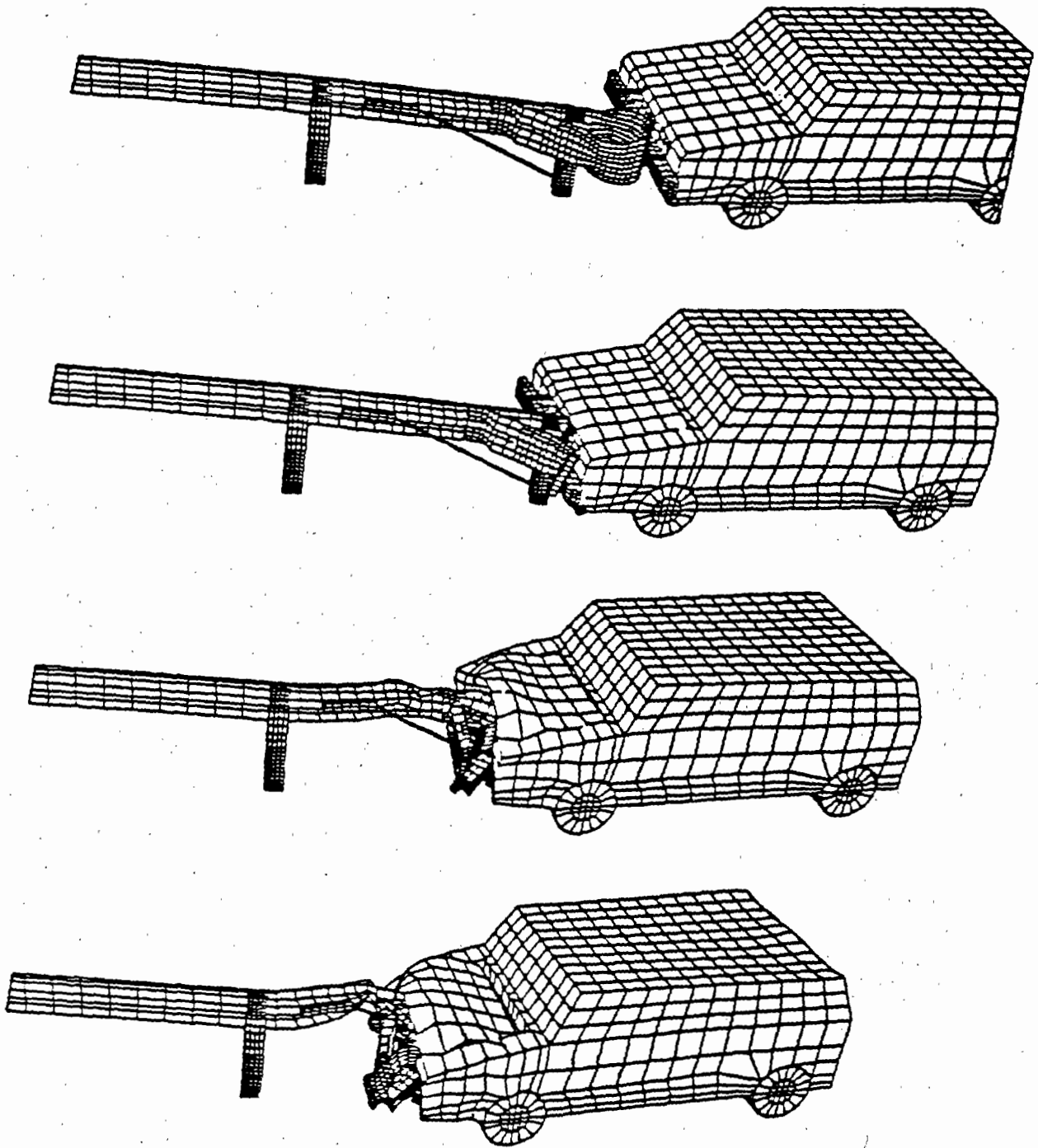


Figure 74. Simulation of a BCT impact.

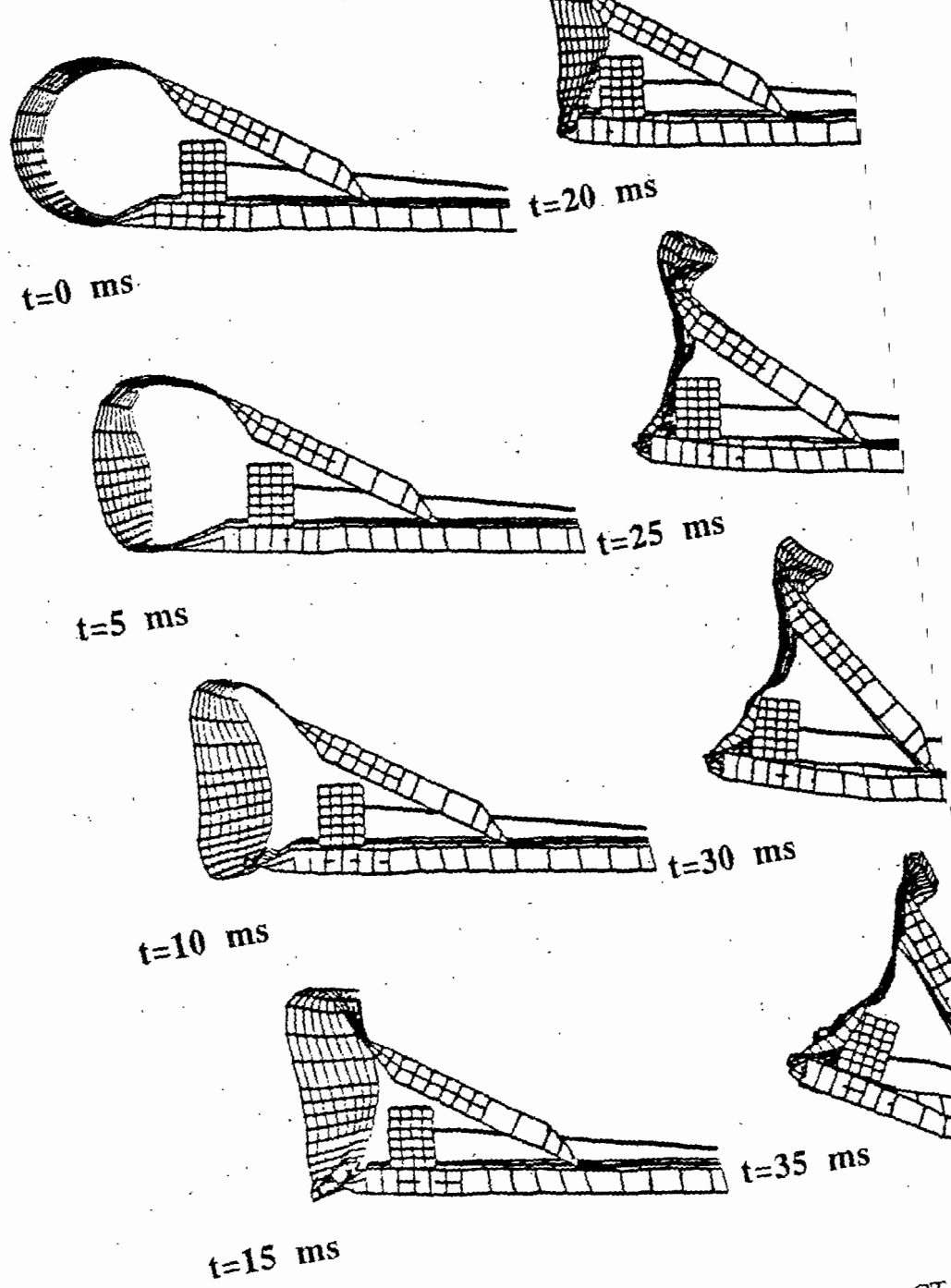


Figure 75. Simulation of the collapse of the BCT



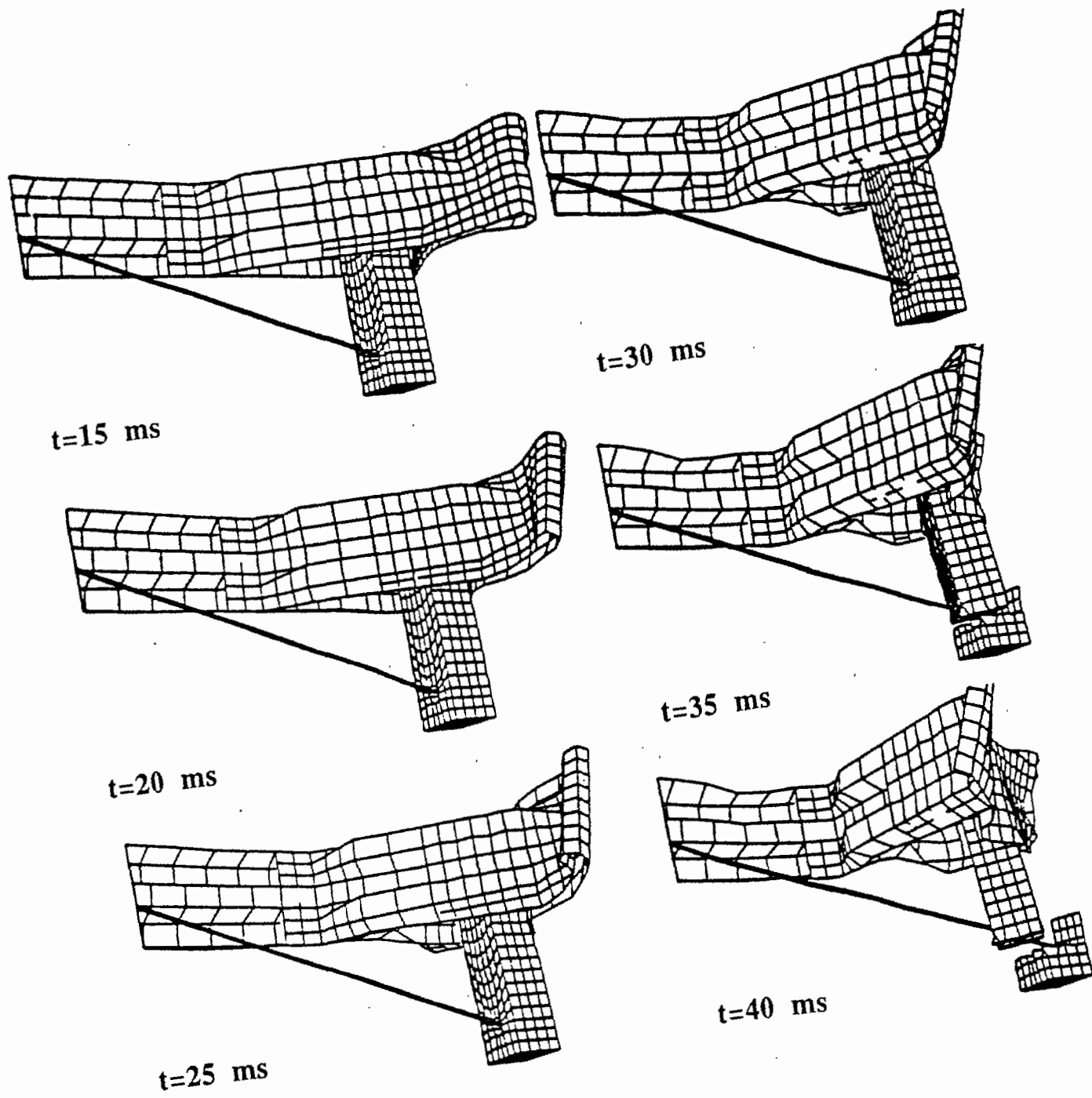


Figure 76. Fracture of the breakaway timber post.

of the vehicle. The bumper, core support, fenders, and frame horns of the vehicle are all heavily damaged by 75 ms. The vehicle continues forward until it strikes the second breakaway post at about 140 ms. The simulation was stopped at this point because inappropriate element interpenetrations were observed between the vehicle and barrier. Several contact surfaces on the barrier and vehicle need to be extended to allow contact at the second post.

Figure 75 shows a sequence of deformation plots of the collapse of the nose of BCT (the vehicle is not shown for clarity). The buffer section is collapsed during the first 20 ms of the event causing the vehicle to decelerate at a relatively constant 4 g's as shown in the acceleration history in figure 77. The vehicle becomes fully engaged with the post between 20 and 30 ms. At this point, the terminal connector begins to rotate, introducing a moment into the guardrail beam. The portion of the W-beam rail lapped into the buffer section and connected to the post remains very stiff throughout the event. At 27 ms, the post breaks and the cable begins to go slack. The vehicle rides over the broken post stub and continues buckling the W-beam rail until the second breakaway post is reached.

Figure 76 shows deformation plots of the breakaway timber post (the vehicle is again not shown for clarity). The buffer plate is fully collapsed against the post at 20 ms. The first fracture in the post appears at 25 ms and expands over the next 10 ms until the post is completely fractured at 35 ms. The vehicle then pushes the broken post and collapsed nose elements in front of it as it continues on to the second breakaway post.

Table 18 shows a variety of statistics indicative of the simulation performance. These are included as a guide to the amount of computational difficulty in simulating this type of collision.

### **Comparison to Crash Test**

The BCT literature was searched for a small-car test of the wood-post-in-foundation-tube BCT that corresponded to NCHRP Report 350 Test 30 conditions. Test WBCT-2 was performed at Southwest Research Institute in 1980.<sup>(65)</sup>

Figure 77 shows a comparison of the acceleration in the x direction at the vehicle c.g. between the test and the simulation. The test data was obtained by manually scaling values from the printed acceleration plot at 2.5 ms intervals. The simulation data is the average acceleration of the accelerometer box modeled in the vehicle. The simulation data was gathered at 2,000 Hz and filtered at 300 Hz. The accelerations of the vehicle in the crash test are measured in the local coordinate reference frame whereas the simulation data are in the global reference frame. For a more meaningful comparison, one should be converted into the other; but they are shown in figure 77 since a program for solving the coupled equations of motion was not immediately available.

The first 15 ms of the event is dominated by relatively low (4 g) decelerations required to collapse the buffer section. The decelerations increase rapidly when the bumper first contacts the W-beam rail that projects in front of the breakaway post (see figure 75). The projection is very stiff since the buffer section and the W-beam are spliced at this location and the rail is attached to the post just behind this section. The first major peak represents

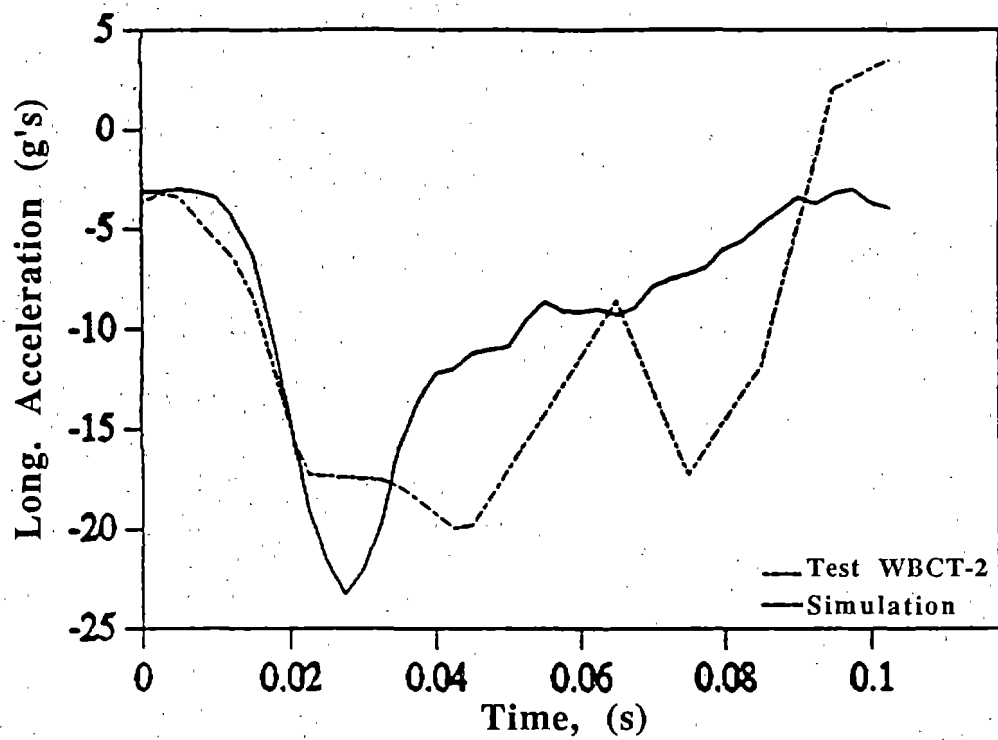


Figure 77. Acceleration of the c.g. - test and simulation.

the decelerations experienced by the vehicle in fracturing the first BCT post. The bumper does not directly contact the post until about 22 ms, but the vehicle contact with the projecting W-beam transmits large bending moments to the post. The major peak represents the failure of the post at 27 ms. The test curve does not reach as high a peak and the peak is spread out more than the simulation. This may indicate that the material is not as brittle as was assumed in the material model.

The test shows another peak at about 90 ms that is absent from the simulation. This peak does not represent the interaction with the second BCT post since that event does not occur until 140 ms. The second peak in the test is probably indicative of the W-beam rail buckling just in front of the second post, another area where the simulation should be carefully rechecked.

While there are numerous improvements needed in the model to address these and other problems, the simulation did demonstrate that a reasonable model could be produced that contained all the correct phenomena. The challenge remaining is to determine which parts of the model control the responses. Finding the answers to these questions represents the real value of simulation since the analyst will have learned what features of the hardware effected the response. This knowledge about the system's behavior can then be used to formulate better designs.

There are several difficulties in comparing this simulation to test WBCT-2. First the simulation used an 820C vehicle modeled on a 1989 Ford Festiva whereas the test used a 1979 Honda Civic.<sup>(52)</sup> The exact position of the accelerometers in the tests is not known. They are reported to be near the c.g., but the pitch and yaw rotations that occur in this simulation and test make a more precise location necessary for proper comparison. There also appeared to be an impact sensing anomaly with the test results that, given the intervening 12 years, is not possible to resolve. These uncertainties make comparing the test and simulation dubious. For the above reasons, a new test of this system is being planned.

### **Future Activities**

While the simulation discussed is not complete, it does demonstrate that useful and reliable results can be obtained using the DYNA3D FE approach. A variety of activities related to this model of the BCT is planned, including:

- Performing another full-scale tests that corresponds more closely to the vehicle, test conditions, instrumentation points, and data analysis techniques assumed in the simulation.
- When the current model is validated in comparison to full-scale tests, variations of the BCT like the MELT and ELT will be modeled and compared to tests in the literature.
- New design concepts will be explored using the BCT model to attempt to find simple and effective retrofits for the BCT. Promising alternatives may be crash tested.

There are several advantages to using simulation in analyzing and designing roadside safety hardware, especially for difficult impact situations like the end-on impact of guardrail terminals.

1. FE models of a roadside hardware will allow researchers and designers to explore a wider range of retrofit options in greater detail than would be possible using crash tests.
2. FE simulations provide details on the stress and strain histories of vehicle and barrier components that are not observable in a test. This detailed knowledge is useful for the engineer in formulating effective and creative modifications.
3. Although the time and cost to build an FE model are easily as expensive as one or two full-scale crash tests, the ability to reuse the simulation for a multitude of parametric studies make simulation a cost effective design and analysis tool.

Table 13. Buffer section and terminal connector material properties.

Mechanical Properties:		
Yield Stress	263	MPa
Ultimate Stress	375	MPa
Elongation	34.3	%
AASHTO Specification	M-180 (21)	
Source: Vendor test report		
DYNA3D Properties:		
Material Type	3	
Element Type	BT	shell
Mod. of Elasticity	200	GPa
Yield Stress	263	MPa
Tangent Modulus	200	MPa
Poisson's Ratio	0.33	
Integration Points	3	
Hardening Type	Kinematic	
Density	7,850	kg/m <sup>3</sup>

Table 14. Cross-section properties of W-beam guardrail.

	Actual Shape	Discretized Shape	Percent Difference
Depth (mm)	81	81	0
Width (mm)	214	214	0
Area (mm <sup>2</sup> )	1,290	1,200	-7
I <sub>weak</sub> (mm <sup>4</sup> )	1.00 (10) <sup>6</sup>	1.03 (10) <sup>6</sup>	+3
k (mm)	27.9	29.3	+5

Table 15. Guardrail material properties.

Mechanical Properties:		
Yield Stress	390	MPa
Ultimate Stress	556	MPa
Elongation	25.5	%
AASHTO Specification	M-180 (21)	
Source: Vendor test report		
DYNA3D Properties:		
Material Type	3	
Element Type	BT	shell
Mod. of Elasticity	200	GPa
Yield Stress	390	MPa
Tangent Modulus	200	MPa
Poisson's Ratio	0.33	
Integration Points	3	
Hardening Type	Kinematic	
Density	7,850	kg/m <sup>3</sup>

Table 16. Timber material properties.

Mechanical Properties:		
Ult. Tensile Stress	375	MPa
Source: Vendor test report		
DYNA3D Properties:		
Material Type	3	
Element Type	BT	shell
Mod. of Elasticity	200	GPa
Poisson's Ratio	0.33	
Density	7,850	kg/m <sup>3</sup>
Interface Properties:		
Normal Stress	70	MPa
Shear Stress	2,000	MPa

Table 17. Ultimate failure stress of timber in pendulum tests.

Avg. Bending	Standard Deviation		
Failure Stress		Samples	Source
(MPa)	(MPa)		
45.42	7.56	8	(22)
35.96	9.07	7	(23)

Table 18. Simulation characteristics.

No. of Elements	
(Vehicle and Barrier)	
Shell	2851
Solids	1833
Beams	16
Contact Surfaces	
Vehicle-Barrier	1
Vehicle-Barrier	12
Vehicle-Barrier	15
Vehicle-Barrier-Ground	1
Performance	
Hardware	Risc 6000/370
Simulated time	200 ms
CPU time	24 hrs
Performance	8 ms/hr



## CHAPTER 6: DISCUSSION

### Training and Assistance

LLNL provided training sessions onsite at FHWA in the use of the basic LLNL codes INGRID, DYNA, and TAURUS. The training consisted of lecture, training course note package, and hands-on sessions. Three separate sessions, each lasting a week provided a different LLNL analyst's perspective on learning and using the LLNL codes. Personnel from FHWA, NHTSA, National Crash Analysis Center (NCAC), and universities attended. The attendees reported that the training sessions were very useful in learning the basics of FE model formulation, DYNA analysis, and post-processing.

LLNL has assisted in the delivery of the DYNA code package to university collaborators associated with FHWA. LLNL offered assistance to the FHWA collaborators. One collaborator was given guidance on the use of material model 24 and DYNA3D related meshing and material characterization problems. Another collaborator was offered help on refinement of a MDB mesh and provided with test specifications for honeycomb materials.

### Safety Research Benefits

After two years of effort, there is still a need for further roadside safety research. Safety research has reduced the fatalities and injuries experienced on the roadside, as well as accident costs, and have protected the public's investment in roadside safety hardware.

The goal of reducing the number, severity, and cost of highway accidents is shared by both FHWA and NHTSA. NHTSA has concentrated on vehicle-to-vehicle collisions and occupant protection technology. FHWA has addressed single-vehicle roadside accidents which accounted for 1.4 million accidents in 1992, representing more than 20 percent of all motor vehicle accidents.<sup>(80)</sup> FHWA and NHTSA share the responsibility for this motor vehicle accident problem. New accident types, like the interaction of wedge-shaped vehicles with roadside hardware, probably cannot be improved without a joint effort by both the roadside and vehicle design community.

Typical roadside hardware has a service life in excess of 20 years. Vehicles last about half as long, but automobile manufacturers can change the characteristics of the vehicle population very quickly. Vehicles are built that meet all applicable NHTSA safety standards but may not perform correctly with the majority of roadside hardware. For example, recent testing has shown that full-size pickup trucks roll over in 25 degree, 100 km/hr impacts with some strong-post W-beam guardrails. This class of vehicles is rapidly approaching 50 percent of the vehicle fleet and this barrier is the primary guardrail throughout the United States.<sup>(81)</sup> Minivans, a new vehicle, now represent about 10 percent of the vehicle population.<sup>(81)</sup> No crash tests of minivans and roadside hardware have been performed. No clear understanding exists of how such vehicles perform in the field when impacting with roadside safety hardware.

State governments have a substantial investment in hundreds of thousands of miles of longitudinal barrier along the roadway. There are no standards to ensure that this investment is not made obsolete by rapid changes in the vehicle fleet. One way to protect the public's investment in roadside safety hardware would be to require that vehicle manufacturers demonstrate acceptable interaction of new vehicles with common types of roadside safety hardware.

### **Vehicle-Barrier Interaction**

Side impacts are a problem with breakaway hardware like luminaire supports, small signs, and guardrail terminals.<sup>(82)</sup> Testing has shown that it is nearly impossible to weaken a guardrail terminal sufficiently to improve side impact performance without destroying the terminal's effectiveness in end-on impacts. Improved performance for side impacts with guardrail terminals (thought to be about 1/3 of all guardrail terminal collisions) will require improvements to the side structure of vehicles as well as better terminal design.<sup>(83)</sup>

Poor performance of pickup truck impacts with guardrails and guardrail terminals has been observed.<sup>(84)</sup> Evaluation of these tests suggests the problem may be caused by (a) the inertial and stability properties of the truck; (b) particular aspects of the suspension design that promote failure in barrier collisions; and (c) the short overhang distance between the front bumper and front wheel. This would prompt the question, "what is being tested, the hardware or the vehicle?" The recent pickup truck experience suggests that there may be similar problems with the new cab-forward passenger car designs.

The aerodynamic shaped found on the front ends of many new vehicles perform poorly in end-on impacts with terminals.<sup>(85)</sup> Terminal nose modifications have not yet significantly improved the results. There is evidence that problems exist for aerodynamically styled vehicles under-riding some types of guardrails.<sup>(86)</sup>

These few examples demonstrate that changing geometry and properties of vehicles have made barriers obsolete that performed quite well with the vehicle fleet as recently as 5 or 10 years ago.

### **Role of FEA in hardware design and testing**

In time, FEA can become an integral part of the roadside safety hardware design process. With the variety of difficult vehicle-barrier interaction problems, one can not expect to test every impact scenario. The roadside safety research cycle can be represented by design, simulation, test, implementation, and inservice evaluation. Today a researcher designs hardware and tests it, refining until either a successful design is produced or funding is consumed. Hardware is installed based on the results of these research and development tests. Inservice evaluation of hardware has not yet found its way into practice so the safety research cycle is seldom ever closed. This report demonstrates the importance and utility of analysis in the roadside hardware development cycle.

Analysis can help identify and correct problems in the complex design before testing. There are several arguments that justify the use of analytical methods in roadside safety research. Tests cannot provide enough information about the loads, accelerations, stress,

research. Tests cannot provide enough information about the loads, accelerations, stress, and strains of barrier components to develop designs based on the mechanical behavior of barrier components. Repetitive tests are expensive and not well suited to parametric analysis. It is impractical to test barriers using the full range of vehicles that should be examined. It is not possible to examine the affects of variety of test conditions like non-tracking pre-impact trajectories, side impacts, and driver braking and steering during impact. FEA can help to improve the quality of future testing by identifying the optimum location of transducers on the vehicle and hardware.

FEA provides information that can be used to modify and improve the design. Not only can simulations explain the results of tests, but they can predict the results a priori, and evaluate impact scenarios that are untestable. Initially FEA can be used to examine tests that have already been conducted. Such analysis can be used to examine the stresses and strains, accelerations and velocities, and failure mechanisms of a particular impact scenario and provide an improved understanding of the impact event. This can then be used to develop better design alternatives through parameter studies of particular design elements or variations in material properties.

Next, FEA can be used to predict the likely outcome of a full-scale crash test before the test is performed. One may be able to select the best design alternative, or identify the most critical crash test. FEA may also enable the worst-case test vehicle to be identified for a particular piece of hardware.

The final stage is to use FEA to evaluate the performance of vehicles and hardware in situations that cannot be tested. Examples include examining non-standard impact conditions like yawing before impact, braking and steering during impact, and traversing a non-level terrain before impact. This use of FEA will enable engineers to examine collisions that are impossible to test. The final result is hardware that performs more reliably under a wide range of actual conditions.

The future roadside safety environment will require roadside hardware that performs safely over a wide range of impact conditions for a wide range of vehicle types. Full-scale crash testing will never be eliminated. But it can no longer remain the primary tool for roadside safety research.

### **Simulation Codes**

FHWA, NHTSA, and LLNL have actively promoted integrating nonlinear FE technology into the roadside hardware design and evaluation process. Over the past 2 years, both success and failure have been experienced. DYNA3D and other available analysis codes can be used to solve many roadside hardware design problems. Analysts have only begun to exploit the capabilities of these codes for roadside hardware design. The near-term focus must be on increasing the number of design engineers that will use FEA to improve the design of roadside safety hardware.

## Vehicle model development

When FHWA began its effort to use DYNA3D in roadside hardware assessment, no one anticipated how difficult it would be to obtain vehicle models. Not a single vehicle model was available. The goal was to develop a model that would run on a workstation. Additional models were developed by a variety of organizations for a variety of purposes so the size, complexity, and speed vary considerably. While a high degree of complexity may be required for designing vehicles, evaluating occupant restraint systems or assessing the likelihood of occupant compartment intrusion, it is still unclear how complex a vehicle model must be to provide good results in roadside hardware simulations.

The first model developed for roadside hardware analysis was a simple model of a 1991 GM Saturn.<sup>(17)</sup> This model was based on the physical measurements of the vehicle. It was used to simulate a frontal impact with a slipbase luminaire support, a rigid wall, and a u-channel post sign support and demonstrate the utility and feasibility of using nonlinear FEA. This vehicle model was the first successful application of DYNA3D to a roadside safety hardware problem and ran on a workstation overnight.

FHWA then sponsored development of a frontal impact model of a 1981 Honda Civic, a vehicle frequently used in past crash tests. This model was developed by a firm that specializes in developing vehicle models for the automotive industry. There were numerous problems with this vehicle and extensive additional work was required before reliable results could be obtained for roadside safety applications.

The 1990 Ford Festiva, a simple model to represent a 820C vehicle, was developed at FHWA to try and obtain a vehicle model quickly that would allow researchers to focus on developing roadside hardware rather than building vehicle models. This relatively generic model was initially developed for frontal impacts into narrow objects. It was also used for frontal impacts with guardrail terminals and redirection collisions with guardrails and bridge railings.

NHTSA sponsored the development of a 1991 Ford Taurus model, also produced by an automotive crashworthiness analysis company.<sup>(87)</sup> This model has been extensively modified as it was used in a variety of new situations not foreseen when it was originally developed and has not yet been used in roadside hardware simulations. It has been used in simulations of frontal rigid wall impacts, off-set frontal vehicle-to-vehicle impacts, frontal narrow object impacts, and occupant compartment intrusion studies. Also, a version of this model is available for narrow object side impact collisions. NHTSA is continuing to sponsor the development of models for additional vehicles.

A 1994 Chevrolet C-1500 (and C-2500) pickup truck was jointly developed by NHTSA, FHWA, and George Washington University. The vehicle was disassembled, scanned, and connections were meticulously documented. The result was a large, complicated, and detailed model that is difficult to use unless one has sophisticated computing facilities and is prepared for long run times. FHWA is currently sponsoring an effort to simplify this model so that it is more useful to roadside hardware researchers using DYNA3D on typical engineering workstations.

At present, the most serious obstacle to using FE methods in designing roadside hardware is the scarcity of vehicle models. Modeling vehicles using nonlinear FEA is not in itself new. Automobile manufacturers have been making extensive use of DYNA3D or similar codes for nearly a decade for full frontal crash simulation to improve safety performance. Using this type of analysis in roadside hardware design, however, is new. Roadside hardware impact simulations must address inertial properties of the vehicle to a much more detailed degree. The roll-pitch-yaw rotations of the vehicle are a very important aspect of a roadside hardware test since these indicate the stability of the vehicle. Until very recently, there was no simulations of a vehicle in an angled impact where the rotation of the vehicle was physically reasonable. The effect of the suspension system on the kinematics of the vehicle is not generally considered in vehicle models generated by the automobile industry. Yet in roadside hardware impacts, the suspension effects can frequently be critically important. Finally, failures observed in full-scale crash tests are sometimes accompanied by relatively little vehicle damage. This illustrates that the kinematics of the vehicle are more important in roadside hardware simulations than they generally are for the full frontal automotive crash simulations. The structural crashworthiness is seldom the deciding factor in whether a full-scale test passes or fails the Report 350 evaluation criteria.

The type of vehicle barrier interaction determines the complexity of the vehicle model required. For example, the floorpan intrusion in a vehicle will require large complex models of the vehicle whereas other types of impacts such as a glancing-blow impact of a guardrail terminal, depend almost completely on inertia and kinematics so a very simple model is appropriate. Ideally, the vehicle models used by FHWA and NHTSA should be the same. There are several approaches to model development. One can develop high-order models and wait for computing hardware and software advances to reduce the computational effort. One can develop high and low-order meshes at the same time. One can develop models specifically targeted for each application. Each strategy has its advantages and disadvantages. At this stage, it is probably more important to gain experience with the existing set of vehicle models.

### **Roadside hardware design**

FHWA has sponsored a variety of efforts to model roadside safety hardware during the past several years despite the scarcity of appropriate vehicle models. The first several roadside hardware applications of DYNA3D were of small car (Saturn, Honda, Festiva) frontal impacts with a rigid pole and u-channel post. The rigid pole simulations are very useful for validating frontal impact vehicle models for narrow object impacts.

Recent poor test results of pickup trucks in impacts with several standard guardrail terminals have generated interest in simulating these types of impacts. A modified eccentric loader BCT (MELT) guardrail terminal was modeled and simulations of Report 350 Tests 3-30 and 3-32 were performed using the 820C vehicle model. The small car model was used first since there is test data available for the Test 3-30 conditions. After the model of the MELT was found to perform well in small car impacts, the Chevrolet C-1500 pickup truck model was combined with the MELT.<sup>(88)</sup> The simulation was encouraging, but the vehicle did not roll, pitch, or yaw as it should have. The actual crash test resulted in a rollover whereas there were no stability problems apparent in the simulation.

A turned-down guardrail terminal impacted by the Honda Civic model at 100 km/h<sup>(89)</sup> was performed as a part of a State-sponsored research effort to find a crashworthy retrofit for the once popular turned-down guardrail terminal. This research was the first where nonlinear FEA was used to examine a variety of design options that were then tested in a full-scale crash test.

These examples serve to illustrate the utility of FEA for safety research. The recent simulation efforts have demonstrated steady progress from relatively simple impacts to quite complicated, realistic impact scenarios.

## CHAPTER 7: CONCLUSIONS AND RECOMMENDATIONS

A great deal of progress has been achieved during the past several years in integrating nonlinear FEA into the enhancement of occupant safety and the roadside hardware design process. The following thoughts are based on the collective experience of the many individuals involved in the Pre-VISTA project.

Since completing the DYNA/MADYMO link, a new version of MADYMO has been released that has restart capability. For simulation of complex vehicle and occupant interaction, this is a very desirable feature. Without a restart capability, one has to depend on the problem running to completion without encountering any number of factors that could end the computation before completion. If the problem does not complete, one must start over again at time zero. Our link was completed well before the new release was available. The link of DYNA with the new version of MADYMO should be completed. NHTSA could find this to be very useful for crash simulations including occupant interaction with the vehicle interior of the newly developed vehicle models.

LLNL provided FHWA with an estimate for accomplishing an RTH-DYNA link. FHWA needs to decide upon an RTH code before this capability is to be developed.

A more sophisticated tire model need not be developed until FHWA and NHTSA decide to simulate non-tracking vehicles over pavement or other terrain before vehicle impact with another vehicle or a roadside barrier.

An improved suspension model will be required for certain types of impacts between a vehicle and a barrier that has demonstrated a tendency for wheel snagging. Additional types of wheel/barrier interaction result in significant suspension damage that can influence the impact behavior between the vehicle and the barrier. For all of these situations, a more detailed model of common suspension types need to be developed that can then be inserted into the existing fleet of crash simulation vehicle models.

The material model survey combined with the experiences of simulation analysts during this project suggest that there are several models that should be developed. Improved material models for those materials used in vehicle interiors and in crash dummies need to be developed to enable better simulation of controlled crash tests. The soil into which all posts and u-channels are deployed may need improvement for barrier simulation calculations.

This project has identified a number of desired improvements for INGRID. LLNL provided an estimate for implementing these. A decision on how to best achieve the needed meshing capability needs to be discussed among FHWA, NHTSA, and the code development group at LLNL. Options may exist that will produce these additional features in a timely manner.

Table 19. Roadside hardware models being developed by universities.

Carnegie-Mellon University	-- IL 2399-1 bridge railing
Florida State University	-- G2 weak-post W-beam guardrail
Texas A&M University	-- Slip-base luminaire support
University of Colorado, Boulder	-- Transformer base luminaire support
University of Mississippi	-- Modified three beam guardrail
University of Nebraska	-- Dual-leg slip-base sign support
Vanderbilt University	-- NCIAS crash cushion

In 1994, FHWA initiated cooperative research programs with seven universities to develop roadside hardware models. The objective of this university program is to obtain the required FEA experience to perform good analyses and to build useful production models. The universities participating in the program, along with the hardware they are modeling, are shown in table 19. These small research programs are beginning to generate useful roadside hardware models. Much work remains before analytical methods achieve their full potential. The computer software tools are available and computing hardware continues to improve at a rapid rate making these analyses increasingly more feasible.

The training classes on DYNA theory and the use of the simulation tools have proved to be very valuable and should continue on a regular basis. The assistance given to analysts lacking the necessary several years of DYNA experience modeling vehicle crash simulation has proven to be of immense help to the many new DYNA analysts. This should be continued at whatever level that FHWA and NHTSA can afford. Few new analysts have the ability to debug these challenging crash simulations. LLNL certainly has the expertise to help with debugging these problems.

The most significant thing that FHWA and NHTSA have done and can continue to do is to build a community of nonlinear FE users in the roadside research arena. This community already includes FHWA, NHTSA, LLNL, commercial code developers, universities, and consultants. Perhaps the key lesson from FHWA's experience in trying to develop GUARD and NARD is that research performed in isolation from the end-users seldom succeeds. Building a network of collaborators is more difficult but more beneficial than harnessing competitors.

FHWA is promoting the NCAC at George Washington University as the repository and developer of vehicle models for roadside hardware simulation. Modeling roadside hardware will be distributed among a variety of universities and contributors. In principle, it is a natural mission for a center jointly funded by NHTSA and FHWA to be responsible for vehicle models since it is vehicles that link the two agencies. The success of this arrangement, however, depends on a close collaboration between vehicle model developers and hardware analysts that has, as yet, failed to develop.



LLNL, FHWA, and NHTSA have all experienced some difficulty in using the independently developed vehicle models for impact simulations. An improved method needs to be considered that eliminates the source of difficulty with the present approach. It is very important that some interaction takes place between the model developer and the analyst during the vehicle model development stage. Perhaps staged contract phases are one way to ensure that the analyst gain some experience using the model before it is totally completed. In this manner, the analyst can identify needed features in the model definition, explain their importance, and pass these on to the vehicle developer for the next stage of development. The modeling criteria identified in chapter 5 for the Honda model refinement should also be considered in the formulation of the contract specifications covering the model development. The Honda, Taurus, C-1500, and C-2500 trucks were developed with no useful interaction. All of these models have proven difficult to use by various analysts.

LLNL debugged the full-size Honda Civic model so that it is possible to simulate the frontal crash tests conducted at the FOIL. However, a more numerically efficient and stable model was developed to perform the parametric analyses required to fine-tune the model. These analyses were performed to debug, fine-tune, and capture the failure in the engine cradle which was observed in crash tests. Comparisons were made between the DYNA3D results from the modified Honda model and the FOIL test data. The comparison between the simulation and test data is quite good, but better correlation was obtained after additional model refinements. The correlation obtained is sufficient to qualify the modified Honda model as validated for the three pole tests and the u-channel described in chapter 5. A set of modeling criteria was developed for the Honda Civic FE model using the results from analyses and experience in modifying the vehicle model. These criteria should be used as guidelines in generating other impact vehicle models.

Even with simple vehicles and simple barrier models, this is a very challenging computation. At present, these simulations require the assistance of a highly experienced DYNA analyst. For FHWA to make substantial progress, it needs to collaborate more with experienced FE analysts during the vehicle/barrier model development.

The completed 2-year program has identified a critical need for vehicle models in addition to those shown currently available. These vehicle models must be available to all researchers (public domain). They must accurately replicate the kinematics of a vehicle before, during, and after impact. They must be capable of running to completion (200 to 400 ms for various impacts) on a workstation in fewer than 24 hours. They must represent the types of vehicles used in crash testing. There is an immediate need for vehicle models that correspond to the Report 350 test vehicles, most particularly for test level four and below.<sup>(88)</sup>

**820C.** A project was recently initiated to investigate emerging small-car vehicle platforms but this effort will only recommend what platform should be used in testing and analysis.<sup>(89)</sup> There appears to be no specific plan for replacing or upgrading the current 820C vehicle model.

**2000P.** The most troublesome operational issues in roadside safety hardware research today involve recent testing with pickup trucks. The large size of the current model will require 1,000 or more CPU hours for a single run. Obtaining a pickup truck model that can be used on a workstation should be FHWA's highest priority.

**8000S.** This is a key vehicle for bridge rail testing. Currently no models of trucks are available for roadside safety research and there are no plans for the development of such models.

There will be a need for other types of vehicles, such as minivans, sport utility vehicles, and cab-forward vehicles. The roadside hardware community must determine what types of models are required to evaluate roadside hardware performance. The development of vehicle models has been expensive and time consuming. It is the Government's responsibility to take the lead in developing a public domain vehicle fleet for use by roadside hardware researchers.

FHWA should concentrate its scarce resources on producing practical results that help address pressing operational questions. The performance of pickup trucks on common guardrails and terminals, the performance of minivans in hardware impacts, the effect of non-standard impact conditions on vehicle kinematics are just a few that need attention. If FEA is not part of the solution to these current problems, the simulation community will have missed a rare opportunity to prove the utility of analytical methods.

The use of FEA has great potential for improving roadside hardware designs. FHWA and NHTSA must find ways to continue to expand the FEA user base. Transforming this potential into action, however, requires leadership and a clear vision of how FEA fits into the overall roadside safety program.

## REFERENCES

1. Cornell Aeronautical Laboratory, *Development of an Analytical Approach to Highway Barrier Design and Evaluation*, Research Report 65-2, New York Department of Public Works, April 1963.
2. G. W. McAlpin, M. D. Graham, W. C. Burnett, and R. R. McHenry, "Development of an Analytical Procedure for Prediction of Highway Barrier Performance," In *Geometric Design and Barrier Rails*, Highway Research Record Number 83, Highway Research Board, Washington, DC, 1963.
3. M. D. Graham, W. C. Burnett, J. L. Gibson, and R. H. Freer, *New Highway Barriers: The Practical Application of Theoretical Design*, Highway Research Record 174, Highway Research Board, Washington, DC, 1967.
4. R. R. McHenry and N. J. DeLeys, *Development of Analytical Aids to Minimization of Single-Vehicle Accidents*, Cornell Aeronautical Laboratory, Report VJ-2251-V-10, 1971.
5. D. J. Segal, *Highway-Vehicle-Object Simulation Model-1976*, Report FHWA-RD-76-163, Federal Highway Administration, Washington, DC, 1976.
6. G. H. Powell, *BarrierVII: A Computer Program for Evaluation of Automobile Barrier Systems*, Report FHWA-RD-76-162, Federal Highway Administration, Washington, DC, 1973.
7. R. E. Welch and E. Pang, *Validation and Application of the Guard Computer Program*, Unpublished report for project DOT-FH-11-9460, Chiapetta, Welch, and Associates, Palos Hills, IL, 1984.
8. N. W. Iwankiw et al, *Modeling the Interaction of Heavy Vehicles with Protective Barriers*, IIT Research Institute, March 1980.
9. S. Basu and G. McHale, *Numerical Analysis of Roadside Design (NARD)*, Report FHWA-RD-88-212, Federal Highway Administration, Washington, DC, 1988.
10. H. Kamil, D. S. Logie and M. H. Ray, *Development of a Plan for Upgrading Vehicle-Barrier Response Simulation Capabilities*, Unpublished report for FHWA (SAT 280.03), Structural Analysis Technologies, Inc. 4677 Old Ironsides Drive, Santa Clara, CA 95054, April 1992.
11. R. L. Chiapetta, *Development of an Upgrading Plan for Highway Safety Simulation Models*, Report FHWA-RD-92-078, Federal Highway Administration, Washington, DC, September 1992.

12. M. McCulough, *An Upgrade Plan for FHWA Roadway Safety Simulation Models*, Report FHWA-RD-93-189, Federal Highway Administration, Washington, DC, 1994.
13. R. G. Whirley, B. E. Englemann, *DYNA3D: A Nonlinear Explicit Three-dimensional Finite Element Code for Solid and Structural Mechanics (User's Manual)*, Report UCRL-MA-107254 Revision 1, Lawrence Livermore National Laboratory, Livermore, CA, November 1993.
14. *MADYMO User's Manual 3D*, TNO Road-Safety Research Institute, The Netherlands, 1992.
15. L. A. Obergefell, T. R. Gardner, I. Kaleps, and J. T. Fleck, *Articulated Total Body Model Enhancement, Volume 2: User's Guide*, Harry G. Armstrong Aerospace Medical Research Laboratory, Wright-Patterson Air Force Base, AAMRL-TR-88-043, 1988.
16. S. W. Kirkpatrick, B. S. Holmes, W. T. Hollowell, H. C. Gablar, and T. J. Trella "Finite Element Modeling of the Side Impact Dummy (SID)," SAE International Congress and Exposition, Paper 930104, Detroit, Michigan, 1993.
17. J. W. Wekezer, M. S. Oskard, R. W. Logan, and E. Zywicz, "Vehicle Impact Simulation," *Transp. Engr.*, Vol. 119, J. No. 4, pp 598-617, 1993.
18. NHTSA Test 1566 performed by TRC of Ohio on March 5, 1991.
19. U. Hoffmann, and W. Protard, J. Scharnhorst, "Finite Element Analysis of Occupant Restrain System Interaction with PAM-CRASH," 4<sup>th</sup> Stapp Car Crash Conference, paper 902325, Orlando, Florida, 1990.
20. A. L. Beguelin, J. J. Dongarra, G. A. Geist, W. C. Jiang, B. J. Manchek, B. K. Moore, and V. S. Sunderam, *PVM 3.2 : Parallel Virtual Machine System 3.2*, University of Tennessee, Oak Ridge National Laboratory, Emory University, 1992.
21. B.N. Maker, R.M. Ferencz, and J.O. Hallquist, *NIKE3D: A Nonlinear, Implicit, Three-Dimensional Finite Element Code for Solid and Structural Mechanics, User Manual*, Lawrence Livermore National Laboratory, Livermore, California, UCRL-MA105268, 1991.
22. R.W. Logan, *Tire, Accident, Handling, and Roadway Safety*, Engineering Research, Development, and Technology, Lawrence Livermore National Laboratory, Livermore, California, UCRL-53868-92, 4-1, 1992.
23. E. Zywicz and G.J. Kay, *DYNA3D Airbag Development*, Lawrence Livermore National Laboratory, Livermore, California, UCRL-53868-94, 2-1, 1994.

24. J. T. Wang and D.J. Nefske, *A New CAL3D Airbag Inflation Model*, SAE Technical Paper Series, #880654, presented at the Int. Congress and Exposition Detroit, Michigan, March 4, 1988.
25. G. J. Van Wylén, *Fundamentals of Classical Thermodynamics 51 Version, 2e*, John Wiley & Sons, New York, p. 120, 1978.
26. M. C. Potter and F.F. Foss, *Fluid Mechanics* (Great Lakes Press, Inc.), East Lansing, Michigan, p. 356, 1982.
27. G. J. Kay and E. Zywicz, *Development and Validation of a DYNA3D Air Bag Model*, (in preparation) 1994.
28. *PATRAN3*, The MacNeal-Schwendler Corporation, Los Angeles, May 1995.
29. NHTSA Test 1600 performed by Calspan on April 25, 1991.
30. A. L. Beguelin, J. J. Dongarra, G. A. Geist, W. C. Jiang, B. J. Manchek, B. K. Moore, and V. S. Sunderam, *PVM 3.2: Parallel Virtual Machine System 3.2*, University of Tennessee, Oak Ridge National Laboratory, Emory University, 1992.
31. M. A. Christon and D. Dovey, *INGRID - A 3-D Mesh Generator for Modeling Nonlinear Systems*, Lawrence Livermore National Laboratory, UCRL-MA-109790, 1992.
32. M. A. Puso, "Foam Material Modeling," Lawrence Livermore National Laboratory, Livermore, California UCRL-53868-94, p. 2-37, 1994.
33. L. J. Gibson, M.F. Ashby, J. Zhang, and T.C. Triantfillou, *Failure Surfaces for Cellular Materials under Multiaxial Loads - II. Comparison of Models with Experiment*, International Journal of Mechanical Science, Vol. 31, p. 635, 1989.
34. M. R. Patel and I. Finnie, *The Deformation and Fracture of Rigid Cellular Plastics under Multiaxial Stress*, Lawrence Livermore National Laboratory, Livermore, California, UCRL-13420, 1970.
35. L. J. Gibson and M.F. Ashby, "Cellular Solids: Structure and Properties Pergamon Press," Oxford, p. 147, 1988.
36. Shaw, M.C. and T. Sata, International Journal of Mechanical Science, Vol. 8, 469, 1966.
37. Duvaut, G. and J.L. Lions, *Les Inequations en Mechanique et en Physique* Dunod, Paris, 1972.
38. A.K. Maji, S. Donald, and K. Cone, Testing of impact Limiters for Transportation Cask Design, Proc. Materials Research Society Symposium, 1991.
39. Energy Absorbing Foams for Automotive Applications," Proc. 34th Annual Polyurethane Technical/Marketing Conf., 438.

40. Logan, R. W., Applications of Advanced Material Models, Lawrence Livermore National Laboratory, Livermore, California UCRL-53868-94, 2-27, 1994.
41. Logan, R. W., Tire, Accident, Handling, and Roadway Safety, Lawrence Livermore National Laboratory, Livermore, California UCRL-53868-92, 4-1, 1993.
42. Krieg, R.D., A Simple Constitutive Description for Soils and Crushable Foams, Sandia National Laboratories, SC-DR-72 0883, 1972.
43. A.L. Browne and T.B. Khalil, *Windshield Impact Response: A Finite Element Model, Crashworthiness and Occupant Protection in Transportation Systems*, ASME AMD Vol. 106, T.B. Khalil and A.I. King, Eds, 1989.
44. EASi Engineering, *Finite Element Model of 1982 Honda Civic, A Users Manual*, August 1993.
45. C.M. Brown, *Crush Characteristics for 1981-1983 Honda Civics*, Department of Transportation, Federal Highway Administration, June 1994.
46. R.W. Logan, J.M. Burger, L.D. McMichael, and R.D. Parkinson, Crashworthiness Analysis using Advanced Material Models in DYNA3D, AMD-Vol. 169, ASME, 1993.
47. J. C. Chen and M.C. Witte, Development of Soil/Rock Constitutive Models and Benchmark Analysis for Gas-Gun Penetration Tests at the PSA Flight 1771 Crash Site, Lawrence Livermore National Laboratory, PATC-IR 89-12, March, 1990.
48. A. Gonzales, Target Effects on Package Response: An Experimental and Analytical Evaluation, Sandia National Laboratory, SAND86-2275, TTC-0696, May 1987.
49. A. S. Lee, *Pre-VISTA Report on Task D.1 and Task D.2*, Lawrence Livermore National Laboratory, June, 1994.
50. A. S. Lee, S. A. Perfect, and R. W. Logan, *Refinement and Application of a Frontal Impact Vehicle/Barrier Model*, paper presented in the Transportation Research Board, January 1993.
51. H. E. Ross, Jr., D. L. Sicking, and J. D. Michie, *Recommended Procedures for the Safety Performance Evaluation of Highway Features*, NCHRP Report 350, Transportation Research Board, 1993.
52. E. Cofie and M. H. Ray, *Finite Element Model of a Small Automobile Impacting a Rigid Pole*, Report FHWA-RD-94-151, Federal Highway Administration, Washington, DC, 1995.
53. R. Rainesburger. *TRUEGRID MANUAL*, Version 0.99, XYZ Scientific Applications, September 1993.

54. B. E. Brown and J. O. Hallquist. *TAURUS: An Interactive Post-Processor for the Analysis Codes NIKE3D, DYNA3D & TOPAZ3D*, University of California, Lawrence Livermore National Laboratory, Report UCID-19392, May 1991.
55. C. Brown, *Crush Characteristic of Four Mini-Sized Vehicles, Test Numbers 91F049 92F032, and 92F033*, Report No. FHWA-RD-93-075, Federal Highway Administration, McLean, May 1993.
56. J. D. Michie and M.E. Bronstad, *Guardrail Crash Test Evaluation: New Concepts and End Designs*, National Cooperative Highway Research Program Report No. 129, Highway Research Board, Washington, DC, 1972.
57. M. E. Bronstad and J. D. Michie, *Evaluation of Breakaway Cable Terminals for Guardrails*, Research Results Digest No. 43, National Cooperative Highway Research Program, Transportation Research Board, Washington, DC, October 1972.
58. M.E. Bronstad and J. D. Michie, *Development of Breakaway Cable Terminal for Median Barriers*, National Cooperative Highway Research Program, Research Results Digest 53, Washington, DC, 1973.
59. M.E. Bronstad and J. D. Michie, *Breakaway Cable Terminals for Guardrails and Median Barriers*, National Cooperative Highway Research Program, Research Results Digest 84, Washington, DC, March 1976.
60. M. E. Bronstad and J. D. Michie, *Modified Breakaway Cable Terminals for Guardrails and Median Barriers*, Research Results Digest No. 102, National Cooperative Highway Research Program, Transportation Research Board, Washington, DC, May 1978.
61. M. E. Bronstad, *A Modified Foundation for Breakaway Cable Terminals*, Research Results Digest No. 124, National Cooperative Highway Research Program, Transportation Research Board, Washington, DC, November 1980.
62. *W-Beam Guardrail End Treatments*, Federal Highway Administration, FHWA Technical Advisory T 5040.25, Change 1, Washington, DC, December 15, 1987.
63. M. E. Bronstad and J. D. Michie, *Recommended Procedures for Vehicles Crash Testing of Highway Appurtenances*, National Cooperative Highway Research Program, Report 153, Washington, DC, 1974.
64. HRB Committee on Guardrails and Guide Posts, *Full-Scale Crash Testing Procedures for Guardrails and Guide Posts*, Highway Research Board, Circular No. 482, September 1962.

65. C. E. Kimball, M. E. Bronstad, and L. C. Meczkowski, *Evaluation of Guardrail Breakaway Cable Terminals*, Federal Highway Administration, Report No. FHWA-RD-82-057, Washington, DC, May 1982.
66. J. G. Pigman and K. R. Agent, *Survey of Guardrail End Treatment Usage*, University of Kentucky, Research Report UKTRP-83-23, October 1983.
67. R. F. Baker, *Breakaway Cable Terminal Evaluation*, New Jersey Department of Transportation with the Federal Highway Administration, FHWA-NJ-81-001, Washington, DC, May 1980.
68. M. E. Bronstad, J. B. Mayer, J. H. Hatton, and L. C. Meczkowski, *Test and Evaluation of Eccentric Loader BCT Guardrail Terminals*, Federal Highway Administration, Report No. FHWA-RD-86-009, Washington, DC, September 1985.
69. L. C. Meczkowski, *Evaluation of Improvements to Breakaway Cable Terminals*, Federal Highway Administration, Report No. FHWA-RD-91-065, Washington, DC, June 1991.
70. L. A. Staron, *Guardrail Terminals: Breakaway Cable Terminal, Eccentric Loader Terminal and Modified Eccentric Loader Terminal*, Federal Highway Administration, Memorandum, Washington, DC, March 27, 1991.
71. G. H. Powell, *Barrier VII: A Computer Program for Evaluation of Automobile Barrier Systems*, Federal Highway Administration, Report No. DOT-RD-73-51, Washington, DC, 1973.
72. AASHTO-ATRBA-AGC, *Guide to Standardized Barrier Hardware*, AASHTO-ARTBA-AGC Joint Committee, Task Force No. 13, American Association of State Highway and Transportation Officials, Washington, DC, 1994.
73. FHWA, *Corrugated Sheet Steel (W-Beam) Guardrail*, Federal Highway Administration, FHWA Technical Advisory T 5040.23, Washington, DC, March 13, 1984.
74. AASHTO, *Standard Specifications for Transportation Materials and Methods Sampling and Testing: Part I - Specifications*, Fifteenth Edition, American Association of State Highway and Transportation Officials, Washington, DC, 1990.
75. L. R. Calcote, *Development of a Cost-Effectiveness Model for Guardrail Selection*, Federal Highway Administration, Report No. FHWA-RD-78-74, Washington, DC, January 1980.
76. M. H. Ray and J. F. Carney III, *Side Impact Crash Testing of Roadside Structures*, Federal Highway Administration, Report No. FHWA-RD-92-079, Washington, DC, May 1993.



77. *Wood Handbook: Wood as an Engineering Material*, United States Department of Agriculture, Forest Service, Agricultural Handbook 72, Washington, DC, 1987.
78. D. Dovey, *GRIZ: Finite Element Analysis Results Visualization for Unstructured Grids, Users Manual*, Lawrence Livermore National Laboratory, Report UCRL-MA-115696 (Draft), Livermore, CA, October 1993.
79. *AISI, Wire Rope Users Manual*, Committee of Wire Rope Producers, American Iron and Steel Institute, Washington, DC, 1979.
80. NHTSA, *Traffic Safety Facts 1992*, Report Number DOT-HS-808-022, National Highway Traffic Safety Administration, Washington, DC, March 1994.
81. H. E. Ross, Jr., White paper on ISTEVA vehicles, Texas Transportation Institute, College Station, TX, 1995 .
82. M. H. Ray and J.F. Carney, *Side Impact Crash Testing of Roadside Structures*, Report Number FHWA-RD-92-079, Federal Highway Administration, Washington, DC, 1993.
83. L. A. Troxel, M. H. Ray, and J. F. Carney III, *Accident Data Analysis of Side-impact Fixed-Object Collisions*, Report No. FHWA-RD-91-122, Federal Highway Administration, Washington, DC, 1994.
84. K. K. Mak and W. C. Menges, Testing of State Roadside Safety Systems, Texas Transportation Institute, Federal Highway Administration Project DTFH61-89-C-00089, in progress.
85. C. F. Brown, *FOIL Test 94F032*, Draft of unpublished test report, Federal Outdoor Impact Laboratory, Federal Highway Administration, Washington, DC, 1994.
86. M. H. Ray and J. R. Viner, *Importance of Vehicle Structure and Geometry on the Performance of Roadside Hardware Safety Features, In Vehicle Highway Infrastructure: Safety Compatibility*, Report P-194, Society of Automotive Engineers, Warrendale, PA, 1987.
87. S. Varadappa, S. C. Shyo, and A. Mani, *Development of a Passenger Vehicle Finite Element Model*, Report DOT-HS-808-;45, National Highway Traffic Safety Administration, Washington, DC, November 1993.
88. M. H. Ray, The Use of Finite Element Analysis in Roadside Hardware Design, TRB Committee A2A04, Roadside Safety Features 1995 Summer Meeting at Irvine, CA, July 31, 1995.
89. J. Reid and D. L. Sicking, Reevaluation of Turned Down Guardrail Terminals, Transportation Research Record (in progress), Transportation Research Board, 1995.

